Electronic Transport in Hybrid Heterostructures

and

Universal Control of Spin-Orbit Interaction in Quantum Wells

Inauguraldissertation

zur

Erlangung der Würde eines Doktors der Philosophie

vorgelegt der

Philosophisch-Naturwissenschaftlichen Fakultät

der Universität Basel

von

Florian Dettwiler

aus Reigoldswil, BL

Basel, 2015

Genehmigt von der Philosophisch-Naturwissenschaftlichen Fakultät auf Antrag von

Prof. Dr. D. M. Zumbühl

Prof. Dr. W. Wegscheider

Basel, 25. März 2014

Prof. Dr. Jörg Schibler

Dekan

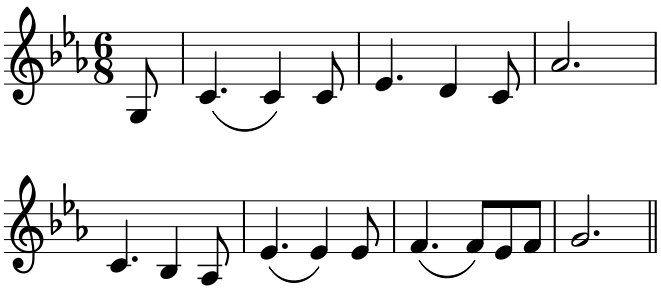

Richard Wagner

Abstract

In recent years, the control of charge and spin in semiconductors has experienced outstanding progress. The extended spin coherence times established in high quality materials together with the advance in elaborate fabrication methods enable coherent spin control, ultimately leading to new spintronic devices. In this thesis, we investigate various aspects of quantum transport with respect to potential spintronic applications in two different kind of 2-dimensional electron gases (2DEGs) in GaAs/AlGaAs crystals.

First, we try to combine the advantages of optically active InAs quantum dots (QDs) and the versatile possibilities of gate tunable 2DEGs in a novel hybrid heterostructure. We have characterized a series of hybrid wafers with different spacings between the inverted 2DEG and Stranski-Krastanov grown self-assembled InAs QDs. Depending on this distance and actual QD nucleation – verified with atomic force microscopy on the wafer surface – the 2DEG mobility is reduced due to scattering induced by the QDs and the InAs wetting layer. For a tunnel barrier of 45 nm, the 2DEG exhibits mobilities exceeding $500'000\,\mathrm{cm}^2/(\mathrm{Vs})$ despite the presence of InAs QDs, while coherent tunneling between 2DEG and QDs is still permitted. Using a top down approach, lateral quantum point contact gates are aligned precisely to a single, specifically chosen InAs QD. The 1D conductance is not sensitive to QD charging events, but is dominated by a disorder potential, even suppressing quantization.

In the second part of the thesis, we study the control of spin-orbit (SO) interaction. This relativistic coupling of the electron spin to its momentum can be used for coherent spin manipulation, but at the same time also causes spin relaxation. Theory predicts a special symmetry, protecting spin from relaxation in diffusive transport, when the two main contributions of SO interaction in GaAs quantum wells (QW) – the Rashba and the Dresselhaus effect – are of equal strength. We demonstrate broad, independent control of all relevant SO fields, allowing us to tune into this regime. By electrically

locking the Rashba and Dresselhaus SO fields via top and back gate, we achieve spin protection for a wide range of voltages on a single QW. We use quantum corrections to 2D conductivity as a sensitive probe of SO coupling. The combination of transport data and numerical calculations allows us to quantify the relevant SO coefficients.

Acknowledgments

This work would not have been possible without the help and effort of many people. Most of all, I would like to thank my supervisor Prof. Dominik Zumbühl. Working in the group of an enthusiastic experimentalist with excellent contacts to scientists around the world comes with many amenities I could profit from a lot during my PhD time. I really learned how to *ctrl + mouse-wheel-scroll* to the smallest detail without losing the bigger picture at the same time. I'm grateful for his guidance comprising of numerous lessons and discussions - from measurement and fabrication details up to challenging new physics out of the experiments - always equipped with reasonable degrees of freedom.

I'd like to take the opportunity to express my gratitude to Prof. Werner Wegscheider, first for being in my committee and reading through my thesis but of course also for the exciting and interesting meetings we had when we discussed material issues of the hybrid project. Having the right material is one of the most important prerequisites of every solid state experiment and therefore it was a great privilege to collaborate with outstanding experts of the field. I use here the plural to also include Prof. Antonio Badolato - at that time a senior scientist at ETH - and his expertise in self-assembled quantum dot growth.

A special thanks goes to the second examiner Prof. J. Carlos Egues. The deep interaction between our spin-orbit data and the theoretical aspects introduced by the numerical simulations was only possible thanks to his support and efforts, also by bridging the distance between São Paulo and Basel by plane. The extended meetings and numerous e-mail discussions were not only enlightening but also very enjoyable. Also, I'd like to thank Jiyong Fu, who run simulations day and night during his visits in Basel. Whenever I needed additional data, he prepared it within the Brazilian-Swiss time shift and it was always a great pleasure to work with him.

All the extensive experiments on $\alpha = \beta$ would not have been possible without the right

wafers. I would like to express my gratitude to Prof. David Awschalom and Shawn Mack for providing us with the quantum well material. It was quite a journey from the first multi quantum well samples to the final structures, with empty MBE sources, a broken substrate controller and other obstacles on the way. But thanks to the effort of Shawn and the support from David we ended up with just the right structures!

Also, I thank Pirmin Weigele for all the valuable input and discussions and I'm looking forward to the new physics he's going to squeezes out of the project. Further, I'd like to thank Parisa Fallahi and Florian Haupt for supporting us with optical measurements on the hybrid material and "my" former master and semester project students Leon Camenzind, Lukas Greuter and Serge Waechter for their contribution and the many challenging questions they asked.

During the last years, I could always count on a good spirit in our group. I (hopefully) will always remember office 1.12 as a great place to work. I'd like to especially thank Lucas Casparis, Dorothee Hug and Dario Maradan for standing, partially adapting and developing the spirit of *Kynismus* and for interesting, more physics-related discussions. Of course I would like to extend my thanks to the office next door, where I could find support from Daniel Biesinger, Myrsini Lafkioti, Mario Palma and Christian Scheller or a cold beer to enjoy together. When I started, Charulata Barge introduced me into the magic of cleanroom fabrication and I always found help to any kind of problem from the more experienced former group members: Kristine Bedner, Tony Clark, Sarah Heizmann, Dominikus Kölbl, Tai-Min Liu and Kai Schwarzwälder.

A big thank goes also to the other groups in the house – especially the Schönenberger group – for sharing, lab space, lab equipment and meetings and also for keeping all the machines running. The reliable and flexible handling of the liquid helium supply was only possible thanks to Dominik Sifrig. I would also like to mention the very helpful and friendly assistance of the whole workshop team of Sascha Martin, including the electronics workshop team around Michael Steinacher, as well as the administrative support from Barbara Kammermann and Astrid Kalt.

Also, I would like to thank some of my former fellow students who proved to be good company even after the undergraduate time. I especially enjoyed coffee breaks and non-physics discussions with Meret Hornstein and Kasper Renggli.

Almost last but not least, I also would like to acknowledge the office coffee machines (I-III) for the daily caffeine kick and of course MCK-50, the working horse of most of my measurements (and of course the construction team from Leiden behind it). Apart from one severe blockage, the fridge has proven to be a tight-ripped, yet highly reliable partner in the lab.

I entered the University of Basel as a young nanoscience student somewhat more than ten years ago and this chapter is now closing. I would like to thank everyone who made this decade an interesting, challenging and enjoyable experience both on the educational and personal basis. A special thanks goes to my parents - especially my dad - for having enabled all this and to my friends, fellow students and coworkers for having endured my personality during the last years. Finally, I hope that I did not forget anyone. In any case: thank you!

Contents

1 Introduction and Motivation

One of the foundations of the fast technological progress in electronic devices and their rapid distribution towards the end of the 20^{th} century was laid by Shockley, Bardeen and Brittain with the first demonstration of a working transistor in the late 1940s, awarded with the Nobel Prize in 1956 [1]. Following their idea of using semiconductors for the implementation of the bipolar transistor (they used germanium), soon unipolar field effect transistors (FETs) became available and today silicon metal-oxide-semiconductor FETs (MOSFETs) are the most popular transistors, found in almost every integrated circuit. Despite or even because of the tremendous progress during the last decades, the classical silicon based technology reaches more and more limitations and physical boundaries.

Today's solid state research is not only focused on pushing these borders, but also on finding new ways to solve existing and even future problems. In the center of these efforts, the concepts of *quantum mechanics* are of crucial importance. The quantum theory started to develop in the early 20^{th} century and succeeded in describing many physical phenomena in a fundamentally new way, beyond the well established disciplines of classical physics. Starting from nuclear, particle and atomic physics, quantum mechanics has led to a different way of describing matter and also of understanding solid state material on a microscopic level. Together with general relativity it even reaches into cosmology and today is also widely used in other science disciplines like chemistry and biology. In the framework of physics, the theory opens the way to new schemes of information processing and transmission and these fields are called *quantum computation* [2–5] and *quantum cryptography* [6, 7].

The basis of quantum computation is the quantum bit or *qubit* [8], the quantum mechanical analog to the two level system 0 and 1 of a classical bit. Technically speaking, a qubit is also a two level system, but the waveform description of a single or a many body state allows also for superposition and entanglement and thus, more information

is stored in a single qubit. Known benefits are the speed gains in solving complex mathematical problems like e.g. prime factorization [9] using quantum algorithms. Although first commercial quantum computers became available recently, their functionality is under debate and the fundamental requirements defined by DiVincenzo [10] are still the guidelines for the quest to a successful and fast quantum computer.

One possible and prospective candidate for a quantum mechanical two-level system itself is a purely quantum mechanical concept: the spin [11, 12]. The two eigenstates of parallel or antiparallel alignment in a magnetic field ($|\uparrow\rangle$ or $|\downarrow\rangle$) are separated by the Zeeman energy and thus provide a natural two level basis. Additionally, superpositions of the form $|\Psi\rangle = \cos(\theta/2)\,|\uparrow\rangle + e^{i\phi}\sin(\theta/2)\,|\downarrow\rangle$ are allowed, where angle θ determines the amplitude and ϕ the phase of the state on the Bloch sphere [11].

A scalable system for encoding and universally controlling quantum information is the spin state of single electrons confined in gate defined quantum dots (QDs) on a 2-dimensional electron gas (2DEG). It was proposed in 1998 [13] and has the potential to fulfill the DiVincenzo requirements. The 2DEG material of choice for a large number of quantum dot and quantum transport experiments in general is GaAs/AlGaAs. Due to the high quality of the epitaxially grown systems reached today and the possibility of tailoring it into almost any desired shape using nanofabrication methods, GaAs/AlGaAs 2DEGs are used in a very broad variety of experiments. Indeed, the progress in engineering on a nanoscale level, experimental methods and the understanding of quantum physics have led to substantial progress in coherent control on the spin on single and double QD systems [14–16].

A similar but less tunable confinement is found in small islands of InAs or other small band gap material embedded in a semiconductor environment (e.g. GaAs) with larger band gap. These self-assembled quantum dots (SAQDs) at the same time can confine electrons and holes and couple to radiation fields [17–19]. Moreover, they have been shown to act as perfect single-photon sources [20, 21] and the quantum information of a spin can be converted to photon polarization [22] or even be entangled with a photon

[23] using InAs QDs. Although double dot systems with vertically stacked InAs islands are also possible [24], the scalability to larger arrays of qubits has proven to be of a major challenge. On the other hand, the optical accessibility opens a very broad field of applications.

1.1 Thesis Outline

One main part of the thesis explores, how these InAs quantum dots influence 2DEG transport properties. For that purpose, we study *hybrid* GaAs/AlGaAs heterostructures with InAs QDs in close vicinity. The hybrid structure follows the proposal for a *quantum optical interface* by Engel *et al.* [25], which is shown in Figure 1.1: InAs self-assembled QDs are grown on top of the interface in such a way as to enable electrons inside the QD to couple coherently to the 2DEG by tunneling. Adding lateral top gates, an additional gate-defined QD can be formed in the 2DEG, below the InAs QD.

Conceptually, the InAs QD acts as an optical interface for fast initialization and readout and spin-photon entanglement, while the advanced electronic control of the QD in the 2DEG allows for fast qubit operations. The conversion from spin to charge provides a way to send and receive quantum information over long distances, which together with the the concept of *flying qubits* by entanglement could be used to optically connect several gate defined qubits.

A general introduction to GaAs/AlGaAs 2DEGs, InAs QDs and electron transport is given in the beginning of Chapter 2. In the subsequent Chapter 3, the effect of the InAs QDs on the nearby hybrid 2DEG is studied and then we take a look at 1D transport and single QD devices in Chapter 4.

The basis of solid state spin qubits in a broader sense is the (coherent) control of spins in electronic devices in general via magnetic or electric fields. Novel *spintronic* devices that make use not (solely) of the charge, but also of the magnetic moment of

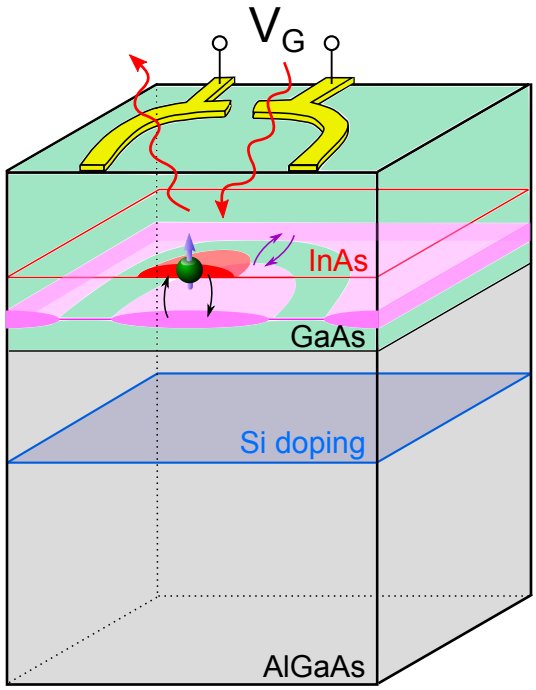

Figure 1.1: Quantum optical interface. Schematic of a hybrid heterostructure, consisting of a 2DEG (purple) and an optically active InAs self-assembled QD (red), as proposed in Ref. [25]. By applying a voltage V_G on the top gate nanostructure (yellow), a gate-defined QD is formed in the 2DEG, in close proximity to the SAQD. The two QDs are coupled via electron tunneling, as indicated by black arrows. The SAQDs are optically addressable (red arrows), while gate defined QDs allow for fast electrical spin manipulation and are coupled to the surrounding 2DEG (purple arrows).

the electron have potential advantages over conventional electronic devices like lower power consumption or increased processing speed. In particular the *spin-orbit interaction*, the coupling of the electron spin to its momentum, allows for fast *all electrical* spin manipulation, as an alternative to large magnetic fields and radio-frequency field pulses. To implement spintronic devices, the focus of research is on the initialization or polarization, the relaxation mechanisms and the read-out of single spins or spin ensembles [26, 27].

In almost any of the above mentioned aspects, the spin transistor conceptually introduced by Datta and Das in 1990 [28], is a very paradigmatic spintronic device. The working principle is sketched in Figure 1.2. Instead of regulating (or rather switching) a charge current by applying an electric field on the conduction channel as in a classical FET, the electric field of the gate induces spin precession via spin-orbit (SO)

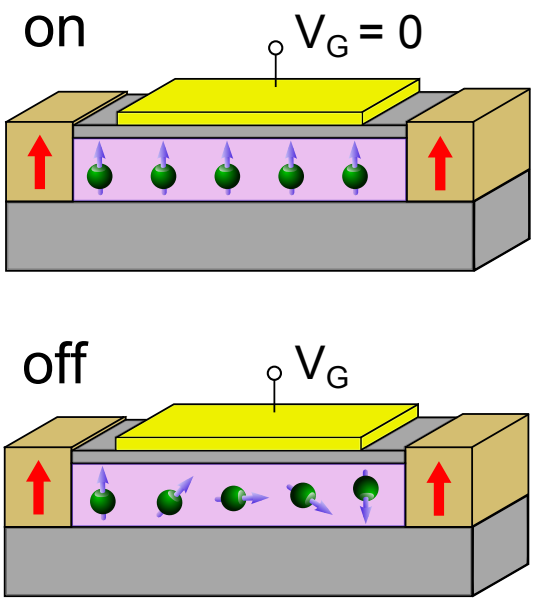

Figure 1.2: The Datta-Das spin transistor [28]. By applying a gate voltage V_G on the top gate (yellow) the precession of the spins in the 2DEG (purple) can be controlled by an electric field via spin-orbit coupling. Polarized spins are injected at a ferromagnetic source (left brown) contact. The red arrow indicates the ferromagnetic polarization. Depending on their relative orientation, spins are detected at the drain contact (right brown) and the transistor is in an *on*-state (parallel, upper) or *off*-state (antiparallel, lower).

coupling. The relative rotation of the polarized spins injected at the source (e.g. ferromagnetic contact) is detected at the drain contact. This *all-electrical* control of the spin has drawn a lot of attention and a first working ballistic device was demonstrated on an InAs heterostructure in 2009 [29]. Problems however arise from unwanted spin relaxation in the diffusive transport due to the resulting fluctuations in the SO-field.

The strict requirement of ballistic transport can be overcome, if the spin is robust against scattering, as in the non-ballistic spin FET proposed by Schliemann *et al.* [30]. Long spin relaxation times despite scattering can be achieved in a GaAs/AlGaAs 2DEG, when spin rotations around a uniaxial effective magnetic field – arising from SO coupling – result in a well defined helical motion. In this case, optically induced spin polarization patterns were shown to have an enhanced lifetime [31] and a stable (persistent) spin helix pattern forms [31, 32]. We explore the origin and requirements for this effect in the second part of Chapter 2, beginning from 2.4. With the focus on transport experiments, the effect on quantum corrections to magnetoconductance

are discussed. Experimental results are presented in Chapter 5, where we demonstrate *universal* control of all the relevant SO contributions, which allows us to have in-situ control on the spin relaxation time and the SO-length. This control allows us to protect the spin from relaxation by locking the two relevant SO-fields – the Rashba and the Dresselhaus effect – at equal strength over a wide range of gate voltages.

Finally, a summary of the most intriguing results and an outlook on possible future experiments are given in Chapter 6.

2 Background

2.1 The 2-dimensional Electron Gas in GaAs/AlGaAs Heterostructures

The 2-dimensional electron gas (2DEG) created in semiconductor heterostructures is an ideal system for quantum transport and quantum optics experiments. Superior properties like the high charge carrier mobility offer attractive possibilities for high frequency electronic devices, if compared to other semiconductors (e.g. Si). The discovery of new quantum Hall 2D-physics in the 1980s [33] was soon followed by a vast variety of mesoscopic experiments, exploring the even lower dimensional physics, by confining the 2DEG into nanometer sized structures via electrostatic gating or etching into quantum point contacts (1D, see Chapter 2.3) or quantum dots (0D). Here, just a brief and focused introduction to the broad topic is given, which should help the reader to understand the subsequent chapters.

The dimensionality reduction of a bulk (3D) solid state crystal to a 2D plane is achieved by a spatial confinement of conduction band electrons, which is smaller than their wavelength λ_F at the Fermi surface. In GaAs/AlGaAs heterostructures discussed here, this is done by creating a potential well with the width of some nanometers along the growth direction $\hat{z}$, perpendicular to the 2DEG in the $\hat{x}$-$\hat{y}$-plane.

GaAs is a III-V semiconductor forming a zinc blende crystal structure, with a direct band gap $E_g = 1.44\,\text{eV}$ ($1.519\,\text{eV}$ at $0\,\text{K}$). By adding a well defined amount of Al, the band gap can be engineered to values up to $\approx 2\,\text{eV}$. Typical Al-fractions are $\approx 30\%$, while above 45% the band gap of AlGaAs becomes indirect. To form a 2DEG, a sequence of GaAs and AlGaAs layers - each with its specific band gap - is grown, using the molecular beam epitaxy (MBE) technique. Alignment of the Fermi levels and distribution of charge carriers, coming from Si donor atoms (e.g. modulation doping using a Si δ-doping layer some nanometers away from the interface), lead to a bending of the

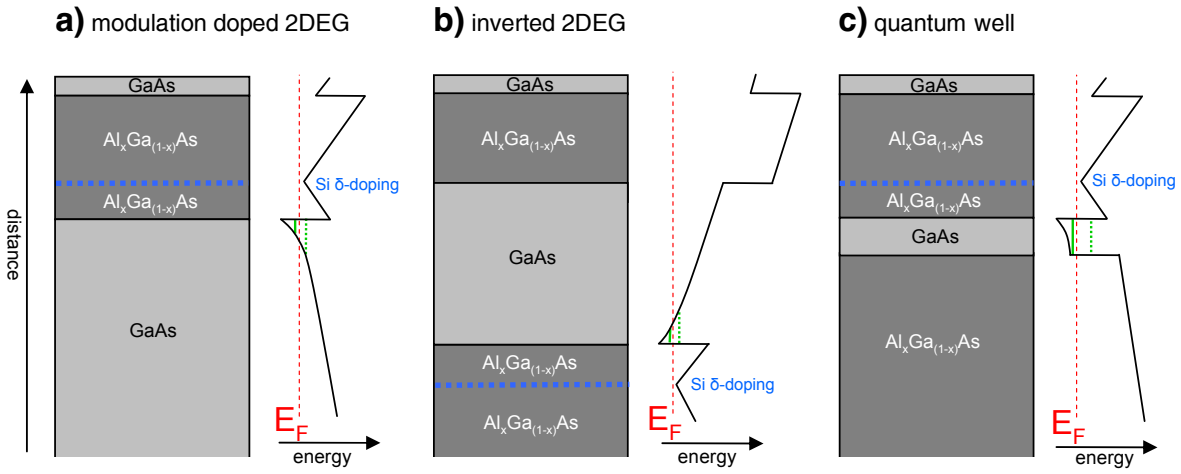

Figure 2.1: Different types of GaAs/AlGaAs 2DEGs. (a) Typical 2DEG structure with (from top) GaAs capping layer, AlGaAs blocking barrier, Si δ-doping (dashed blue line), tunneling barrier and GaAs substrate. The 2DEG forms in the triangular well at the GaAs/AlGaAs interface due to conduction band bending (diagram on the right), with subbands (green) filled up to Fermi energy E_F (red dashed line). **(b)** For inverted 2DEGs, donors are placed below the 2DEG. **(c)** The square potential of a QW has two (finite) band offset walls as boundaries.

bands and – locally at the band offset of the GaAs/AlGaAs interface – to quantum mechanical states in the potential well of the conduction band. These states are filled up to the Fermi energy E_F, with usually just the quantum mechanical ground state being occupied. In Figure 2.1a a typical growth structure and the corresponding band diagram are shown. In this work we mainly discuss two slightly modified cases: (i) the inverted 2DEG, a triangular potential well with doping below the heterointerface (Figure 2.1b) and (ii) quantum wells (QW), which can be described as a square potential well with two band offset walls, as shown in Figure 2.1c.

2.1.1 Basic Transport Properties

In a degenerate GaAs 2DEG, the electrons contributing to charge transport are described semi-classically as quasi free particles with Fermi energy $E_F = \frac{\hbar^2 k_F^2}{2m^*}$, where $k_F = \frac{2\pi}{\lambda_F}$ is the Fermi wave vector and $\hbar$ Planck's constant divided by 2π. The individual electron moves in the 2D plane at Fermi velocity $v_F = \hbar k_F / m^*$. The effective

mass $m^* = 0.067 \cdot m_e$, deviating from the free electron mass m_e by a factor of ~ 15, accounts for the crystal potential. In absence of an external magnetic field, the density of states (DOS) within one subband $\mathcal{D}_{2D} = \frac{m^*}{2\pi\hbar^2}$ is constant and hence independent of k and electron density $n = k_F^2/(2\pi)$. The charge carriers have fermionic character and follow the Fermi-Dirac distribution

$$f(E,T) = \frac{1}{e^{(E-\mu_c)/k_BT} + 1}, \tag{1}$$

with μ_c being the electrochemical potential and k_B Boltzmann's constant. For temperature $T = 0$, the chemical potential is equal to the Fermi energy $\mu_c = E_F$ and $f(E, 0)$ is a step function.

To first order, diffusive 2D transport can be described by the Drude-Sommerfeld model of transport in metals, defining the steady state conductivity as $\sigma = ne\mu$, where $e > 0$ is the elemental charge. The mobility $\mu = e\tau_p/m^*$ connects the drift velocity v_D to the electric field E applied to the 2DEG via $v_D = \mu E$. The time between two scattering events is the transport scattering time τ_p. Together with v_F, the mean free path $l_p = v_F\tau_p$ can be calculated. With the 2D diffusion constant $D = (1/2)v_F^2\tau_p$, the conductivity can be rewritten in the form of the Einstein relation $\sigma = e^2\mathcal{D}_{2D}D$.

The quantum mechanical nature of a 2DEG system becomes more apparent at temperatures close to absolute zero, when coherence is increased, i.e. when coherence time τ_φ and length $L_\varphi = \sqrt{D\tau_\varphi}$ exceed certain other important length scales like l_p. Then, quantum corrections to the Drude model become important, as will be discussed in Chapter 2.6 about quantum interference effects.

2.1.2 Scattering in Modulation Doped 2DEGs

The main contributions to scattering in a modulation doped 2DEG at a temperature close to absolute zero are: (i) the Coulomb potential of the charged remote donor atoms in the doping layer (spatially separated from the 2DEG) and (ii) charged back-

ground impurity atoms and (iii) neutral impurities or crystal defects, which cannot be completely omitted in MBE growth (ii and iii). Alloy scattering from random Al arrangement in the AlGaAs and interface-roughness scattering at the heterointerface is also present but small. At higher temperature ($T > 10 - 100\,\mathrm{K}$, depending on the mobility), the dominant source is the highly temperature dependent inelastic electron-phonon scattering, inherently reducing the conductivity and causing decoherence.

When independent of each other, the rates $1/\tau_n$ of the individual scattering mechanisms can be summed up to a total scattering rate $1/\tau$ according to Matthiessen's rule:

$$\frac{1}{\tau} = \frac{1}{\tau_1} + \frac{1}{\tau_2} + \frac{1}{\tau_3} ... \tag{2}$$

Thus, the total scattering is dominated by the mechanism with the largest rate.

The transport scattering time τ_p introduced in the previous section is proportional to μ and is a direct measure of the 2DEG conductivity (Drude). It is predominantly accounting for backscattering on short range potential (large scattering angle ϑ). The rate can be written in terms of the scattering potential V and angle ϑ in $\mathbf{k}$-space between the momentum before and after scattering as

$$\frac{1}{\tau_p} = \frac{n_{imp} m^*}{\pi \hbar^3} \int_0^\pi |V(2k \sin(\vartheta/2))|^2 (1 - \cos(\vartheta)) d\vartheta, \tag{3}$$

where n_{imp} is the impurity density [34]. The actual scattering time of a single electron τ_q is called quantum lifetime. It can be much smaller (up to an order of magnitude in the case of small angle scattering) and the rate $1/\tau_q$ has no angle weighting:

$$\frac{1}{\tau_q} = \frac{n_{imp} m^*}{\pi \hbar^3} \int_0^\pi |V(2k \sin(\vartheta/2))|^2 d\vartheta \tag{4}$$

For dominant (large angle) scattering on short range potentials $\tau_q \approx \tau_p$.

2.2 InAs Self-Assembled Quantum Dots

A quantum dot (QD) is a quasi 0-dimensional quantum mechanical system confining electrons (or holes) in all three spatial dimensions, which leads to discrete density of states, exhibiting atom-like characteristics. In GaAs crystals, QDs are formed either electrostatically with lateral gates on the surface or by growing small islands of a semiconductor with different band gap. In this chapter the formation and the main properties of InAs self-assembled QDs (SAQDs), embedded in a GaAs heterostructure, are briefly discussed. Albeit such a QD structure consists of thousands of real atoms, the strong spatial confinement leads to orbital-like states and hence to the term of *artificial atoms*. The wide interest for InAs SAQDs in basic research is based on the fact that due to the small band gap, both electrons and holes can be studied in the same system. In particular bound pairs of electrons and holes and the recombination of such confined excitons are a promising starting point for possible applications like novel lasers, single electron transistors (SET) or optically addressable qubits.

2.2.1 Stranski-Krastanov Growth

The first SAQDs were grown by Leonard *et al.* [35], making use of the growth mechanism observed by Stranski and Krastanov in 1939. It describes the epitaxial growth of atomic layers in the presence of strain. Due to the larger lattice constant of InAs (mismatch of roughly 7%) the MBE deposition of InAs on a GaAs (or AlGaAs) substrate is highly influenced by strain effects. Atoms from the indium and the arsenic source are adsorbed homogeniously (Frank-van der Merve growth) and form a 2D wetting layer (WeL), covering the substrate completely (see Figure 2.2). Depending on temperature and deposition rate, a transition from 2D to 3D growth sets in at a specific critical thickness d_C of the WeL ($\approx$ 1.6 monolayer [36–38]) due to strain release. This leads to a formation of small InAs islands of uniform size and shape [39] with diameters $< 100\,\text{nm}$ and heights of some nm, as schematically shown in Fig. 2.2c. Due to a band

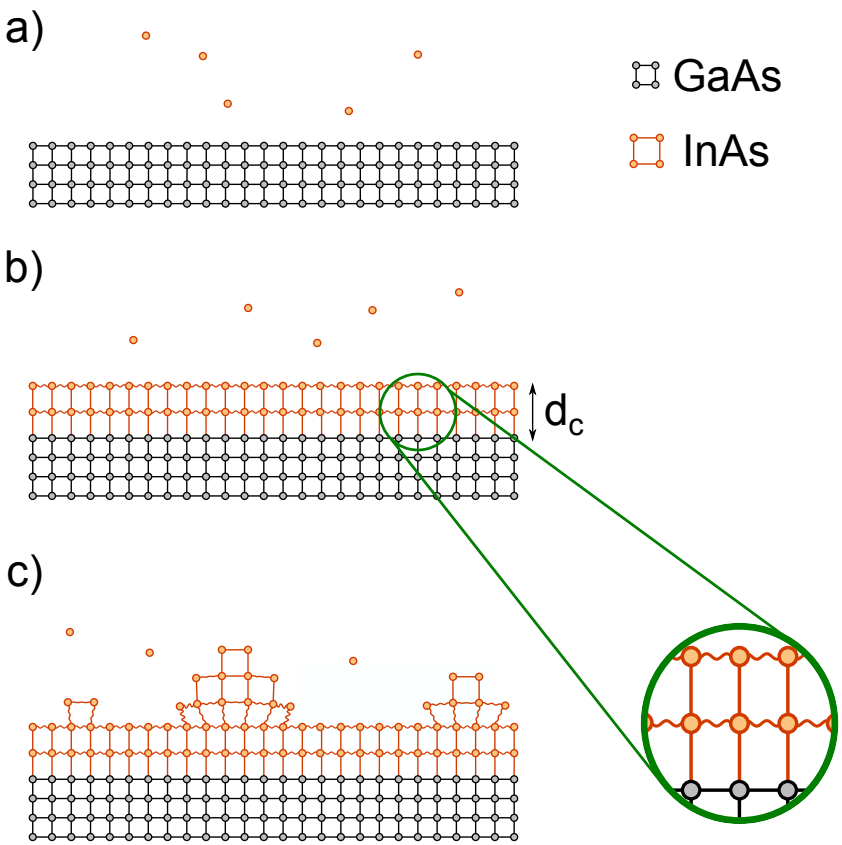

Figure 2.2: Stranski-Krastanov growth of InAs SAQDs. **(a)** In and As atoms (orange) are adsorbed on the GaAs crystal surface (gray lattice) during MBE growth. **(b)** InAs monolayers adopt the crystal lattice of GaAs up to a critical thickness d_C. Due to a lattice mismatch, strain builds up (see zoom-in, wiggly lines). **(c)** InAs continues to grow and forms islands to release strain.

gap smaller than that of the GaAs environment, the local potential well is confined in all three dimensions. The spatial distribution of the InAs SAQDs on the wafer is not site-controlled, however the areal density is dependent on the amount of material deposited. A density gradient is achieved by interrupting substrate rotation during growth, with more material being deposited at places closer to the In and As source.

2.2.2 Quantum Dot Properties

Smallest variations in the parameters during growth affect size, shape, density, etc. of the SAQDs and thus also their actual quantum mechanical properties (level spacing, orbitals, etc.). As a simplified model, we look at a lens-shaped circular island, that is

confined by a parabolic potential

$$V(x,y) = \frac{1}{2} m^* \omega_0 (x^2 + y^2), \tag{5}$$

with ω_0 being the angular frequency of the harmonic potential, in addition to the potential $V(z)$ coming from band offset between GaAs and InAs. The quantum mechanical solution of such a 2-dimensional harmonic oscillator results in eigenenergies of the form

$$E_{n,l} = \hbar\omega_0 (2n + |l| + 1), \tag{6}$$

with $n = 0, 1, 2, ...$ and $l = 0, \pm 1, \pm 2, ...$ describing the radial and the azimuthal quantum number, respectively [40]. Following the notation of atomic orbitals, the lowest energy states (n,l) in such a QD are commonly called s ((0,0), 2 electrons), p ((0,$\pm$1), 4 electrons) and d ((1,0) and (0,$\pm$2), 6 electrons) [40, 41]. For QDs of ellipsoidal or pyramidal shape, $\mathbf{k} \cdot \mathbf{p}$, effective mass oder pseudopotential calculations have to be performed, similarly resulting in a discrete density of states. Experimentally, these energy levels have been probed using spectroscopic methods.

2.2.3 Spectroscopy Methods

There is a vast variety of spectroscopy methods, both optical and electronic techniques, to probe the discrete DOS in SAQDs. The selection of methods presented here is focused on what is needed in Chapters 3 and 4.

Photoluminescence Spectroscopy: The basic principle of photoluminescence (PL) spectroscopy is to measure the recombination of an electron-hole pair following an optical excitation by a laser. In standard PL measurements, the excitation energy is larger than the band gap of the host material $E_{ex} > E_g$. The exciton then relaxes to an energy minimum, before it recombines by emitting a photon (see Fig. 2.3). For InAs SAQDs, electrons and holes relax fast to the lowest energy level in the QD and

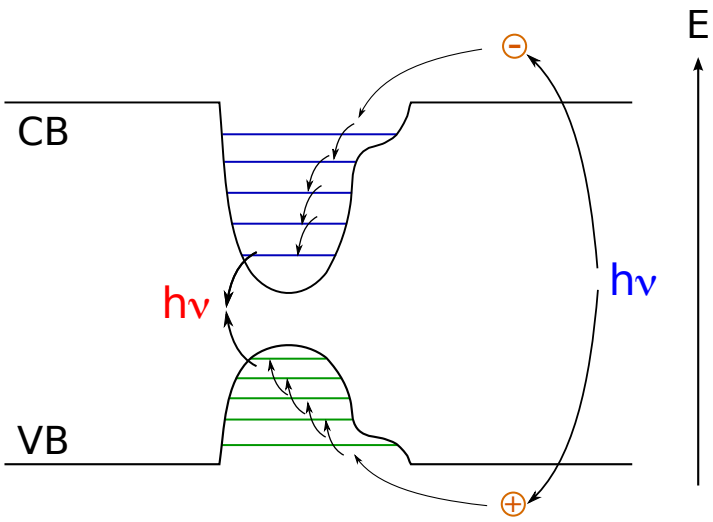

Figure 2.3: Photoluminescence (PL) spectroscopy. In standard PL spectroscopy, an electron hole pair exciton is created by a laser with photon energy larger than the material band gap. The electron/hole relaxes into a conduction band (CB) minimum/valence band (VB) maximum in the SAQD. The small step on the right side of the QD potential represents the InAs wetting layer. The exciton finally recombines by emitting a photon.

therefore mostly the recombination of this state is probed in QD ensembles [42] or single QDs [43]. More elaborated techniques like photoluminescence excitation (PLE), resonant PL (RPL) or time resolved PL (TRPL) spectroscopy are able to probe higher energy levels [44] and the lifetime of these states [45], respectively. Spatial resolution ($< 1\mu m$) is achieved by using microscope lenses in Micro-PL (μ-PL) spectroscopy [46].

Capacitance-Voltage Spectroscopy: This spectroscopy method does not include any optical elements and detects the (electron or hole) addition spectrum electrically. Therefore the capacitance voltage (C-V) spectroscopy [47] is capable of giving specific information about the level spacing in the conduction band (CB) and valance band (VB) [48, 49]. Samples normally consist of a heterostructure containing SAQDs embedded close to a back contact, so that electrons are able to tunnel to this reservoir. On the surface of the sample, a gate electrode (top gate) is added, building a plate capacitor together with the back contact. By applying a voltage to the top gate, an electric field builds up and the QDs are being charged or de-charged. For certain gate voltages, an energy level of the SAQDs is in resonance with the back contact and if

the coupling is strong enough, the QDs are on the same potential. Thus, if resonance is achieved, the effective distance from top gate to the back contact is reduced. This decrease in distance between the two plates results in a slightly increased capacitance C.

Experimentally, the strong coupling is achieved by a small ac-voltage modulation on the dc-voltage of the top gate. The continuous charging/de-charging of the QDs at a resonance leads to a small ac-current, accounting for the increased capacitance. In the C-V plot, peaks appear as a function of the applied dc-voltage for every energy level on top of a larger background capacitance from the device itself. The peaks are broadened by inhomogeneities in the ensemble of SAQDs ($> 10^6$). The back contact is either a n-doped substrate or a 2DEG.

2.3 Quantum Point Contact

2.3.1 Conductance Quantization

A quantum point contact (QPC) is a perfect ballistic 1-dimensional wire connecting two reservoirs, where both length L and width W are in the order of the Fermi wavelength λ_F (see Fig. 2.4a for a schematic of such a device). Experimentally, the (tunable) confinement of a 2DEG into such a short 1D channel was first implemented by Van Wees *et al.* [50] and Wharam *et al.* [51], using gate electrodes. In contrast to earlier split gate experiments, they observed a clear signature of conductance quantization, because both width W and length L were small enough, thus fulfilling the ballistic limit ($l_p > L, W$). In absence of a B-field, the conductance G shows a step-like behavior upon closing the channel by applying a more negative gate voltage V_g, as shown in Fig. 2.4b. Each of the N steps corresponds to a mode, equally contributing to G and therefore summing to

$$G = N\frac{2e^2}{h}, \tag{7}$$

with Planck's constant h. The modes are spin degenerate and carry twice the conductance quantum $G_0 = e^2/h$. Thinking in terms of resistance $R = 1/G$, the concept of measuring a finite resistance in ballistic transport seems to be counterintuitive. However, the actual resistance originates in the coupling from the reservoir to the conducting modes.

The quantization can be calculated by assuming a uniform parabolic confinement potential in $\hat{y}$-direction ($\perp$ current propagation axis $\hat{x}$, see Fig. 2.4a) and the 2DEG confinement in $\hat{z}$-direction $V(\mathbf{r}) = (1/2)m^*\omega_y^2 y^2 + V(z)$. The wave function $\psi(\mathbf{r})$ is then separable into quantized states $\chi_j(y,z)$ and a plane wave $\propto e^{ik_x x}$:

$$\psi_{j,\mathbf{k}} = \chi_j(y,z) \cdot \frac{1}{\sqrt{L}} e^{ik_x x}, \tag{8}$$

where $\sqrt{L}$ is a normalization factor and $j = 1, 2, ...$ is the number of the 1D mode with

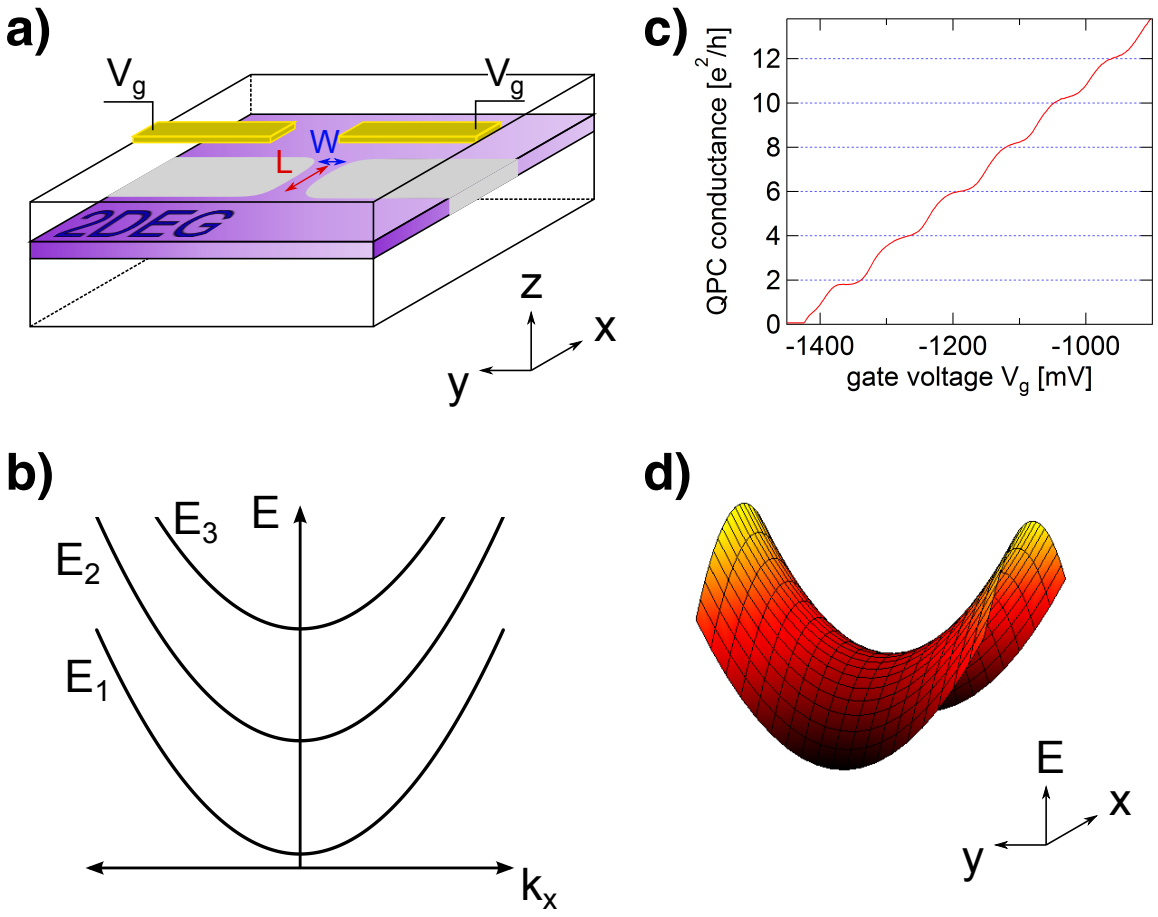

Figure 2.4: Quantum point contact. **(a)** Schematic picture of a QPC device. By applying a gate voltage V_g to the split gates (yellow) the 2DEG (purple) below the gates is depleted (gray area) and a channel of width W and length L forms. **(b)** The QPC conductance decreases in well defined quantized steps ($2e^2/h$) as a function of increasing negative gate voltage V_g. **(c)** The energy dispersion of a 1D waveguide shows discrete equidistant modes and is parabolic. **(d)** A good approximation for the potential landscape in a QPC is a saddle point potential.

energy

$$E_j = \hbar\omega_y(j - \frac{1}{2}). \tag{9}$$

The total energy of an electron with momentum $\hbar k_x$ is $E_{j,k} = E_j + \hbar^2 k_x^2/(2m^*)$, with the dispersion shown in Fig. 2.4c. To calculate the conductance $G = I/U$ of a single channel, the current

$$I = e\int_{\mu_S}^{\mu_D} \mathcal{D}_{1D}(E)v_G(E)dE \tag{10}$$

through the QPC from source (S) to drain (D) due to a small difference in chemical potential $\Delta\mu = \mu_S - \mu_D = eV$ is considered. Here, we assume full transmission and zero temperature, so that the Fermi function drops out and simple integral limits can be used. The energy dependence of the 1D density of states $\mathcal{D}_{1D}(E) = (1/h)\cdot\sqrt{2m^*/E}$ and of the group velocity $v_G(E) = (1/\hbar)\cdot\partial E(k)/\partial k = \sqrt{2E/m^*}$ cancel each other and with current $I = 2e\Delta\mu/h$, the conductance of one channel is exactly $2e^2/h$.

A similar derivation can be done using a saddle point potential $V(\mathbf{r}) = -1/2m^*\omega_x^2 x^2 + 1/2m^*\omega_y^2 y^2 + V(z)$ (Fig. 2.4d), which is a more realistic model for a QPC. The wave function remains separable, however the plane wave along $\hat{x}$ is replaced by a more complicated expression. The energy scale defined by $\hbar\omega_x$ is important for the width of the conductance plateaus and the transition between them, with nice, non-temperature limited plateaus, if criteria $\omega_y/\omega_x > 1$ and $\hbar\omega_x > k_B T$ are fulfilled.

2.3.2 Non-ideal 1D Transport

Unlike the accuracy of the quantum Hall plateaus, the quantization measured in QPCs often is not ideal. Imperfections in the potential landscape can lead to a backscattering probability R, so that the ideal conductance (eq. 7) of each mode j is reduced by the transmission probability factor $T_j = 1 - R_j < 1$

$$G = \frac{2e^2}{h}\sum_j^N T_j. \tag{11}$$

Additionally, a small plateau-like feature is often observed around $0.7\,G_0$. Its exact origin is still controversially discussed [52–55].

2.3.3 QPC Applications

The non-ideal conductance properties may reduce the appeal for metrology applications, however QPC devices have proven to be of great importance in high sensitivity detection experiments, e.g. as charge sensors in lateral QDs [56] or motion detectors in nanomechanical experiments [57]. In the context of spin FETs, the spin filtering aspects of QPCs, which are achieved using high magnetic fields [58] or in presence of strong SO interaction [59] are of wide interest.

2.4 Spin-Orbit Coupling in GaAs 2DEGs

The existence of a coupling between the orbital motion of an electron and its magnetic moment from the spin was first observed as fine structure in atomic spectra. Soon it became clear, that the *spin-orbit interaction* (SOI) is also of great importance in crystalline materials like metals and semiconductors. Comparable to electrons orbiting in the radial E-field of the nucleus in the single atom picture, charge carriers in a crystal move through a potential landscape in the lattice of a 3D crystal or a 2DEG. Relativistically, this E-field $\mathbf{E}$ translates into an effective internal B-field $\mathbf{B}_{\text{int}}$ in the rest frame of the charged particle

$$\mathbf{B}_{\text{int}} = -\frac{1}{c^2}\mathbf{v} \times \mathbf{E}, \tag{12}$$

where $\mathbf{v}$ is the velocity of the charge carrier and c the speed of light. The spin couples to $\mathbf{B}_{\text{int}}$, resulting in a precessional motion.

The effect of the relativistic SOI of electrons (and spin 1/2 particles in general) was successfully implemented into the concepts of quantum mechanics by Dirac and his Lorentz-transformation invariant description of the problem [60]. In a non-relativistic approximation ($pc \ll m_0c^2$) it enters the Schrödinger equation via the Pauli-term

$$\mathcal{H}_{\text{SO}} = \frac{\hbar}{4m_0^2c^2}\hat{\vec{\sigma}}\left(\nabla V \times \mathbf{p}\right). \tag{13}$$

Here, $\vec{\sigma} = (\sigma_x, \sigma_y, \sigma_z)$ are the Pauli matrices, m_0 is the rest mass of the particle, $\nabla V = \mathbf{E}$ describes the electric field and $\mathbf{p}$ is the momentum vector.

It is well known that effects of SO are most pronounced in materials with large atomic number Z, due to the larger Coulomb field of the more positively charged nucleus. The scaling goes roughly with the forth power (Z^4). In semiconductors the same tendency is observed via the SO split-off band of the valence band. The electronic states of the p-like band have different total angular momentum $\mathbf{J}$ (with quantum numbers $j = 1/2$

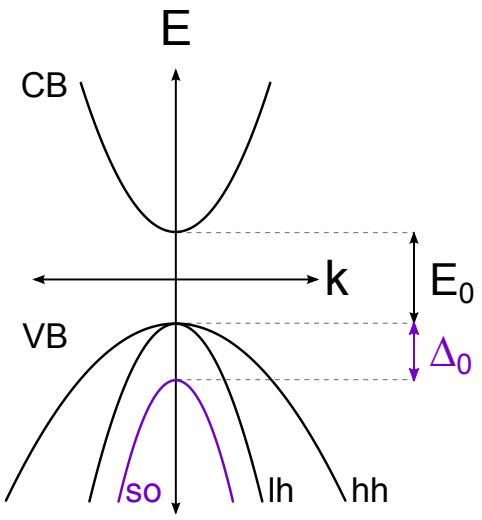

Figure 2.5: Schematic sketch of bulk GaAs band structure around the band gap minimum E_0. Conduction band (CB) and valence band (VB) dispersion are parabolic, with curvature $\propto 1/m_i^*$, the corresponding effective mass of band i. The valence band is split into heavy hole (hh), light hole (hh) and split-off (so) band.

and 3/2) and the lowest band (the one with $j = 1/2$) is split by an energy Δ_0 from the light and heavy hole band ($j = 3/2$), which are degenerate at the Γ point ($\mathbf{k} = 0$), see Figure 2.5. These SO effects can be included in band structure calculations, e.g. via the $\mathbf{k} \cdot \mathbf{p}$ theory [61] and for GaAs one finds $\Delta_0 \approx 340\,\text{meV}$.

The lack of centrosymmetry in the zinc blende structure of III-V crystals introduces an additional splitting in absence of external B-field: The SO coupling lifts the degeneracy of the spin subbands. Two spin eigenstates $\uparrow$ and $\downarrow$ in a crystal are degenerate, if both space inversion symmetry (SIS) and time reversal symmetry (TRS) are not broken. In that case

$$E_\uparrow(\mathbf{k}) = E_\downarrow(\mathbf{k}) \tag{14}$$

and the energy parabola of both spin species are the same (Fig. 2.6a). If the crystal structure however breaks SIS, this degeneracy is lifted and thus:

$$E_\uparrow(\mathbf{k}) \neq E_\uparrow(-\mathbf{k}) \text{ and } E_\downarrow(\mathbf{k}) \neq E_\downarrow(-\mathbf{k}) \tag{15}$$

According to Kramer's theorem, there is still a degeneracy as long as TRS is not broken,

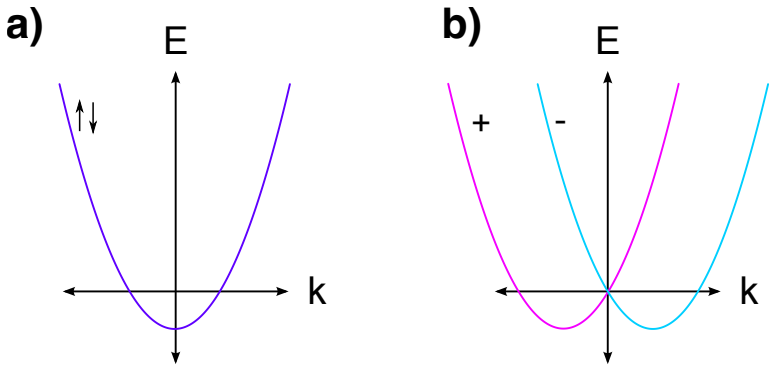

Figure 2.6: Zero-field splitting. **(a)** Degenerate energy dispersion in centrosymmetric crystals. **(b)** Dispersion relation splits into two branches, if spatial symmetry is broken.

leading to

$$E_+(\mathbf{k}) = E_-(-\mathbf{k}) \tag{16}$$

and hence to a horizontal shift of the energy parabola in $\mathbf{k}$-space, as shown in Fig. 2.6b. This is consistent with the picture of an effective SO field $\mathbf{B}_{\text{eff}}(\mathbf{k})$ and a total Hamiltonian (including the SO term $\mathcal{H}_{SO}$) that maintains TRS. In eq. 16 the eigenstates $\uparrow, \downarrow$ are replaced by $+$ and $-$, because the the quantization axis of the SO coupled spin is a function of momentum.

As described by eq. 13 and will be discussed in the following Chapters (2.4.1, 2.4.2 and 5), the main sources of SOI are electric fields, originating from asymmetries such as gradients in the Coulomb potential ∇V of the heterostructure bands and the crystal, respectively. Therefore, it is an intrinsic effect, strongly depending on the material and its structure.

Diffusive electrons experience fluctuating fields and thus, SOI leads to unwanted spin relaxation and decoherence in solid state systems. However, external E-fields provide an additional knob to gain (limited) in-situ control on SOI. In the context of cryogenic experiments, this enables spin resonance experiments without the need of complicated high frequency magnetic fields not only in QDs [62–64], but also in 2DEGs [65–67]. Moreover, SOI is also important for the observation of the relativistic *zitterbewegung* [68] and is one of the key ingredients for the creation of Majorana bound states [69, 70],

which are possible candidates for topological quantum computation due to their non-Abelian statistics.

2.4.1 Rashba-Type Spin-Orbit Interaction

One of the effects breaking spatial inversion symmetry is the Rashba effect [71]. It describes the SO splitting in a 2DEG due to an inversion asymmetry of the confinement potential along the growth direction ($\hat{z}$) from an average E-field $\langle E_Z \rangle$, perpendicular to the 2D plane. For a [001] grown QW, the Rashba Hamiltonian

$$\mathcal{H}_{\mathrm{SO}}^{\mathrm{R}} = \alpha \left(\sigma_x k_y - \sigma_y k_x \right) \tag{17}$$

is linear in components of wave vector $\mathbf{k}$, with coefficient α, the Rashba SO coefficient. The structural inversion asymmetry (SIA) is present in all non-symmetric heterostructures, stemming from potential offsets of the different materials, the Coulomb field from 2DEG electrons and the charged donor atoms in the doping layer. Additional contributions from externally applied E-fields [72–74] and strain-induced SO are also of Rashba type [75, 76] and allow for in-situ tunability. Rashba splitting can be avoided ($\alpha = 0$) by growing QWs symmetrically or by compensating internal fields with an external potential.

The effective magnetic field $\mathbf{B}_{\mathrm{int}}^{\mathrm{R}}(\mathbf{k})$ shifts the spin subbands in k-space by $2m^*\alpha/\hbar^2$ (Fig. 2.7), resulting in an energy splitting of $\Delta E_{SO} = 2\alpha k_F$. The B-field is in-plane and always perpendicular to the electron momentum

$$\mathbf{B}_{\mathrm{int}}^{\mathrm{R}} = \frac{2\alpha}{g\mu_B} \begin{pmatrix} k_y \\ -k_x \end{pmatrix} \tag{18}$$

with the Bohr magneton μ_B and the electron g-factor g. In Figure 2.7b the effective Rashba field in $\mathbf{k}$-space is shown for the situation, where the SO spin splitting is small compared to the Fermi energy $\Delta E_{SO} \ll E_F$.

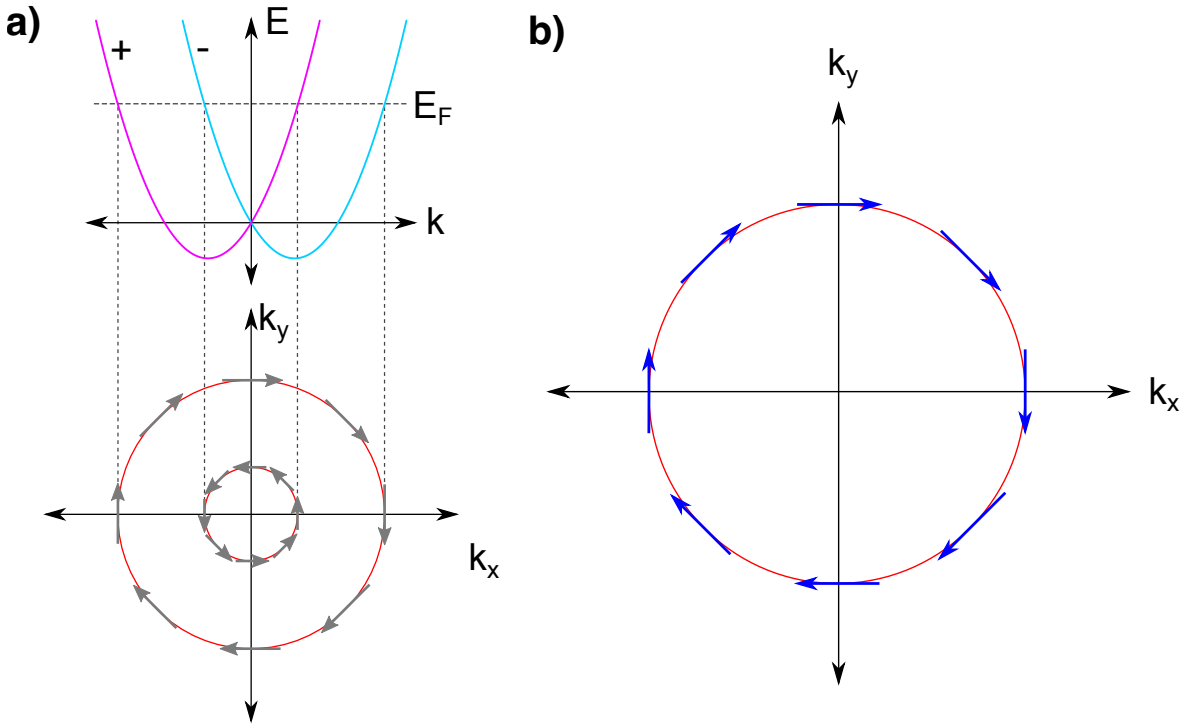

Figure 2.7: Rashba SO energy splitting and effective field. **(a)** Rashba induced splitting of the energy dispersion relation. Cutting the energy parabolas (paraboloids in 2D) at a fixed value, reveals two concentric circles (red) in the 2D-plane for each of the two (antiparallel) eigenstates (indicated by gray arrows). **(b)** Effective B-field $\mathbf{B}_{\text{int}}^{\text{R}}$ (blue) as a function of $\mathbf{k}$. The red circle indicates the possible wave vectors of the electrons, using $k_x^2 + k_y^2 = k_F^2$. If the energy splitting due to SOI is small compared to $E_F = \hbar^2 k_F^2/(2m^*)$, this is a good approximation.

2.4.2 Dresselhaus-Type Spin-Orbit Interaction

The Dresselhaus Hamiltonian [77] describes the second important contribution to SO in GaAs, originating from bulk inversion asymmetry (BIA) of the crystal. The Hamiltonian accounting for the zinc blende structure is cubic in $\mathbf{k}$

$$\mathcal{H}_{\mathrm{SO}}^{\mathrm{D}} = \gamma \left(\sigma_x k_x k_z^2 - \sigma_x k_x k_y^2 + \sigma_y k_y k_x^2 - \sigma_y k_y k_z^2 + \sigma_z k_z k_y^2 - \sigma_z k_z k_x^2 \right), \tag{19}$$

with Dresselhaus coefficient γ and crystal directions $\hat{x} \| [100]$, $\hat{y} \| [010]$ and $\hat{z} \| [001]$. In a 2DEG or QW, electrons are confined along $\hat{z}$, thus the z-component of the wave vector operator k_z can be replaced by its expectation value $\langle k_z \rangle = \langle -\partial_z \rangle = 0$ [78]. With the same argument, $k_z^2 = \langle k_z^2 \rangle$ and by using $\beta_1 = \gamma \langle k_z^2 \rangle$ the Dresselhaus Hamiltonian can be separated into a linear and a cubic (in $\mathbf{k}$) term:

$$\mathcal{H}_{\mathrm{SO}}^{\mathrm{D1}} = \beta_1 \left(\sigma_x k_x - \sigma_y k_y \right) \tag{20}$$

$$\mathcal{H}_{\mathrm{SO}}^{\mathrm{D3}} = \gamma \left(\sigma_y k_y k_x^2 - \sigma_x k_x k_y^2 \right) \tag{21}$$

In contrast to the Rashba contribution, the Dresselhaus effect is a material property, therefore less tunable and rather weak in bulk GaAs. Since $\langle k_z^2 \rangle \propto 1/W^2$, by increasing the 2D confinement (going to more narrow QW widths W), the QW can be designed such as the Dresselhaus effect becomes of comparable strength as the Rashba contribution. The coefficient γ is difficult to determine and values both measured and calculated range from $7.6\,\mathrm{eV\AA}^3$ up to $34.5\,\mathrm{eV\AA}^3$ (see table in supplementary material of Ref. [79]). It is a bulk material parameter but could also depend on confinement, as observed e.g. in Ref. [80]. The cubic Dresselhaus Hamiltonian is strongly density dependent, because in 2DEGs $k_F = \sqrt{2\pi n}$.

Again, these Hamiltonians can be expressed as effective magnetic fields and we can

assume that $\Delta E_{SO} \ll E_F$. The linear Dresselhaus field is of the form

$$\mathbf{B}_{\text{int}}^{\text{D1}} = \frac{2\beta_1}{g\mu_B} \begin{pmatrix} k_x \\ -k_y \end{pmatrix} \tag{22}$$

and displayed in Fig. 2.8a. It is of constant magnitude, but the field vector rotates by 2π, when going around the Fermi circle. The cubic field has the form

$$\mathbf{B}_{\text{int}}^{\text{D3}} = \frac{2\beta_3}{g\mu_B} \begin{pmatrix} -k_x k_y^2 \\ k_y k_x^2 \end{pmatrix} \tag{23}$$

and is shown in Fig. 2.8b. Similar to the Rashba field, it is always perpendicular to $\mathbf{k}$, but its magnitude oscillates as a function of angle θ between $\mathbf{k}$ and k_x.

If we rewrite $\mathcal{H}_{\text{SO}}^{\text{D3}}$ in polar coordinates, using $k_x = k_F \cos(\theta)$ and $k_x = k_F \sin(\theta)$, we find

$$\mathcal{H}_{\text{SO}}^{\text{D3}} = \frac{\gamma k_F^3}{4} \left[\sigma_y \left(\sin(3\theta) + \sin(\theta)\right) - \sigma_x(-\cos(3\theta) + \cos(\theta))\right]. \tag{24}$$

One can separate the terms of first harmonic and third harmonic order and by using $\beta_3 = k_F^2/4$ re-express eq. 24 as two terms:

$$\mathcal{H}_{\text{SO}}^{\text{D3,1st}} = -\beta_3 \left(\sigma_x k_x - \sigma_y k_y\right) \tag{25}$$

$$\mathcal{H}_{\text{SO}}^{\text{D3,3rd}} = \frac{\gamma k_F^3}{4} \left[\sigma_y \sin(3\theta) + \sigma_x \cos(3\theta)\right] \tag{26}$$

Comparing eq. 25 (1st order harmonic term) with eq. 20, we find that these Hamiltonians have the same symmetry. The internal B-field (Fig. 2.8c) is proportional to β_3 and is of opposite sign, compared to $\mathbf{B}_{\text{int}}^{\text{D1}}$. Combining the two fields, we can write a total effective magnetic field

$$\mathbf{B}_{\text{int}}^{\text{D,1st}} = \frac{2\beta}{g\mu_B} \begin{pmatrix} k_x \\ -k_y \end{pmatrix}, \tag{27}$$

with total $\beta = \beta_1 - \beta_3$. To visualize this total vector field, also Figure 2.8a can be used. The third order harmonic Hamiltonian (eq. 26) reads as

$$\mathbf{B}_{\text{int}}^{\text{D,3rd}} = \frac{\gamma k_F^3}{2g\mu_B} \begin{pmatrix} \cos(3\theta) \\ \sin(3\theta) \end{pmatrix} \tag{28}$$

and has a different symmetry, as can be seen in Fig. 2.8d. The field rotates by a total angle of 6π when going around the Fermi circle.

2.4.3 The Regime of Equal Rashba and Dresselhaus Strength

In narrow GaAs QWs the Rashba and Dresselhaus internal B-fields are of comparable size. For the special case of an exact matching ($\alpha = \pm\beta$) and in absence of any cubic contributions ($\beta_3 = 0$), the Hamiltonian can be rewritten as

$$\mathcal{H}_{\text{SO}} = \alpha(\sigma_x - \sigma_y)(k_x + k_y). \tag{29}$$

Here, $\alpha = +\beta$. Rotating the coordinate system by $\pi/4$ by introducing $k_\pm = 1/\sqrt{2}\,(k_y \pm k_x)$ and a global spin rotation by $\hat{U} = 1/\sqrt{2}\left[1 + \left(i/\sqrt{2}\right)(\sigma_x + \sigma_y)\right]$ the total Hamiltonian $\mathcal{H} = \mathcal{H}_0 + \mathcal{H}_{\text{SO}}$ of an electron in a 2DEG reads

$$\mathcal{H} = \frac{\hbar^2\left(k_+^2 + k_-^2\right)}{2m^*} - 2\alpha\sigma_- k_+ + V(\mathbf{r}) \tag{30}$$

and a situation of exact SU(2) spin rotation symmetry arises [81]. The potential $V(\mathbf{r})$ describes further confinement into a wire, QPC or QD structure and $\sigma_- = 1/\sqrt{2}(\sigma_x - \sigma_y)$ is the rotated spin basis.

Before discussing the physical consequences of the additional symmetries, a more intuitive interpretation in the picture of the effective internal B-field is given. Adding up the two internal SO-fields $\mathbf{B}_{\text{int}}^{\text{R}}$ (Fig. 2.9a) and $\mathbf{B}_{\text{int}}^{\text{D,1st}}$ (Fig. 2.9b) with equal strength ($\alpha = \beta$), results in a total B-field which is uniaxial. As shown in Figure 2.9c, the vectors are all parallel to the k_--axis and are adding up to twice the strength of the

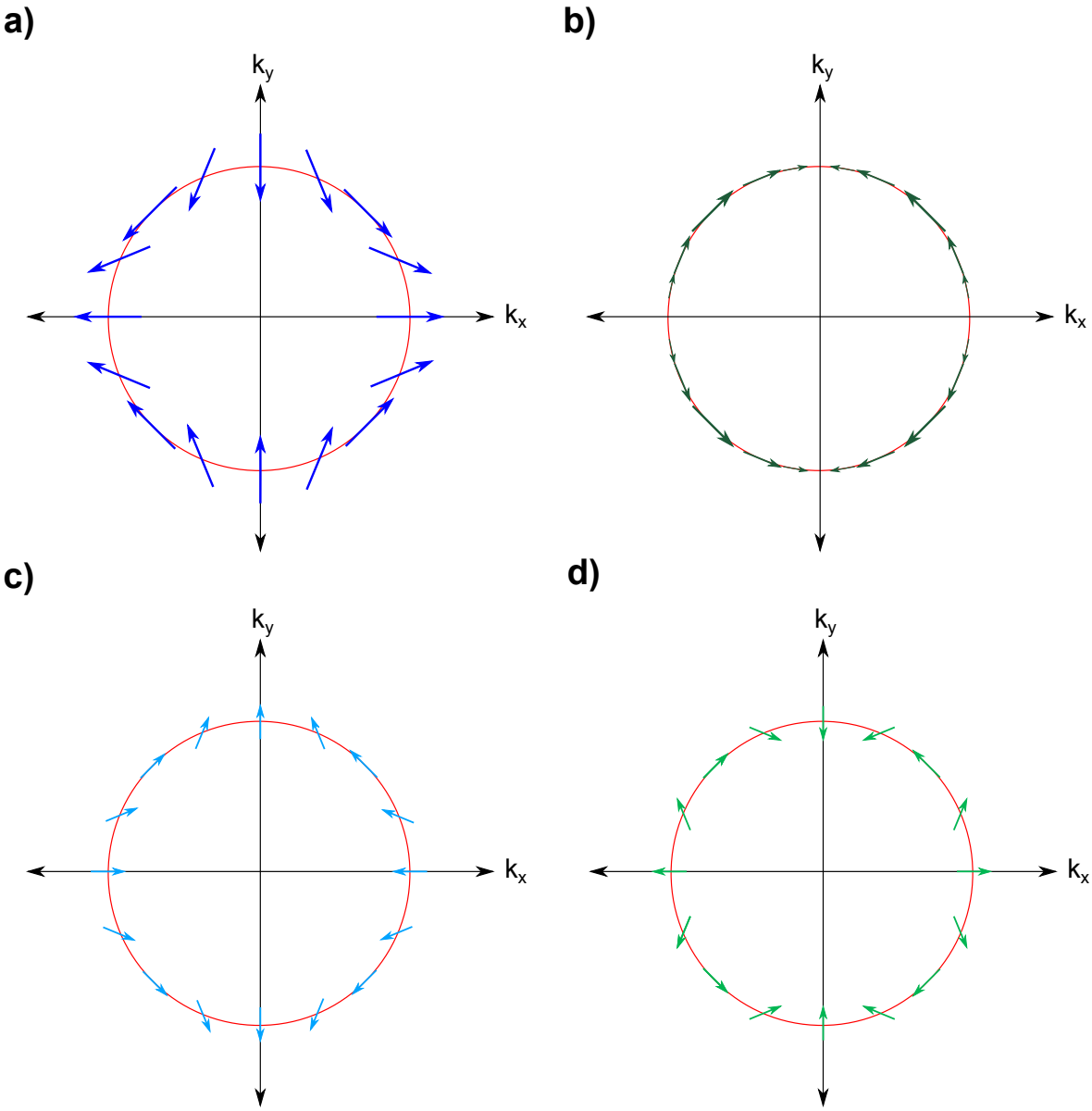

Figure 2.8: Effective Dresselhaus fields in k-space. **(a)** The vector of the linear effective Dresselhaus field rotates by 2π, when going around the k_F circle (red). **(b)** The total cubic B-field is always perpendicular to **k** (comparable to Rashba field), but its strength changes with **k**. **(c)** The first harmonic of the cubic term has the same angular symmetry as the linear term in **a**, but opposite sign, while the third harmonic field in **(d)** rotates by 6π on the k_F circle.

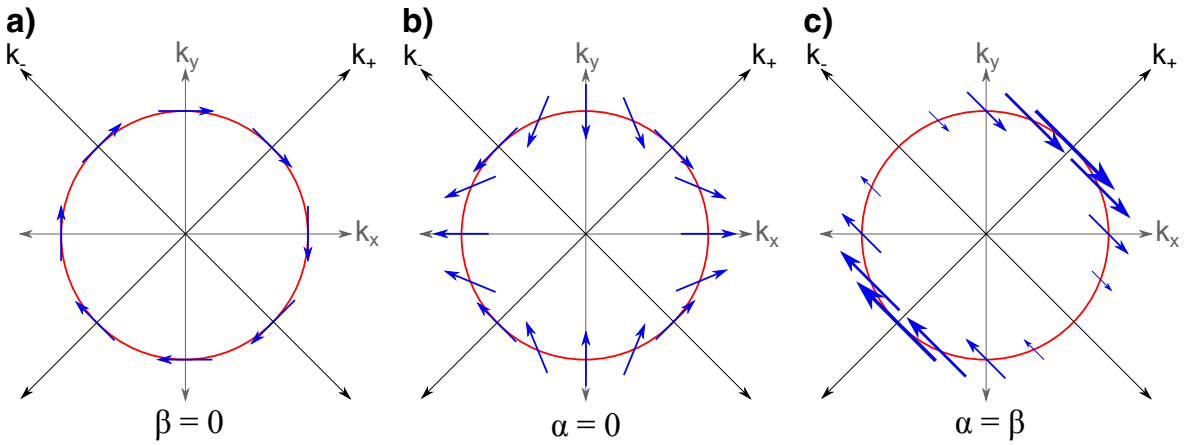

Figure 2.9: Interplay of SIA and BIA effective SO fields in k-space. **(a)** The geometry of the Rashba field in absence of Dresselhaus contribution ($\beta = 0$) is always perpendicular to $\mathbf{k}$. **(b)** The direction of the pure Dresselhaus field ($\alpha = 0$) changes from parallel to perpendicular as a function of $\mathbf{k}$. **(c)** Adding up the two fields from **b** and **c** with equal strength ($\alpha = \beta$) results in an uniaxial B-field $\mathbf{B}_{\text{int}}$.

individual fields at k_+, while they cancel on the k_--axis. The energy paraboloids, which split isotropically in k-space, if only either Rashba or Dresselhaus is concerned (see Fig. 2.7a for the Rashba case), become anisotropic and split on the k_+-axis by a total of $q = 4m^*\alpha/\hbar^2$ [82]. The energy splitting in presence of both SO contributions is given by $\Delta E = 2k\sqrt{\alpha^2 + \beta^2 + 2\alpha\beta\cos(2\theta)}$, with θ being the angle between k_+ and wave vector $\mathbf{k}$. In GaAs QWs this splitting is usually much smaller than the Fermi energy and momentum $\hbar k_F$ for all electrons is a very good approximation.

Schliemann *et al.* have shown, that for the Hamiltonian in eq. 30 a momentum independent wave function exists and thus, the spin is robust against randomization due to scattering [30]. The rotation symmetry of a spin returning to its origin was later identified to be of $SU(2)$ type by Bernevig *et al.* [81]. As already described, $\mathbf{B}_{\text{int}}$ is uniaxial, leading to a fixed precession axis for all electron spins. The total precession angle only depends on the net displacement in $\hat{x}_+$-direction ($\|k_+$) and has periodicity $\frac{\hbar^2\pi}{2m^*\alpha}$. Hence, starting with a spin at position $\mathbf{r}_1$ and going an arbitrary way to point $\mathbf{r}_2$ always results in the same precession angle, independent of the path the electron takes. Returning to $\mathbf{r}_1$, the spin rotation is undone. Moreover, spins parallel to $\hat{x}_-$ do not precess at all.

2.4.4 Other Spin-Orbit Terms

Apart from BIA and SIA discussed before, there are other sources of SOI in GaAs heterostructures. One of them is strain induced SOI, which up to some degree can also be understood as a breaking of both structural and bulk symmetry [75]. Its contribution can therefore be incorporated via the Rashba and Dresselhaus Hamiltonians and is weak in GaAs samples, which are grown strain-free.

Of more complex nature are interface contributions, that come from local reduction of the crystal symmetry at the GaAs/AlGaAs interface [61, 83]. The microscopic interface asymmetry (from D_{2d} to C_{2v}) leads to a mixing of heavy and light hole states and in third order $\mathbf{k} \cdot \mathbf{p}$ to a spin splitting in the conduction band [83]:

$$\begin{aligned} \mathcal{H}_{6c6c} = \pm h_{x-y} \frac{P^2}{3{E_0}^2} \Bigg\{ & \left(1 + \frac{2E_0}{(E_0 - \Delta_0)}\right) \delta(z - z_i) k_x k_y \mathbb{1}_{2\times 2} \\ & + i \left(\frac{1}{2} - \frac{E_0}{2(E_0 - \Delta_0)}\right) [k_z, \delta(z - z_i)](k_x \sigma_x - k_y \sigma_y) \Bigg\} \end{aligned} \tag{31}$$

As earlier E_0 and Δ_0 are parameters given by the band gap and the SO split-off band, respectively. Additionally, the Kane parameter P and h_{x-y} are also material parameters, with the latter describing the interface at position z_i. The second term has the same symmetry as the first harmonic Dresselhaus term. Depending on the material, the interface contribution is small and for a 10 nm GaAs QW a splitting of 0.02 meV was calculated [83], usually much smaller than the linear Dresselhaus term. Therefore, interface effects and also strain effects are not considered in Chapter 5.

2.5 Spin-Orbit Spin Relaxation Mechanisms

Indeed, SO coupling leads to spin relaxation and thus can also result in spin decoherence in semiconductors. For future spintronic applications it is important to understand these spin equilibration processes. One can distinguish between two fundamentally different mechanisms for spin relaxation caused by SOI: (1) The Elliott-Yafet (EY)

mechanism [84], that describes spin-flips occurring at phonon and/or impurity scattering (Fig. 2.10a) and (2) the D'Yakonov-Perel' (DP) type of spin relaxation, only present in absence of inversion asymmetry (SIA, BIA and strain), originating in the randomization of the spin precession axes $\mathbf{B}_{\text{eff}}$ as described above and depicted in Fig. 2.10b.

In principle both mechanism are present in GaAs and other zinc blende III-V semiconductors, with one dominating over the other. The fundamental criterion to identify the predominant type is via the dependence on momentum scattering time of an electron τ_p. The spin flips of EY can only occur directly at a scattering event (see Fig. 2.10a) and therefore the spin relaxation rate $1/\tau_s \propto 1/\tau_p$. For the DP mechanism on the other hand one finds that $1/\tau_s \propto \tau_p$, resulting in an enhanced spin lifetime τ_s in presence of disorder (short τ_p). Indeed, this *motional narrowing* effect is only observed if the mean of the Larmor precession rate $|\mathbf{\Omega}|$ is smaller than $1/\tau_p$, so that the total spin precession between two momentum changes $|\Omega|\tau_p \ll 1$ and does not complete a full rotation. The spin evolution is then comprised of small precessional movements around randomly fluctuating precession axes, described by a 2-dimensional *random walk* on the Bloch sphere. The average step size of the small rotation between consecutive scattering events is $\delta\varphi = \bar{\Omega}\tau_p$. Here $\bar{\Omega}$ is the mean of $\mathbf{\Omega}(\mathbf{k})$ in k-space. After time t and $N = t/\tau_p$ steps, the mean square angular deviation is $\langle\Delta\varphi^2\rangle = N\bar{\Omega}^2\tau_p^2$. By defining the spin relaxation length τ_s as the time t that is needed for $\sqrt{\langle\Delta\varphi^2\rangle} = 1\,\text{sr}$ ($\sqrt{N}$ steps), one gets the relation $1/\tau_s = \bar{\Omega}^2\tau_p$.

Additional spin relaxation mechanisms are the Bir-Aronov-Pikus mechanism (spin-flips via electron-hole exchange, predominantly in p-type material [85]) and hyperfine interaction (coupling to nuclear spin fluctuations [86]), both independent of SO coupling. For non-centrosymmetric n-type bulk semiconductors there is a competition between EY and DP [87] because of different dependence on band gap energy E_g and SO-split-off energy Δ_w. But not only material properties like crystal symmetry and band gap size are important. Both DP and EY exhibit distinct T-dependence, depending on the

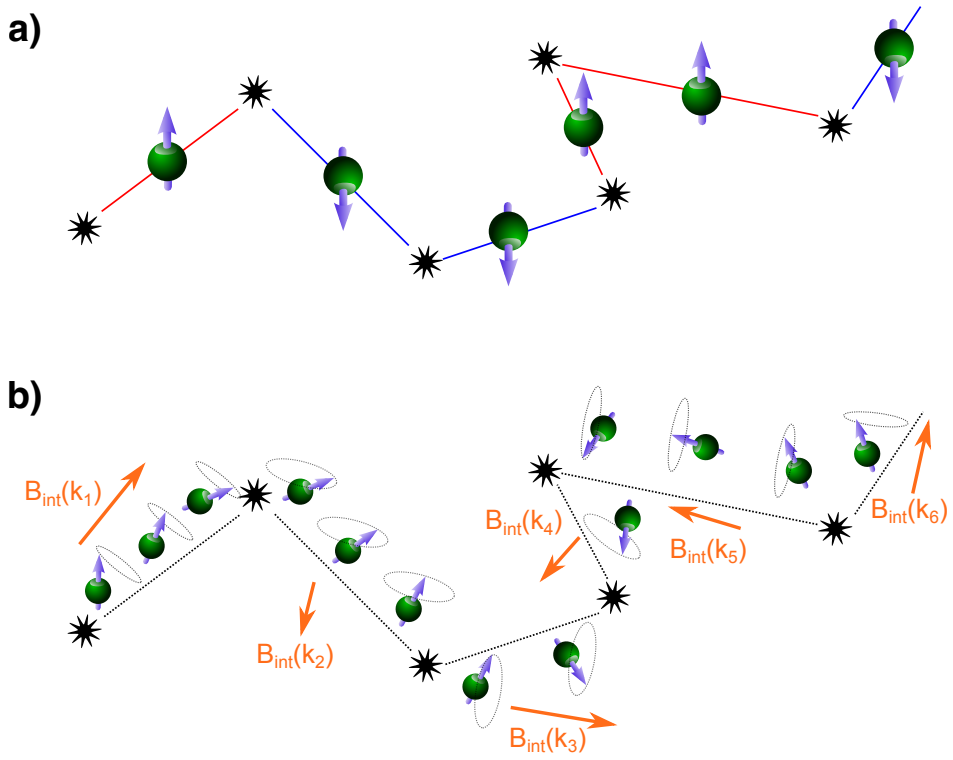

Figure 2.10: SO spin relaxation mechanisms. **(a)** Elliott-Yafet mechanism: electron spin relaxation may occur as spin-flips process at scattering events due to mixing of spin up and down states (no pure eigenstates in presence of SO, described by Elliott) or in the E-field of charged impurities (Yafet). Red (spin up) and blue (spin down) lines indicate absence of spin relaxation between the scattering events. **(b)** D'Yakonov-Perel' mechanism: randomly fluctuating effective (internal) SO field $\mathbf{B}_{\text{int}}$ (orange arrows) as a function of wave vector $\mathbf{k}_i$. Here, the precession axis changes after every scattering process, leading to *motional narrowing*.

presence of specific scattering mechanisms at different temperatures [88]. This gives further information about the type of spin relaxation. In the case of (asymmetric) GaAs/AlGaAs QWs discussed in Chapter 5, both Rashba and Dresselhaus SO coupling contributions determining the strength of Larmor precessions Ω are sufficiently strong and spin relaxation occurs via DP.

2.5.1 Signatures of SOI in Transport Measurements

If spin lifetime in a 2DEG is dominated by SOI, optical spin polarization decay measurements are a powerful tool to investigate this effect. In combination with transport experiments, it is possible to determine the relative strength of the Rashba and Dresselhaus effects by measuring the angle dependence of the spin-galvanic photocurrent [89] up to room temperature.

At low temperature, the beating pattern in the Shubnikov-de Haas (SdH) oscillations provides a direct way to determine SO strength in quantum transport measurements [90], if the zero field splitting is large. A more sensitive tool is presented in the next Chapter: weak antilocalization (WAL), a quantum interference effect due to spin. Both SdH beating and WAL have been shown to be tunable via externally applied electric fields [72, 91].

Further, the SO induced spin separation in 2D transport, in analogy to the Hall effect called *spin Hall effect* (SHE) [92], is also of interest. Apart from the *extrinsic* SHE (skew scattering at charged impurities), the *intrinsic* SHE is a measure of BIA and SIA contributions [93]. However, spin polarization detection in GaAs/AlGaAs 2DEGs is a non-trivial experimental challenge.

2.6 Quantum Interference Effects in Diffusive 2D Electron Transport

As briefly mentioned in Chapter 2.1, there are corrections to the classically derived Drude conductivity of diffusive 2D transport, accounting for the quantum nature and interactions of the charge carriers. At low temperature ($k_B T \ll \hbar/\tau_p$), in absence of magnetic fields and neglecting spin, the total correction to conductivity is [94, 95]

$$\delta\sigma(T) = \frac{e^2}{2\pi^2\hbar}\left[\ln\left(\frac{\tau_p}{\tau_\varphi(T)}\right) + \left(1+\frac{3}{4}\lambda\right)\ln\left(\frac{k_B T\tau_p}{\hbar}\right)\right]. \tag{32}$$

The first term describes the interference correction due to coherently back-scattered electrons. The coherence time τ_φ is strongly temperature dependent and in the low-T regime $\tau_\varphi^{-1} \propto T$, dominated by the quasi-elastic Nyquist type of electron-electron scattering [96]. In the second term, the contribution of electron-electron interactions (EEI) is covered, with parameter λ accounting for the interaction [97]. Both of these corrections do not only depend on temperature, but also have characteristic B-field dependence $\delta\sigma(B)$. In the following, the quantum interference effect of back-scattered electrons, leading to weak corrections in the low field limit of magnetoconductance (MC), is discussed in more detail (Chapter 2.6.1). The additional effect of the spin is included in Chapter 2.6.2. The magnetoresistance from EEI is parabolic and has a larger field scale. At the critical field $B_C = 1/\mu$ the correction is zero (pure Drude conductivity).

2.6.1 Weak Localization

The effect of weak localization (WL) is a negative quantum correction to conductance in the order of $\delta\sigma = e^2/h$. Its origin lies in the coherently back-scattered (spin-less) electron wave functions, interfering constructively with each other [98]. This is the case if the electron mean free path l_p is smaller than the coherence length L_φ. It

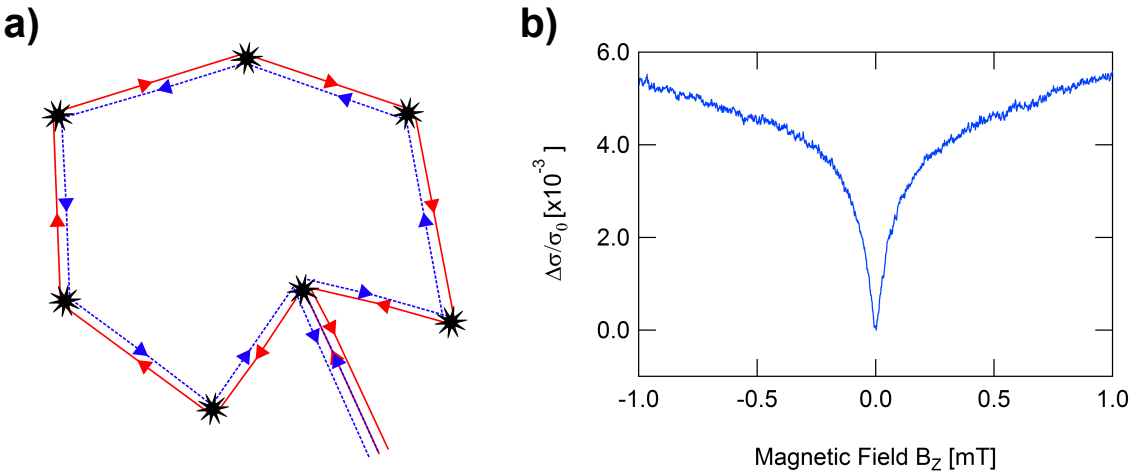

Figure 2.11: Weak localization (WL). (a) In a spin-less system, a constructive interference of two backscattered electrons leads to a increased probability of backscattering, as electrons traveling same path but in opposite direction (red and blue path) pick up the same phase. **(b)** Applying a magnetic field B_Z perpendicular to the 2DEG plane adds an Aharonov-Bohm phase and destroys the constructive nature of the effect. Thus, the signature of WL is a (local) minimum in magnetoconductance at $B_Z = 0$.

is a consequence of the quantum mechanical treatment of the Feynman path return probability amplitudes. In Figure 2.11a an example of such a closed path is shown. Back-scattered electrons can travel along a direct and also a time-reversed but otherwise identical path, each path described by its quantum mechanical amplitude A^+ (direct) and A^- (time reversed). According to this, the probability of returning to the starting point is

$$|A^+ + A^-|^2 = |A^+|^2 + |A^-|^2 + A^+A^{-\star} + A^{+\star}A^-. \tag{33}$$

If the system has time-reversal symmetry ($A^+ = A^- = A$), the total probability is $P = 4|A|^2$. The classical probability is only $2|A|^2$, by a factor of 2 smaller, because the last two interference terms in eq. 33 are zero for incoherent addition of probabilities. The sum over all paths leads to an increased probability to find an electron at the origin, and hence to a reduced conductivity.

The symmetry is lifted by a perpendicular magnetic field B_Z. An Aharonov-Bohm (AB) phase of $\varphi_{AB} = 2e\pi/h \cdot (BS)$ is introduced by the flux through the area S of the

closed loop. The return probability

$$|A^+(B) + A^-(B)|^2 = 2|A|^2 + 2|A|^2 \cos\left(4\pi \frac{BSe}{h}\right) \tag{34}$$

is modulated periodically. Effectively, a large number of different paths with a wide distribution of areas spanned (and hence different AB flux/phase) is contributing. The periodicity averages out when all these paths are considered and the total change in conductance reads [99, 100]

$$\delta\sigma(B_Z) - \delta\sigma(0) = \frac{e^2}{2\pi^2\hbar}\left[\Psi\left(\frac{1}{2} + \frac{\hbar}{4eDB_Z\tau_\varphi}\right) - \Psi\left(\frac{1}{2} + \frac{\hbar}{4eDB_Z\tau_p}\right) + \ln\left(\frac{\tau_\varphi}{\tau_p}\right)\right], \tag{35}$$

with digamma function $\Psi(x)$ and diffusion constant D. As can be seen in Fig. 2.11b, the relative conductance changes as a function of B_Z and the effect of WL is suppressed by the B-field, because pathways larger as the magnetic length $l_m = \sqrt{h/(2eB_Z)}$ do no longer contribute to WL.

2.6.2 Weak Antilocalization

Considering also the spin in the WL description, time-reversal symmetry of two counter-propagating paths is broken by some non-symmetric B-fields, i.e. the effective SO field $\mathbf{B}_{\text{int}}(\mathbf{k})$. In the presence of strong SOI (SO-length $\lambda_{SO} \leq l_p$), the spin precession axis experiences a change after each scattering event and completing the path, the final spin state $|f\rangle = R_n \cdot ... \cdot R_3 \cdot R_2 \cdot R_1|i\rangle$ is given by the total rotations acting on the initial state $|i\rangle$ (see Fig. 2.12a). The time-reversed path picks up a different precession, given by $|f_{TR}\rangle = {R_1}^{-1} \cdot {R_2}^{-1} \cdot {R_1}^{-1} \cdot ... \cdot {R_n}^{-1}|i\rangle$ [98]. Due to the fermionic character of the electrons (obeying the Pauli exclusion principle) a spin rotating by 2π picks up an additional phase of -1, thus a total precession of $4\pi m$ (with $m = 0, 1, 2, ...$) is needed for constructive interference. For spin rotations of $2\pi m$, Fermions interfere destructively. As a consequence of summing up all the interfering paths, the total sign of this quantum correction is positive (dip in MC, see Fig. 2.12b)

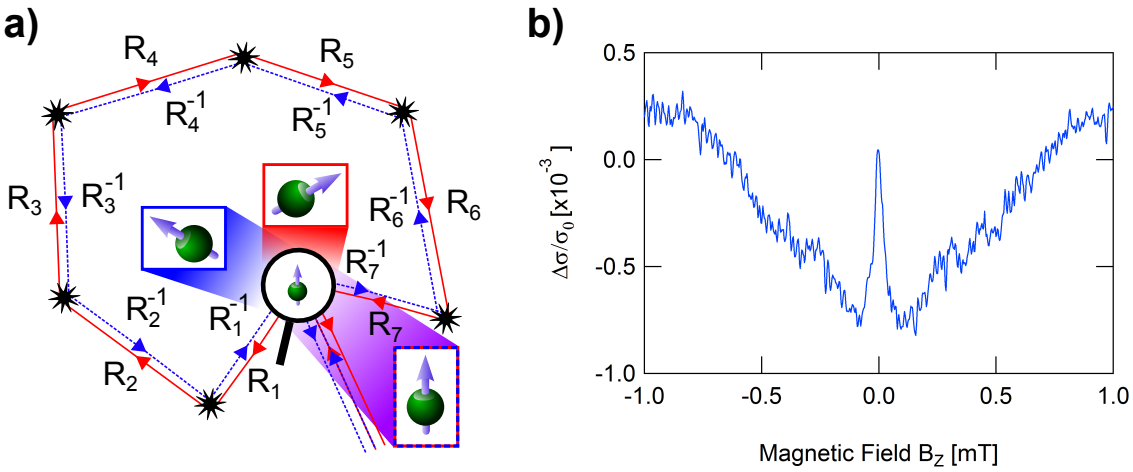

Figure 2.12: Weak antilocalization (WAL). (a) The spin precession (e.g. in a random effective SO-field $B(k)$) of two coherently backscattered electrons around the same path but in opposite direction (red and blue) results in destructive interference, because of non-commutativity of the rotations R_i. **(b)** Due to this spin interference, the magnetoconductance has a local maximum at $B_Z = 0$.

and therefore the effect is denoted as weak antilocalization (WAL).

As a second consequence the maximal magnitude of the WAL correction is reduced by a factor of 2, if compared to WL and the field scale is connected to the SO time τ_{SO} and SO length $l_{SO} = \sqrt{D\tau_{SO}}$, since only paths with $l_{SO} < l_\varphi$ are contributing. An expression for the total correction by interference terms as a function of the applied perpendicular field was first given by Hikami, Larkin and Nagaoka (HLN). For strong SOI ($\tau_\varphi \gg \tau_{SO}$) and in the low mobility regime ($\tau_\varphi \gg \tau_p$)

$$\delta\sigma(B_Z) - \delta\sigma(0) = a\frac{e^2}{2\pi^2\hbar}\left[\Psi\left(\frac{1}{2} + \frac{\hbar}{4eDB_Z\tau_\varphi}\right) - \ln\left(\frac{\hbar}{4eDB_Z\tau_\varphi}\right)\right], \tag{36}$$

with $a = -1/2$. A full closed-form expression covering the interplay of all relevant SOI and magnetic scattering terms in a coherent quantum mechanical description for the fitting to WAL data is still lacking, as will be discussed in the following section.

2.6.3 Quantum Interference Effects in the $\alpha = \beta$ Regime

It has been proposed already in 1995 by Pikus and Pikus that the regime of equal Rashba and the Dresselhaus strength is of special interest [101]. Their discovery was

made in the framework of quantum corrections to magnetoconductance $\Delta\sigma(B_\perp)$, studying the dependence of WAL on the two SO contributions, long before the theoretical studies discovered the spin symmetry [30, 81]. The pioneering HLN model [99] assumed only the EY-like SO mechanism. Altshuler *et al.* provided a model for die DP spin relaxation, valid in presence of either Rashba *or* linear Dresselhaus SO interaction [102]. The approach of adding a cubic (in k) term non-additively to a linear term of Iordanskii *et al.* [103] was adopted by Pikus and Pikus. They explained the magnetoconductance data by a cancellation of the Rashba and Dresselhaus terms [101], which also allowed the extraction of SO parameters from experimental data [104].

As described in Chapter 2.4.3, the two effective B-fields $\mathbf{B}_{\text{int}}^R$ and $\mathbf{B}_{\text{int}}^D$ add up to a total field, which for $\alpha = \pm\beta$ and a negligible cubic term ($\beta_3 \ll \beta$) is uniaxial. Therefore only the strength of the B-field, but not the direction of the precession axis is fluctuating and the rotation φ_n between two consecutive scattering events is proportional to the distance traveled. The total precession from (random) point A to B is even independent of the path, with the consequence, that for backscattered trajectories ($B = A$) the total rotation $\Delta\varphi = \sum_n \varphi_n = 0$ and the positive magnetoconductance signal (WAL) disappears.

To illustrate this effective spinless situation, one can look at a closed trajectory of a simple square shape, as shown in Fig. 2.13. For simplicity, the four sides of the square are aligned along the main axes $\hat{x}_+$ and $\hat{x}_-$, respectively. Electron spins with momentum $\pm\hbar k_-$ do not see an internal B-field, while electrons with momentum $\pm\hbar k_+$ precess around $\mathbf{B}_{\text{int}} \perp \hat{x}_+$. However, the sign of $\mathbf{B}_{\text{int}}$ is exactly opposite for the two relevant sections and therefore, the rotations commute and finally are undone ($\mathbf{R_3} = \mathbf{R_1}^{-1}$), with a net rotation of 0. This is true for arbitrary closed trajectories, since every path can be decomposed into segments parallel to either $\hat{x}_+$ or $\hat{x}_-$.

Because of this, the suppression of WAL is a sensitive detection of the SU(2) spin symmetry and the relative SO strengths. With an appropriate theory it is even possible to determine the SO coefficients α and β by fitting small field magnetoconductance

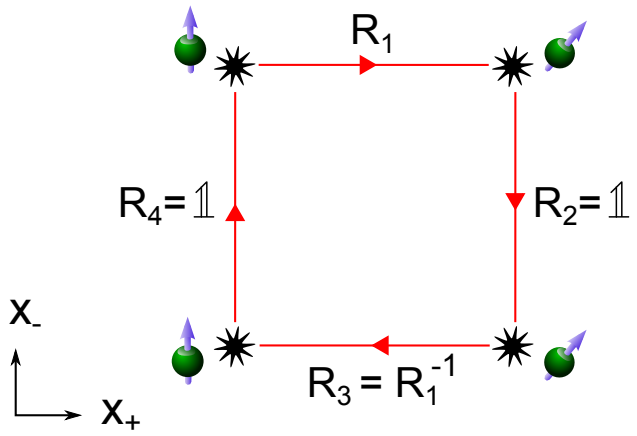

Figure 2.13: Quantum interference at $\alpha = \beta$. The total spin precession of a simple, closed trajectory is 0 for equal strength of Rashba and Dresselhaus SOI. Starting at the left top, the spin of an electron moving along $\hat{x}_+$ precesses by a rotation $\mathbf{R_1}$. No precession occurs between the following scattering event ($\mathbf{R_2} = \mathbb{1}$) and the first rotation is undone upon moving in $-\hat{x}_+$ direction ($\mathbf{R_3} = \mathbf{R_1}^{-1}$). With no precession on the last section ($\mathbf{R_4} = \mathbf{R_2}^{-1} = \mathbb{1}$), the spin returns unrotated. This is also true for the time-reversed path and coherently backscattered electrons with arbitrary path.

traces. In lack of a complete closed-form theory of MC, extraction of the SO coefficients from experimental data has proven to be difficult [91, 101, 104, 105].

3 Inverted GaAs 2D Electron Gas in Close Proximity to InAs Quantum Dots

F. Dettwiler, D. M. Zumbühl

Department of Physics, University of Basel, CH-4056 Basel, Switzerland

P. Fallahi[1], A. Badolato[1,2]

[1]*Institute of Quantum Electronics, ETH-Zurich, CH-8093 Zurich, Switzerland*

[2]*Department of Physics and Astronomy, University of Rochester, Rochester, New York 14627, USA*

D. Scholz[3], E. Reiger[3], D. Schuh[3], W. Wegscheider[3,4]

[3]*Institut für experimentelle und angewandte Physik, Universität Regensburg, 93040 Regensburg, Germany*

[4]*Laboratory for Solid State Physics, ETH-Zurich, CH-8093 Zurich, Switzerland*

Abstract

We present an inverted GaAs 2D electron gas with self-assembled InAs quantum dots in close proximity, with the goal of combining quantum transport with quantum optics experiments. We have characterized several wafers - using transport, AFM and optics - finding high-mobility, single subband 2D gases and nicely optically active self-assembled quantum dots. The dots are clearly visible on the surface with an AFM, allowing precise localization and paving the way towards a hybrid quantum system integrating optically active quantum dots with surface gate-defined nanostructures in the 2D gas.

This chapter is in preparation for publication

3.1 Introduction

A coherent spin-photon interface between quantum controlled electron spins and single photons would be desirable for fundamental as well as practical reasons, in particular in view of quantum information and communication applications. Spin qubits in gate-defined GaAs quantum dots [106] are currently among the most promising candidates for a quantum processor [15], benefiting from excellent in-situ tunability and flexibility of gate-defined nanostructures in a GaAs 2D electron gas, in particular the potential for scaling. However, due to the lack of hole confinement, these qubits do not easily couple to photons. Self-assembled quantum dots (SAQDs) e.g. made from InAs, on the other hand, are among the best solid-state photon emitters known today, acting as a spin-photon interface [22] and further allowing ultrafast optical manipulation [107, 108].

Placing a SAQD in close proximity to a surface-gate defined double dot can create a hybrid quantum system [25], opening the door for coherently converting the stationary spin qubit to a photon, and vice-versa, thus enjoying the advantages of both systems in a combination of quantum optics and quantum transport experiments. Growing InAs SAQDs in vicinity of a 2DEG (Fig. 3.1) causes electron scattering [109–112] and allows investigation of charging of nearby SAQD ensembles by C-V spectroscopy [113, 114] or with transport measurements [115, 116]. Transport experiments on a small number or single dots have been done on structures with 2DEG [117–119] and without 2DEG using nanogap electrodes [120–123].

In this Chapter, we present quantum transport, atomic force microscope (AFM) and optical measurements characterizing several wafers with tunnel barriers between the 2DEG and the InAs dots ranging from 15 nm to 60 nm. The mobility of the 2DEG depends on the tunnel barrier thickness, displaying higher mobilities for the larger barriers thicknesses. Shubnikov-de Haas oscillations indicate a single-subband 2DEG, with a depth - as extracted from top gate capacitance measurements - consistent with the expected depth. Micro-photoluminescence (μ-PL) measurements on individual

InAs dots show nicely optically active quantum dots with typical, narrow line widths. Further, the deformation field of the quantum dots is clearly visible on the surface with an AFM, even though the dots are buried about 500 nm below the surface. This allows precise localization of individual quantum dots, paving the way towards hybrid systems integrating single quantum dots in surface gate defined nanostructures in the 2DEG.

3.2 Inverted Hybrid 2DEG Structure

Figure 3.1 shows the growth profile of the hybrid samples investigated. All samples were grown on semi-insulating (100) GaAs substrates by molecular beam epitaxy (MBE). The inverted 2DEG is located 500 nm below the surface, with the Si delta doping layer set back 50 nm below the 2DEG. An InAs wetting layer followed by Stranski-Krastanov InAs QDs are separated by a tunnel barrier of width $x = 15, 30, 45$ and 60 nm. An inverted 2DEG structure was chosen because of two reasons. First, the strain field of the InAs SAQDs is expected to have a smaller effect on the mobility μ. Additionally, the alignment of the discrete energy levels of the SAQDs with the Fermi energy should require a relatively small external potential. This requirement can be fulfilled with the described structure as can be seen in the self-consistent conduction band simulation [124], also shown in Figure 3.1. Although inverted 2DEGs are expected to have a lower mobility than comparable non-inverted structures due to Si migration from the doping layer, high mobility heterostructures with values up to $3 \cdot 10^6\,\mathrm{cm}^2/(\mathrm{Vs})$ have been grown [125].

3.3 InAs SAQD Density Gradient

2DEG characteristics were measured on a Hall bar setup (Fig. 3.2a), fabricated with standard photolithographic methods. 4-wire ac measurements were done at 4.2 K and for some samples also in a dilution refrigerator (DR) at 20 mK. Electron density n and

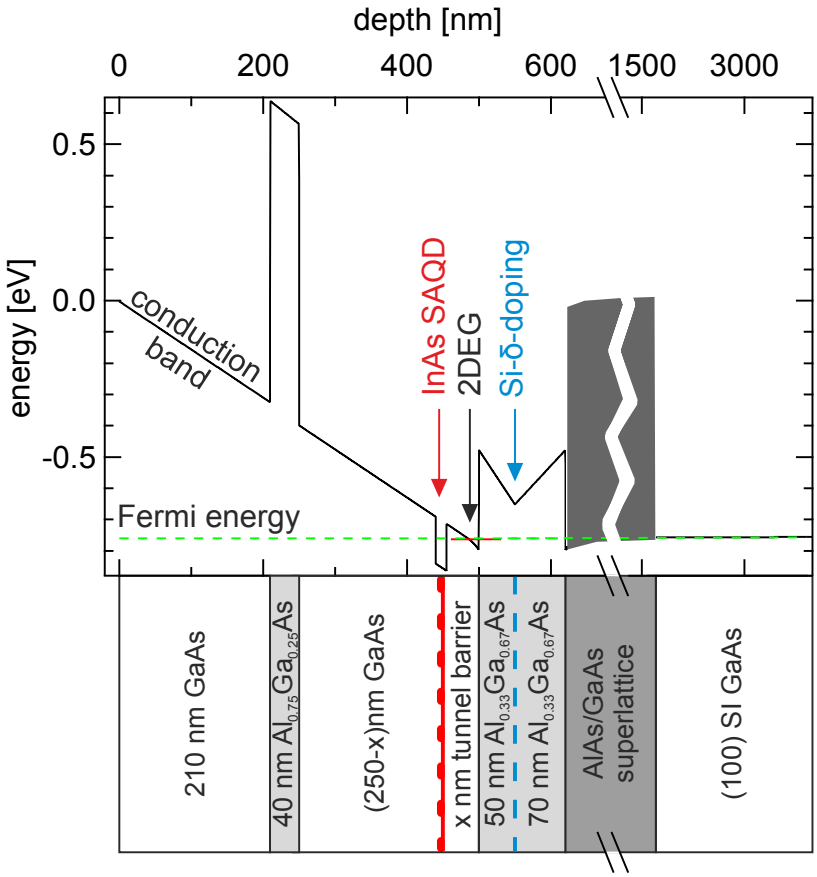

Figure 3.1: Growth profile and corresponding conduction band energy of the hybrid wafer. Tunnel barrier width x between InAs SAQDs and inverted 2DEG is varied between 15 and 60 nm. Electrons are allowed to tunnel from the 2DEG (red line indicates first subband) and the SAQD. By applying a top gate voltage, the QD energy levels (not shown) can be aligned with Fermi energy E_F. Conduction band is calculated self-consistently [124].

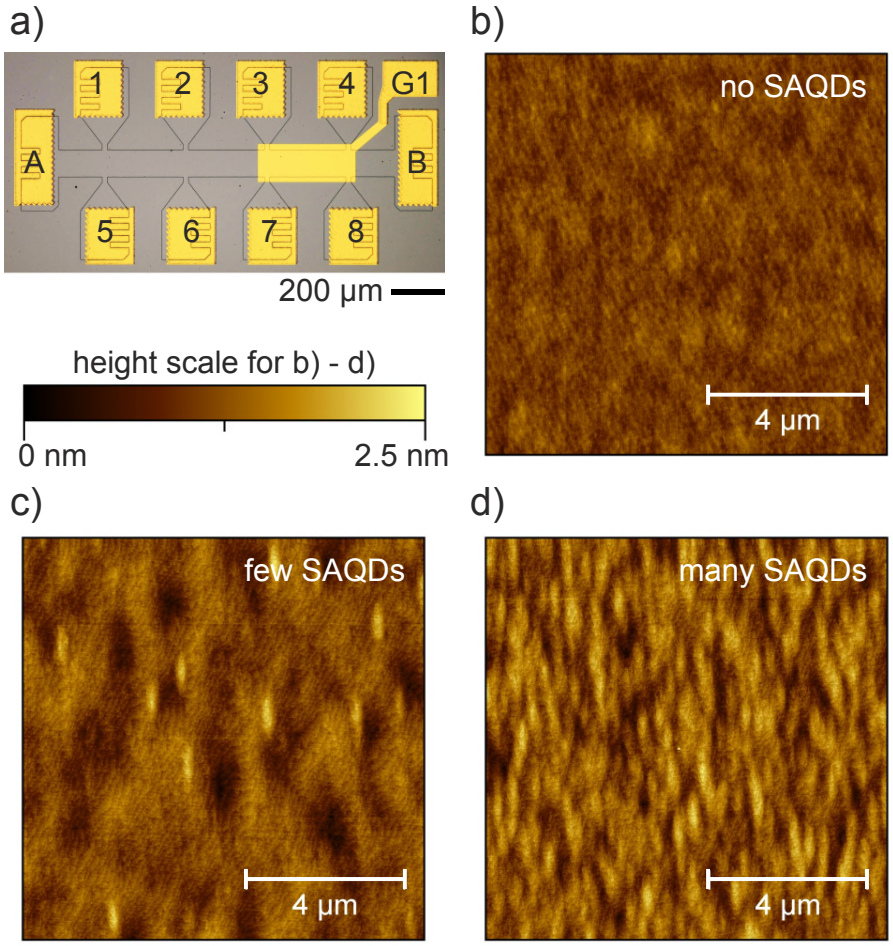

Figure 3.2: Sample design and AFM measurements. **(a)** Optical image of a test chip. The same Hall bar design is used in the experiments. **(b)-(d)** AFM images of the wafer surface: area with **(b)** no, **(c)** few and **(d)** many SAQDs.

mobility μ were investigated for samples with and without SAQDs. Successful InAs SAQD formation is confirmed by μ-PL and AFM measurements. The latter method was also used to determine the InAs SAQD density. The deformation field of the InAs islands propagates through the crystal, therefore single dots are still detectable by AFM on top of the wafer, even under a capping layer of almost 500 nm. The cigar-shaped hills on the surface (see Fig. 3.2c) are much larger ($\sim$ 800 nm long and $\sim$ 250 nm wide) than the actual QD dimension ($\sim$ 30 nm). The small height of the surface structure of $\sim$ 1 nm makes it difficult to detect these hills.

During QD growth the wafer was not rotated, resulting in a density gradient along one wafer axis. Figures 3.2b – d show three examples of different SAQD density. While

areas like Fig. 3.2c are of interest for single QD experiments mentioned in the introduction paragraph, samples like Fig. 3.2b (no SAQDs, only wetting layer) and 3.2d (high SAQD density and wetting layer) were used in this experiment to compare the influence of the SAQDs. RMS roughness values also reflect the obvious difference in SAQD density, with $R_{\mathrm{RMS\,no\,QDs}} = 0.15\,\mathrm{nm}$ (Fig. 3.2b), $R_{\mathrm{RMS\,few\,QDs}} = 0.27\,\mathrm{nm}$ (Fig. 3.2c) and $R_{\mathrm{RMS\,many\,QDs}} = 0.32\,\mathrm{nm}$ (Fig. 3.2d). Note that due to the overlap of the surface hills, the exact SAQD density cannot be determined with this method.

3.4 Interaction between 2DEG and InAs SAQDs

3.4.1 Effect on the 2DEG Mobility

For all the devices, density and mobility were extracted from the slope of the Hall trace of the transversal resistance $R_{XY}(B_\perp)$ in the classical regime and the zero field longitudinal resistance $R_{XX}(B_\perp = 0)$, measured at 4 K. Due to the constant set back of the Si donors, the density n is of comparable magnitude throughout the different wafers, with values between 0.9 and $1.5 \cdot 10^{11}\,\mathrm{cm}^{-2}$. The distance to the wetting layer/SAQDs does not have an influence on n, but mobility is highly affected by a nearby InAs layer (present in all samples). A drastic reduction of μ is observed for small barrier widths x, when the InAs wetting layer is close the the 2DEG, as shown Figure 3.3. In the two panels, we compare the influence of SAQDs, using two growth procedures, in which the temperature during the deposition of InAs was varied. The pyrometer temperature of the data shown in the upper (lower) panel was at $T \approx 517\,^\circ\mathrm{C}$ ($T \approx 534\,^\circ\mathrm{C}$) during the growth of the SAQDs. For each data point, at least two different Hall bars were measured.

The mobility reduction from the InAs wetting layer is increased significantly in presence of SAQDs. The potential of the SAQDs causes additional scattering and hence a decrease in the mobility is observed on the samples with high QD density. We found the effect to be largest for the wafer with barrier width $x = 30\,\mathrm{nm}$ (Fig. 3.3, upper panel).

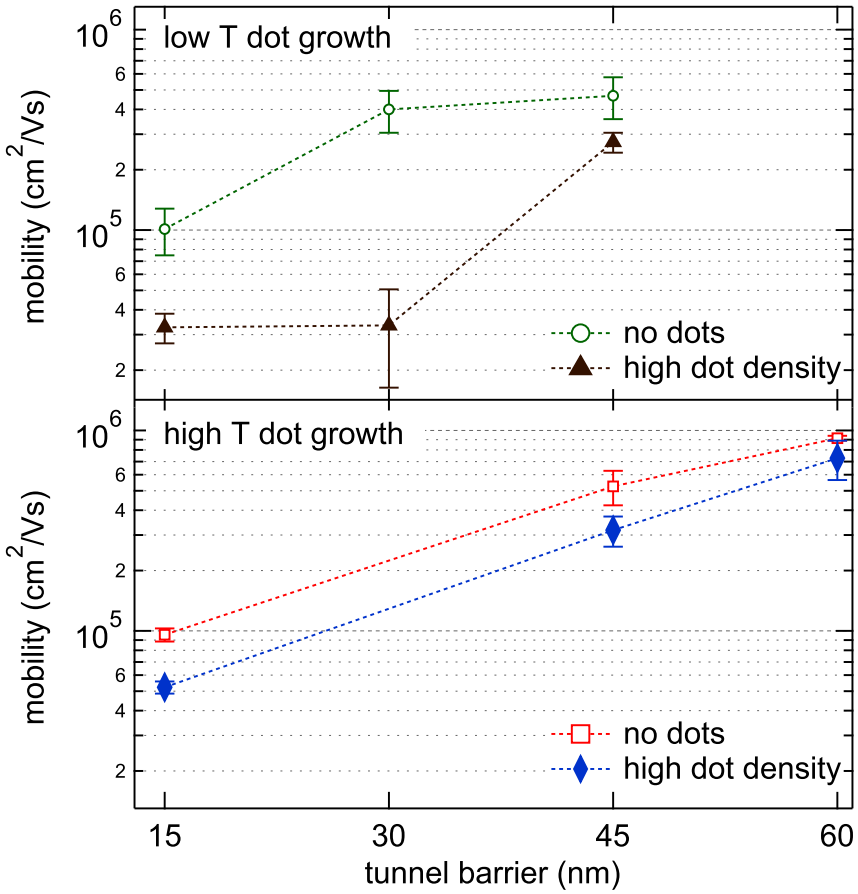

Figure 3.3: Electron mobility as functions of tunnel barrier width for two different growth temperature profiles. The pyrometer temperature during InAs deposition was $T \approx 517\,^{\circ}\mathrm{C}$ for the wafers in the upper panel and $T \approx 534\,^{\circ}\mathrm{C}$ for the samples shown in the lower panel. For each wafer, we compare devices without SAQDs (empty markers) to high SAQD density devices (solid markers). A small tunnel barrier width x reduces the mobility significantly, even in absence of SAQDs (only wetting layer). Scattering decreases for increased tunnel barrier width. SAQDs lead to an additional reduction of mobility. The temperature during SAQD growth affects the quality of the 2DEG only weakly. Lines are guide to the eye.

Here, the relative difference in μ between the samples with and without SAQDs is more than one order of magnitude. The mobility reduction gets smaller for increased tunnel barrier widths, with $\mu > 0.5 \cdot 10^6 \mathrm{cm}^2/(\mathrm{Vs})$ and a relative difference of less than 30% for the 60 nm tunnel barrier wafer (Fig. 3.3, lower panel). This result is in qualitative agreement with previous work on similar inverted hybrid 2DEGs [109], but the mobility of our material is significantly higher. Further, the wave function extension into the SAQD layer for small x, leading to an increase in n, is omitted in our wafers. Thus, the high degree on the control of the growth parameters allows us to achieve a considerable improvement in quality of the hybrid material.

From a higher temperature during InAs growth, one would expect two effects: (i) SAQD nucleation probability is reduced, resulting in the growth of larger but less QDs (lower QD density) [126, 127]. (ii) The required lowering of the temperature for the SAQD growth possibly affects the quality of the GaAs capping layer in a negative way (more point defects). Increasing the InAs growth temperature by $\sim 20\,^\circ\mathrm{C}$ might therefore result in an improved μ. Comparing the absolute mobility values and the relative difference (no dots/high dot density) in the two panels of Figure 3.3, we have no evidence for a significant overall improvement, but data indicates, that for small tunnel barrier x, the negative effect of the SAQDs seems to be weakly suppressed due to a different SAQD morphology. Note, that we could not verify changes in size and density of the SAQDs with the AFM. Further, the capping layer alone also plays an important role: A test wafer grown at the same temperature profile, but without actually depositing InAs also results in a mobility reduction [128, 129].

3.4.2 Subband Occupation and Depth of the Inverted 2DEG

Additional measurements at 20 mK were done to exclude parallel 2D transport channels like an occupied second subband or other 2DEGs. Indeed the minimum in the longitudinal resistance R_{XX} go to zero at the Hall plateaus (Fig. 3.4, blue curve) and the Fourier transform of the Shubnikov-de-Haas oscillations results in one single peak

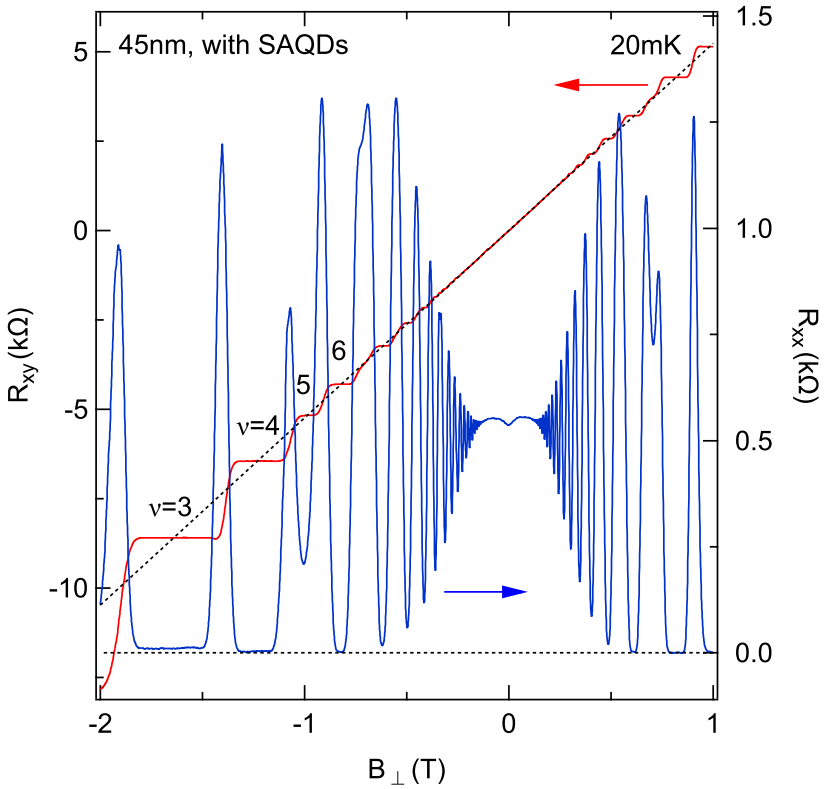

Figure 3.4: Quantum Hall effect and Shubnikov-de Haas oscillations. Transversal (red, left axis) and longitudinal (blue, right axis) resistance as a function of the applied perpendicular magnetic field $B_\perp$. Density extracted from Hall slope (black dashed line) and Shubnikov-de Haas oscillation frequency are in agreement. The minimum in R_{XX} go to zero for high $B_\perp$ and no beating pattern is visible, therefore parallel conduction channels are excluded.

(for fields below Zeeman splitting). Transversal resistance R_{XY} (Fig. 3.4, red curve) shows linear behavior (black dotted line) and plateaus can be assigned to integer filling factors ν. Electron densities calculated from Shubnikov-de-Haas oscillations agree with the values taken from Hall slope measurements, also indicating the absence of parallel conduction channels.

The pronounced negative magnetoresistance around zero field has been observed in 2D hole gases (2DHGs) [130] and in 2DEGs in presence of a periodic potential [131–133] or magnetic impurities [134]. For the $x = 45\,\text{nm}$ wafer, this minimum is measured only on the high SAQD density sample. There is now evidence for a strict periodicity of the background potential from the SAQDs, but nevertheless this could be a possible explanation for the magnetoresistance minimum.

The 2DEG depth was measured using the top gate (G1 in Fig. 3.2a). Density and mobility of all devices showed linear dependence on gate voltage, as shown in Fig. 3.5. Approximated by the parallel plate capacitor model, the 2DEG and the top gate are the two plates of area A, separated by distance d. The capacitance C per area is

$$\frac{C}{A} = \frac{\epsilon\epsilon_0}{d} = e\frac{\delta n}{\delta V_\mathrm{g}}, \tag{37}$$

where e is the elemental charge and ϵ_0 is the permittivity. From the slope of a linear fit of the density as a function of gate voltage $\delta n/\delta V_\mathrm{g}$ (Fig. 3.5) and $\epsilon \approx 12$ for GaAs we get $d \approx 500\,\mathrm{nm}$, in good agreement with the growth profiles. Quantum capacitance of the 2DEG and capacitance of the measurement setup, which add in series [113] can be neglected, because they are much larger.

The range of usable top gate voltage V_g is limited by the inception of leakage currents $> 1\,\mathrm{nA}$ and differs between the devices due to varying mesa etch depths. A smaller etch depth results in a reduced gate voltage range. Note that for our devices, we chose etch depths ranging between $290 - 460\,\mathrm{nm}$ (see Appendix A), well above the heterointerface and the δ-doping depth. Ohmic contacts experienced adhesion problems, when the mesa was etched into the AlGaAs layer due to Al oxidation. Top gate and 2DEG were also used for C-V spectroscopy. However, charging of QD orbitals could not be observed with this method.

3.5 Summary

In summary, we have successfully grown and characterized inverted 2DEG structures with InAs SAQDs in close proximity. The wafers are grown with a density gradient of optically active SAQDs, verified with AFM measurements on the wafer surface. Wetting layer growth and QDs limit the mobility inside the quantum well. The limiting effect decreases with increasing tunnel barrier width between 2DEG and wetting layer. The mobility is further decreased by SAQDs. Despite this reduction effect, the inverted

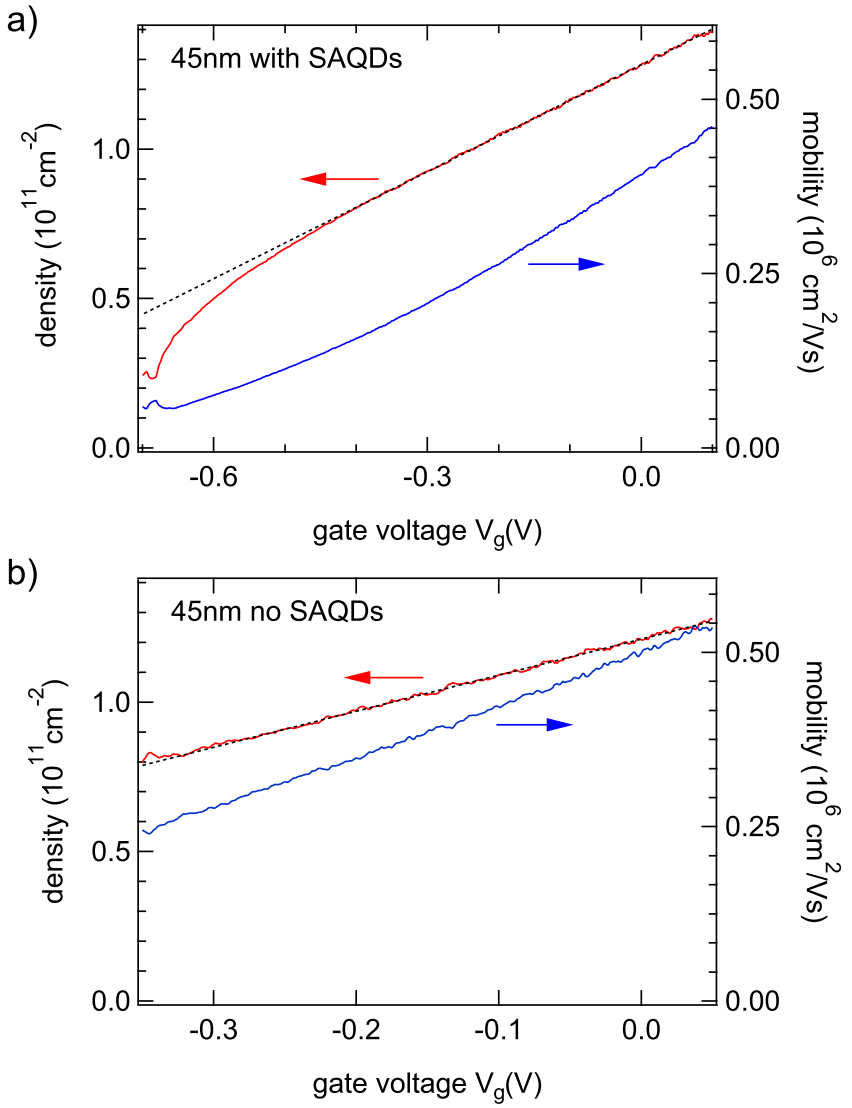

Figure 3.5: Density and mobility of the 45 nm tunnel barrier devices **(a)** in presence and **(b)** in absence of SAQDs as a function of top gate voltage V_g. From the linear fit (black dashed line), the 2DEG depth is calculated.

hybrid 2DEGs exhibit mobilities exceeding $0.5 \cdot 10^6 \mathrm{cm}^2/(\mathrm{Vs})$, while tunneling from 2DEG to the SAQDs should still be possible. Such high quality hybrid structures in principle are also suitable for ballistic transport experiments.

4 Quantum Point Contact Devices Containing Single InAs Self-Assembled Quantum Dots

F. Dettwiler, D. M. Zumbühl

Department of Physics, University of Basel, CH-4056 Basel, Switzerland

P. Fallahi[1], A. Badolato[1,2]

[1]*Institute of Quantum Electronics, ETH-Zurich, CH-8093 Zurich, Switzerland*

[2]*Department of Physics and Astronomy, University of Rochester, Rochester, New York 14627, USA*

D. Schuh[3], W. Wegscheider[3,4]

[3]*Institut für experimentelle und angewandte Physik, Universität Regensburg, 93040 Regensburg, Germany*

[4]*Laboratory for Solid State Physics, ETH-Zurich, CH-8093 Zurich, Switzerland*

Abstract

In this chapter, we discuss the fabrication and measurements of quantum point contact (QPC) devices on inverted 2DEG material. The top-down fabrication approach of placing split gate electrodes near a single self-assembled InAs quantum dot requires an ultra-clean wafer surface. An additional third gate above the SAQD is used to independently tune the charge state. The QPC conductance is dominated by the disorder potential of the 2DEG and does not show conductance quantization. No signature of discrete energy levels of a single quantum dot was observed in the QPC conductance.

4.1 Fabrication of Hybrid Devices

The most common way to grow InAs QDs is by self-assembly [35]. For the majority of optical experiments, the QD position is not an important parameter, since experiments involve QD ensembles and do not require an exact alignment of metal electrodes. Considering the coupling of single QDs to lateral structures [25], alignment and spatial control becomes a fundamental necessity. One possible approach to this problem is the site-controlled growth by using a pre-structured substrate [135, 136].

Here, we use a top-down approach on as-grown self-assembled QDs. To successfully couple lateral 2DEG nanostructures and InAs SAQDs on a hybrid device, the exact positioning of gate electrodes precisely at a single (specifically chosen) SAQD is a necessary and challenging prerequisite. Optically addressable QDs are usually buried under a capping layer, some tens of nanometers below the surface. The growth conditions and material composition of the capping layer affects not only the PL spectrum, but also the surface morphology, with elongated, cigar-like structures found for fast GaAs cap layer growth [137]. As already shown in Figure 3.2, these small elevations are detectable with an AFM, allowing for precise localization and alignment of lithographically defined lateral gate structures.

4.1.1 High Precision QD Localization

Alignment Grid: The material used for the QPC charge sensing experiment and the C-V spectroscopy control experiment is the same inverted 2DEG hybrid structure as described in Chapter 3.2, with a tunnel barrier width of $x = 45\,\text{nm}$ between the SAQDs and the 500 nm deep 2DEG. AFM mapping on the clean wafer surface is used to determine the SAQD density as a function of position. For single dot experiments a region of intermediate density with distances $> 1\mu m$ between the QDs is chosen (Fig. 3.2c).

For the devices, we use a Hall bar design with four alignment grids of 6×4 markers,

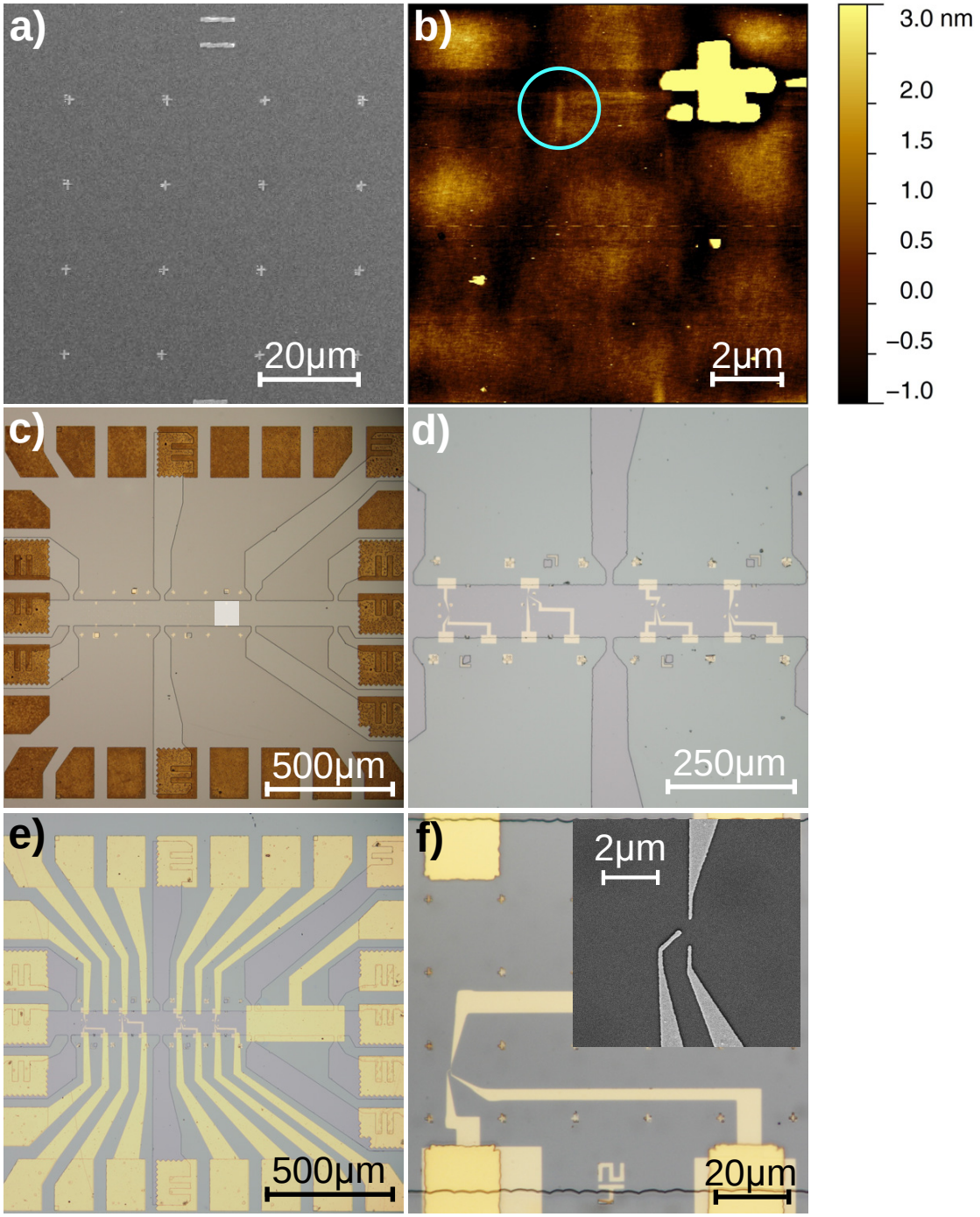

Figure 4.1: Sample fabrication steps. **(a)** The localization and alignment grid (SEM image) is the first fabrication step. **(b)** The grid area is mapped by AFM to determine the precise location of InAs SAQDs (elongated shape in blue circle) with respect to the grid markers (upper right). **(c)** Optical image of the mesa etch and Ohmic contacts of the Hall bar design added after the AFM mapping, using UV lithography. Four individual grids (gray square indicates one grid, as shown in **a**) are placed on one Hall bar device. **(d)** One QPC device with 3 gates each was added per grid (see also **f**). Exact alignment is achieved using e-beam lithography. **(e)** Photogates connect the QPC gates with the bonding pads. On the rightmost segment of the Hall bar a larger top gate is added, used for C-V spectroscopy. **(f)** Detail of one of the QPC devices. Inset: SEM micrograph showing the two split gates and a third top gate to tune the potential of the SAQD (below the gate).

separated by 20 μm (see Fig. 4.1a). These are lithographically defined and evaporated onto the surface of the chosen the wafer piece. To maintain an ultra-clean surface in this first electron beam lithography step, we use *ZEP 520A*, an anisole based e-beam resist. A special treatment with UV-flood exposure before the deposition of 5/20 nm of Ti/Au supports the lift-off process and enhances the removal of resist residues, allowing subsequent AFM mapping measurements without significant resist residues left on the surface. The exact fabrication parameters can be found in Appendix C.1.

AFM Mapping: All grid quadrants are scanned for signatures of buried InAs SAQDs with an AFM. In Figure 4.1b the AFM height image of such an elongated overgrowth island (blue circle) is shown. An exact coordinate assignment of the center of the SAQD surface structure relative to the position of the alignment marker crosses (upper right in Fig. 4.1b) allows a later alignment of lithographically defined nanostructures. The accuracy of the assignment is limited by drifts of the AFM and the only weakly defined shape and small height of the SAQD island. To increase the precision, the position of the SAQD is measured using all four markers per quadrant. Each image is recorded at least twice. We estimate the total error of this procedure to be $\approx \pm 200$ nm. A final verification with AFM (PMMA residues) or SEM (QDs not visible) is not possible. Given the width of the QPC channel ($\sim$ 1-1.2 μm), the QD gate ($\sim$ 100-200 nm) and the diameter of the QD ($\sim$ 25 nm), the QD has to be near the QPC channel and its charge state should be affected by the QD gate.

Hall Bar and Ohmic Contacts: By etching a mesa, the Hall bar structure is defined (Fig. 4.1c), using UV lithography. The Hall bar is aligned optically to the four marker grids. The 2DEG is contacted via thermally annealed AuGe/Pt Ohmic contacts, also fabricated using UV-lithography and a rapid thermal annealer.

QPC Gate Electrodes: In an additional e-beam step, small Ti/Au QPC gates are defined, exactly aligned to the SAQD via the marker grid (Figures 4.1d&f), using the

coordinates determined by AFM mapping. A total of four QPC devices (three gates each) with slight variations in design and width are fabricated on each Hall bar. One example of a QPC is shown in the inset of Fig. 4.1f: the two split gates are separated by $\sim 1\,\mu$m. The tip of the third (middle) gate coming from the lower left is placed to lie exactly on top of the SAQD, enabling independent control of the charge state in the QD.

Gate Connections: To complete the sample, photogates (Ti/Au) connect the inner QPC gates with the larger bonding pads at the border of the sample, as shown in Fig. 4.1e. The device is then glued and bonded to a chip carrier.

4.2 QPC Charge Sensing Device and Measurements

4.2.1 QPC Device

Following the idea of Field *et al.* [56], a QPC is a sensitive sensor for nearby changes in the electrostatic environment and thus an ideal charge sensor. Our charge sensing experiments were done on different QPC designs, using a 2-wire and 4-wire voltage bias setup to measure the conductance, as displayed in Figure 4.2. The QPC channel is formed by applying negative voltages V_1 and V_2 on the two split gates. The lithographically defined spacings W were chosen to be either $1\,\mu$m or $1.2\,\mu$m and gate dimension $L = 100\,$nm. Voltage V_3 is used to tune the charge state of the SAQD and locally change the 2DEG density. In design A (Fig. 4.2a) the gates are placed such that the SAQD is at some distance $D = 500\,$nm to the QPC, whereas in design B (Fig. 4.2b) it is directly above the channel. Note that in both cases the SAQDs are in a layer 45 nm away from the inverted 2DEG and couple only electrostatically to the QPC. If the 2DEG is also depleted below the third gate (at $V_3 \approx -800\,$mV), a more narrow QPC forms between the lower gate and the dot gate.

The 2DEG density $n = 1.25 \cdot 10^{11}\,\mathrm{cm}^{-2}$ and mobility $\mu = 600'000\,\mathrm{cm}^2/(\mathrm{Vs})$ correspond

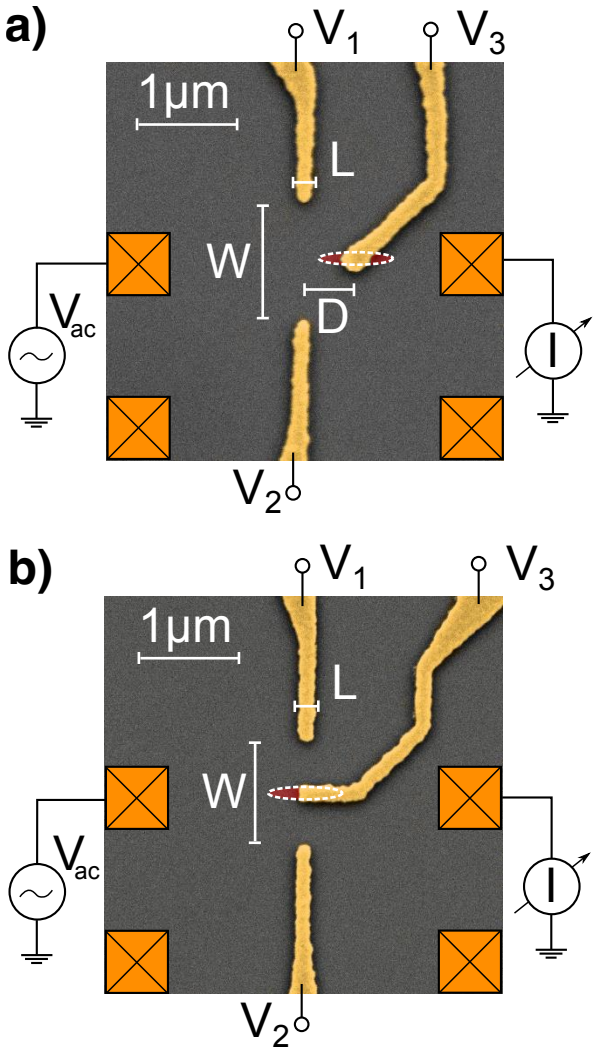

Figure 4.2: QPC device designs. **(a)** Design A (SEM image, false colors) with split gates (V_1, V_2) and third dot gate (V_3). The third gate is aligned to be centered on the SAQD surface structure, as indicated (dotted white/red ellipse). Note, that here we display the ideal case. The SAQD is not visible in the SEM. AC voltage bias is applied and current is measured using two Ohmic contacts (yellow squares). Alternatively, a 4-probe current bias measurement can be used to determine the QPC conductance. **(b)** In design B, the SAQD/third gate is in the center of the QPC.

to a mean free path of $l_p \approx 3.5\,\mu$m and a Fermi wavelength of $\lambda_F = 70\,$nm. From PL measurements, optically active electron hole recombinations are expected at top gate voltages between 0 and +500 mV (see Appendix B).

4.2.2 Channel Formation

A 1-dimensional constriction is formed, while sweeping the voltages V_1 and V_2 of the two QPC gates simultaneously to negative values. The conductance g as a function of gate voltage ($V_1 = V_2$) is shown for both QPC designs in Fig. 4.3a&b, left panel. The ~ 30 modes available after 2DEG depletion below the gates ($V_{1,2} \sim -1\,$V) correspond to a channel width of $30 \cdot \lambda_F/2 = 1.1\,\mu$m, consistent with the width W of the lithography. Stable conductance quantization steps in units of $2e^2/h$ cannot be assigned (see also inset of Fig. 4.3b) and the material exhibits a relatively large hysteresis between down and up sweep traces. However, the small features in the conductance traces are reproducible (Fig. 4.3b, dotted line in inset of left panel). The gate leakage current was tested and is smaller than 1 nA over the whole range in Fig. 4.3.

Moreover, no quantization steps are observed for a QPC formed between the lower gate and the quantum dot gate (Fig. 4.3a&b, right panels). In this configuration, the 1D channel is smaller for both designs (design A: $\sim 650\,$nm, design B: $\sim 450\,$nm) and hence the QPC pinch-off is expected to happen at less negative voltage. Compared to the pinch-off curves of the split gates, a clear kink in the conductance (indicating 2DEG depletion) is not observed and the number of modes cannot be determined. However, we clearly have conduction after depletion and hence a channel has formed.

A possible explanation for the absence of the conductance quantization steps is the potential landscape in the QPC. Potential variations in the channel on the scale of the Fermi wavelength $\lambda_F \sim 70\,\mu$m cause scattering. Such variations are usually not found in the confinement potential itself, but come from long range fluctuations and from randomly distributed charged donors or impurities and lead to the breakdown of the conductance quantization [138]. In the inverted hybrid structure, SAQDs and

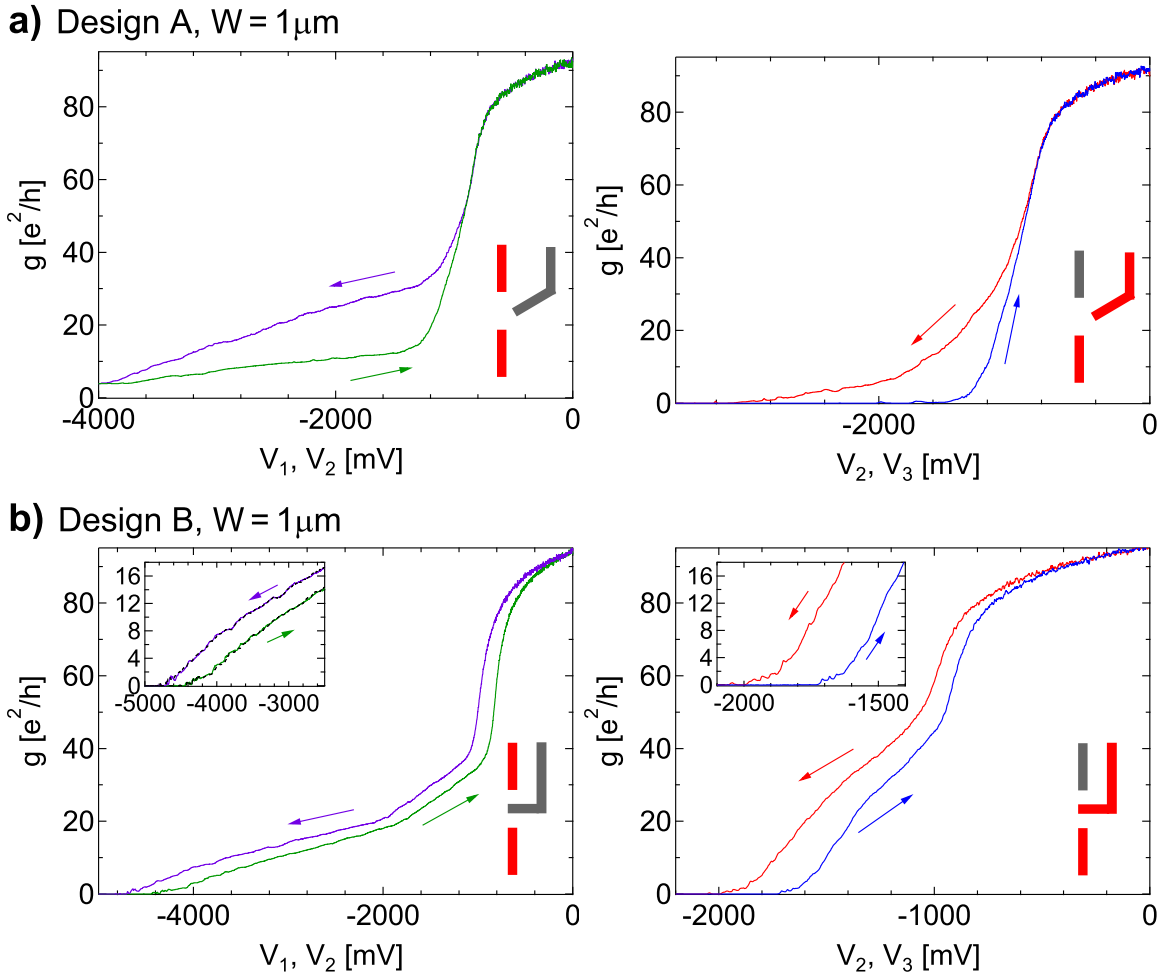

Figure 4.3: QPC channel formation. **(a)** Conductance of a QPC of design A and width $W = 1\,\mu$m as a function of split gate voltage V_1, V_2 (left) and V_2, V_3 (right), being swept simultaneously. Around $V_{1,2} = -800\,$mV the 2DEG is depleted and the current only passes through the modes of the QPC. The conductance shows no clear quantization and there is a hysteresis between up (green, blue) and down (purple, red) traces (as indicated by arrows). The QPC forming between the lower gate and the dot gate (right) closes at less negative voltages, compared to the split gate (left). **(b)** Design B QPC channel formation as a function of split gates (V_1 and V_2, left) and quantum dot gate (V_2 and V_3, right). The hysteresis is less pronounced and small features are more reproducible (left inset, dashed lines show 2nd trace), but also no clear quantization steps form (see insets for zoom-in).

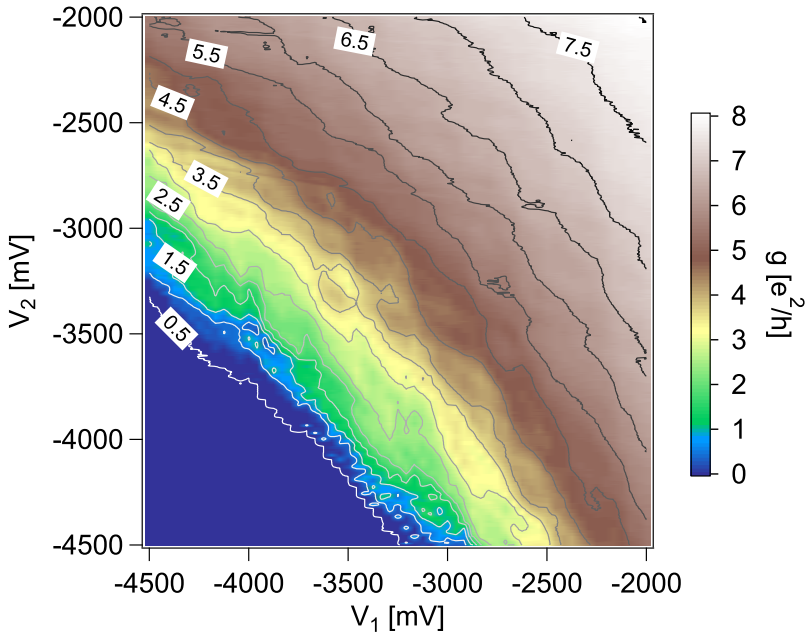

Figure 4.4: Lateral shift of the QPC. False color plot of the QPC conductance g (design A, 1 μm) as a function of the two gates (V_1 and V_2). Contour plot lines indicate constant conductance (see label for value). To move on a contour line, a more negative voltage V_1 must be compensated by a less negative voltage V_2. Lines of constant conductance are not well defined and quantization is not visible for any configuration of gate voltage.

the migration of Si donor atoms [125] are possible sources. It was shown theoretically, that the induced small angle backscattering is suppressed in a 1D channel, except for the highest newly populated mode [139]. There, backscattering requires only a small momentum transfer and therefore the transmission probability $T < 1$, resulting in mesoscopic fluctuations in the conductance Δ_G in the order of e^2/h. Depending on the QPC geometry (mainly on channel length L_C) and 2DEG characteristics, these fluctuations destroy the quantization completely, down to the lowest subband, even if the condition for ballistic transport $l_p > L_C$ holds. Further, the 2DEG depth of 500 nm and the relatively large channel width W might result in a flat (confinement) potential landscape around the minimum and hence in a small energy separation between the subbands.

4.2.3 Probing the Disorder Potential

By applying different gate voltages on the two split gates, the potential minimum is shifted laterally [140, 141] and we can probe the local (impurity) potential using the QPC conductance. In Figure 4.4 a 2D scan of the conductance through the QPC as a function of the two split gate voltages V_1 and V_2 is shown. By going to more negative gate voltage on one gate (e.g. V_1) the conductance can be kept constant, if V_2 is increased. For a perfect 1D channel, the resulting lines of constant conductance are hyperbolic in the gate voltage space. In our experiment we observe unstable lines indicating a hyperbolic shape only weakly. The 2D scan of the conductance shows no signature of quantization (roughly linear in gate voltage) but only small (reproducible) fluctuations, thus probing the potential disorder of the inverted 2DEG inside the channel.

4.2.4 Dot Gate Influence

Even in absence of clear and stable quantization steps, the QPC conductance can be a sensitive detector for nearby changes in the charge. However, the signature of a possible change of the charge state in the nearby InAs SAQD is difficult to distinguish from local potential fluctuations. Features coming from SAQD charging/de-charging events should however depend strongly on the voltage of the third gate V_3 right above the QD.

To find such features, the lateral shifting of the QPC was repeated for different voltages V_3 applied to the QD gate. Two situations are shown in Fig. 4.5a ($V_3 = -1200\,\mathrm{mV}$) and 4.5b ($V_3 = -1750\,\mathrm{mV}$). On top of the weak background pattern of nearly parallel vertical and horizontal lines (indicated by dashed red lines in Fig. 4.5a) stronger lines appear (black arrow). These are only weakly depending on V_1 and the QD dot gate voltage V_3, appearing at almost the same position in Fig. 4.5b and are not affected by the occasional switching events (Fig. 4.5b, white arrows), observed for $V_3 \leq -1400\,\mathrm{mV}$.

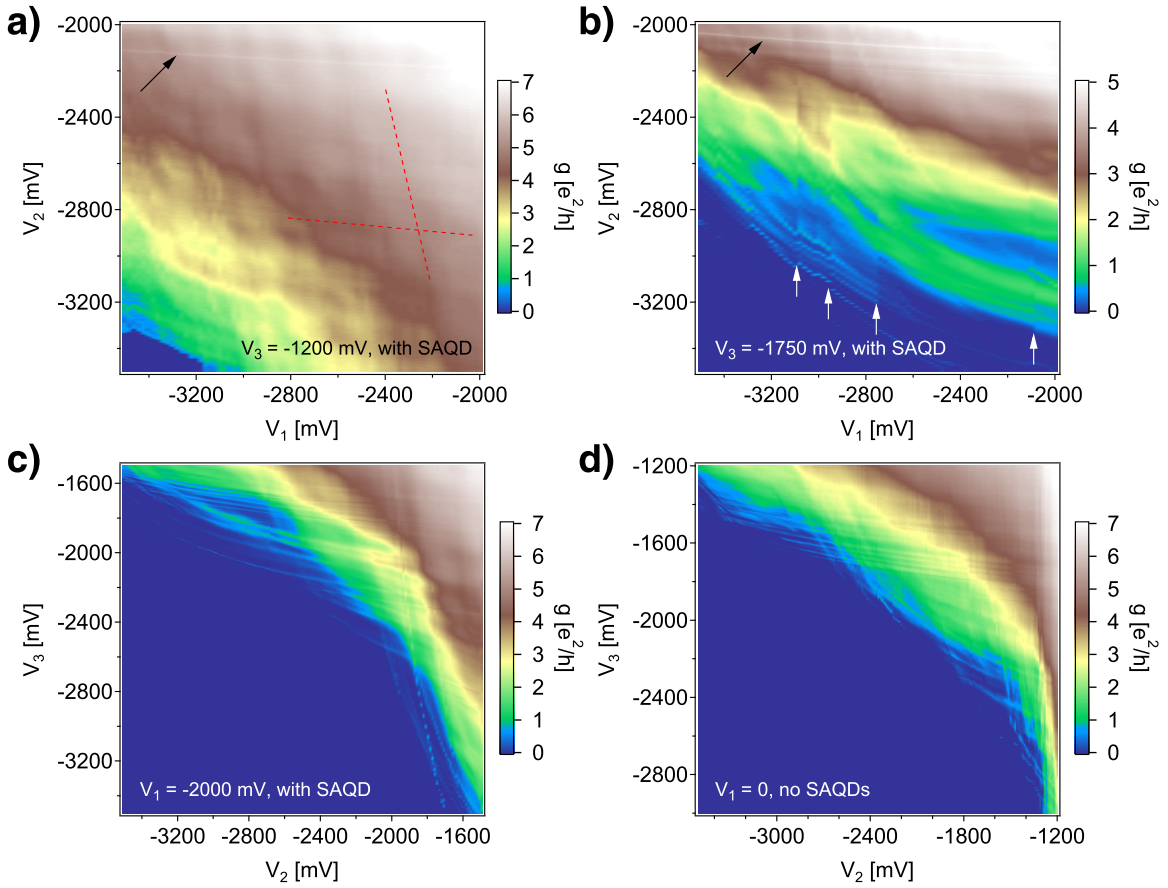

Figure 4.5: Influence of the QD gate and reference data. **(a)** QPC conductance g as a function of V_1 and V_2 with local variation of the density, using the third (QD) gate ($V_3 = -1200\,\mathrm{mV}$). Lines of slightly increased conductance are visible around $V_2 \sim -1200\,\mathrm{mV}$ (black arrow). A weak pattern of parallel stripes is identifiable in the 2D plot, as indicated by the red dashed lines. **(b)** For $V_3 = -1750\,\mathrm{mV}$, the QPC pinch-off voltage is shifted to less negative values in V_1 and V_2. More lines appear, but the position is only weakly affected by V_3 (black arrow). Resonant features appear near $g = 0$. White arrows indicate jumps. **(c)** Conductance measurement for the lateral shift of the (smaller) QPC between lower split gate and QD gate ($V_1 = -2000\,\mathrm{mV}$). Large number of resonance lines visible. **(d)** Very similar conductance features are measured on a reference QPC (same geometry, no SAQDs detected with AFM). Here $V_2 = 0$ (upper QPC gate). All data taken in absence of a magnetic field $B = 0$.

The switching events have the signature of a random, slow two-level fluctuation, induced by a nearby charge charging/de-charging. The absence of a reproducible gate dependence excludes the SAQD to be the source. Despite the lack of quantization steps, the background pattern shows similarities to QPC conductance pattern containing a scattering center of diameter $d \gg \lambda_F$, thus forming two coupled channels around the impurity [142, 143].

Overall, the QPC pinch-off voltage of the split gates is shifted to less negative voltages while decreasing V_3, explained by a local decrease of the charge carrier density below and around the QD gate. In the pinch-off regime near $g = 0$, a number of resonance lines appears, which is a further indication for scattering inside the QPC channel [142].

Similar resonance curves are also measured when shifting the smaller constriction, formed between the lower QPC gate and the QD gate (see Fig. 4.5c). Groups of parallel curves show different gate dependences with two main slopes. In Figure 4.5c we show the measurement result of a QPC of the same dimensions, but fabricated on a Hall bar lacking SAQDs (only WeL, measured with AFM). The presence of these resonances and an overall similar conductance pattern in this reference sample excludes the InAs SAQD to be the origin of the disorder and indicates the remote potential and possible migration of the Si dopants to be the main source.

4.3 C-V Spectroscopy Control Experiment

As a second transport charge detection experiment C-V spectroscopy data was taken, using the large ($100 \times 300\,\mu$m) top gate (see Fig. 4.1e) and the 2DEG as a back contact. Note that with this method, all the QDs in the gated area are measured. The applied dc voltage V_{CV} is swept and modulated with a small ac voltage V_{rms} with frequency f and a current $I_{\mathrm{CV}} \propto C$ is measured with the lock-in. In Fig. 4.6 a measurement with $f = 1.012\,$kHz and $V_{rms} = 2.23\,$mV is shown. The C-V curves typically drop between $-200\,\mathrm{mV} < V_{\mathrm{CV}} < 200\,\mathrm{mV}$ but do not show the characteristic charging features of single orbitals as reported in Refs. [41, 49, 144]. The step-like small

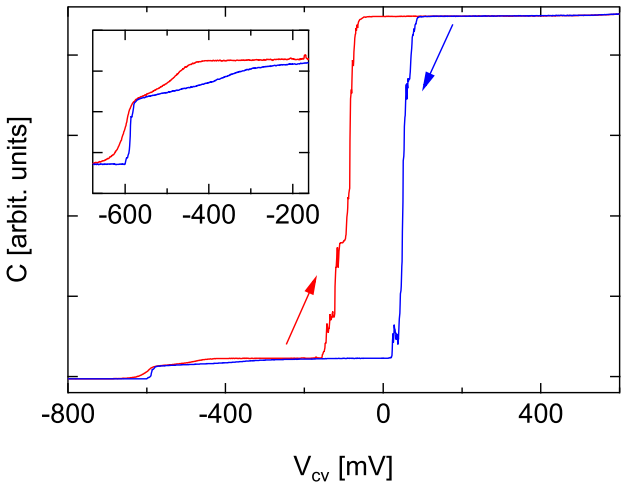

Figure 4.6: C-V spectroscopy curve. Capacitance between top gate and 2DEG as a function of the applied dc voltage V_{CV}. The steep drop is attributed to the 2DEG with a hysteresis between down (blue) and up (red) sweep direction. An indication for the presence of SAQDs could be the step-like smaller feature (see also inset), but does not show any orbital characteristics.

signal between $-600\,\mathrm{mV} < V_{\mathrm{CV}} < -200\,\mathrm{mV}$ was attributed to SAQDs in Ref. [129], but is lacking orbital resolution. A proper interpretation of our C-V data is difficult. Due to the rather low SAQD density, the effective signal might be simply too small to be detected. However, higher SAQD density samples did also not show clear signature of QD charging/de-charging. For the doped inverted 2DEG structure it is not clear at which potential and at which rate this is expected to happen.

In comparison to the I-V curves of the 2DEG (not shown), the steep drop around $V_{\mathrm{CV}} = 0$ can be related to the depletion of the 2DEG. Sweeping V_{CV} from $+600\,\mathrm{mV}$ to $-1\,\mathrm{V}$, the current through the the 2DEG drops to 0 (zero conductance) at a similar voltage as the C-V signal, also with a pronounced hysteresis. Although complete depletion (electron density $n = 0$) is expected around $V_{\mathrm{CV}} \sim -700\,\mathrm{mV}$, localization of the charge carriers can occur at less negative voltage. Also note, that the 2DEG density n was measured to be slightly lower below the top gate compared to the QPC area.

4.4 Summary

In summary, we fabricated and measured hybrid 2DEG devices, on which we aligned lateral gate nanostructures to individual InAs SAQDs. Maintaining an ultra clean wafer surface during the fabrication process, high precision localization of single SAQDs with an AFM is possible. QPC split gates were added in close vicinity to probe the potential of the SAQD. Electrostatic gating permits the formation of 1D channels, despite hysteresis effects and a 2DEG depth of 500 nm. The conductance in the QPC shows no quantization steps and is dominated by mesoscopic fluctuations due to the variations in the (disorder) potential, coming from remote donors and/or SAQDs and leading to backscattering. Quantization is not restored in absence of SAQDs, explained by remote donor atoms as the main source of potential fluctuations. Migration of Si towards the heterointerface is a known issue during growth of inverted structures. Using a third gate above the SAQD, local potential changes did not result in a clear signal of single charging events. To reach the goal of a successful sensitive single electron quantum transport charge sensor, a reduction of the potential variations is required. Further, fundamental adjustments in the design and fabrication method of the QPC (e.g. etch defined QPC), may result in a modified potential landscape, more suitable for deep, inverted 2DEGs.

5 Electrical Spin Protection and Manipulation via Gate-Locked Spin-Orbit Fields

F. Dettwiler, P. Weigele

D. M. Zumbühl

Department of Physics, University of Basel, CH-4056 Basel, Switzerland

J. Fu, J. C. Egues

Instituto de Física de São Carlos, Universidade de São Paulo, 13560-970 São Carlos, São Paulo, Brazil

S. Mack, D. D. Awschalom

Center for Spintronics and Quantum Computation, University of California, Santa Barbara, California 93106, USA

This chapter is in preparation for publication

5.1 Introduction

The spin-orbit (SO) interaction couples electron spin and momentum via a relativistic, effective magnetic field. While conveniently facilitating coherent spin manipulation [28, 62, 63] in semiconductors, the SO interaction also inherently causes spin relaxation [18, 145, 146]. A unique situation arises when the Rashba and Dresselhaus SO fields are matched [30, 81, 147], strongly protecting spins from relaxation, as recently demonstrated [31, 32]. Spintronics devices such as the paradigmatic spin transistor [28, 29] could vastly benefit if such spin protection could be expanded from a single point into a broad range accessible with *in-situ* gate-control, making possible tunable SO rotations under protection from relaxation.

Here, we demonstrate broad, independent control of all relevant SO fields in GaAs quantum wells, allowing us to tune the Rashba and Dresselhaus SO fields while keeping both *locked* to each other using gate voltages. Thus, we can electrically control and simultaneously protect the spin. Our experiments employ quantum interference corrections to electrical conductivity as a sensitive probe of SO coupling. Finally, we combine transport data with numerical SO simulations to precisely quantify all SO terms.

5.2 Universal Control of the Individual SO Parameters in GaAs Quantum Wells

Spin-orbit coupling in a GaAs 2D electron gas (2DEG) has two dominant contributions: the Rashba [71] and the Dresselhaus [77] effect, arising from breaking of structural and crystal inversion symmetry, respectively. The Rashba coefficient α is proportional to the electric field in the quantum well (QW) and can be tuned with the doping profile [31] as well as *in-situ* using gate voltages [72, 148]. We achieve independent control of α and carrier density n by using both top and back gates [73, 74], at voltages V_T and V_B, respectively. To modify α at constant density, a change of V_T can be compensated

by an appropriate change of V_B (see Fig. 5.1a), controlling α via a change of the gate-induced average electric field δE_Z, where $z \perp$2DEG. Note that α can be continuously tuned to change sign.

The Dresselhaus term [77], on the other hand, can be decomposed into sin/cos-functions [103] of θ (1st harmonic) and 3θ (3rd harmonic), with polar coordinate θ of the momentum $\mathbf{k}$ in the 2DEG plane. The first harmonic has a coefficient $\beta = \beta_1 - \beta_3$ comprised of $\beta_1 = \gamma\langle k_z^2\rangle$ and $\beta_3 = \gamma k_F^2/4$, where $k_F = \sqrt{2\pi n}$ is the Fermi wave number, $\gamma > 0$ is the bulk Dresselhaus parameter and $\langle k_z^2\rangle$ depends on the width W of the well [149], with $\langle k_z^2\rangle = (\pi/W)^2$ for infinite barriers. In addition, β_3 is the coefficient of the 3rd harmonic Dresselhaus term – hereafter cubic term – and depends on density n, thus enabling gate-control. The cubic term breaks the angular symmetry of the other terms and is relatively small compared to β_1 since $\langle k_z^2\rangle \gg k_F^2/4$, except for the largest densities used. To control β_1, we studied QWs of width $W = 8, 9.3, 11$ and 13 nm, yielding wave functions spreading over the full well width and $\langle k_z^2\rangle < (\pi/W)^2$, see Fig. 5.2d, due to wave function penetration into the finite barriers. Over this range, β_1 changes by a factor 2 and is essentially independent of gate voltage.

Thus, we can set β_1 in discrete steps via QW width, and we achieve independent, continuous control of α and β_3 *in-situ* using top and back gates. This wide tunability makes it possible to change α while *locking* β to match α via gate-control of β_3, thus strongly protecting spins from relaxation. In previous experiments, the Rashba and Dresselhaus fields were matched only at isolated points [31, 32, 105], not over a broad range. Finally, the broad gate-tunability gives us access to various SO regimes, such as the Dresselhaus (Rashba) regime $\beta \gg \alpha$ ($\alpha \gg \beta$), and allows a detailed characterization of the cubic term, which limits the spin lifetime even at $\alpha = \beta$.

5.3 Suppression of Weak Antilocalization and Protection from Spin Relaxation

Weak antilocalization (WAL) is a well established signature of SO coupling in magnetoconductance (MC) $\sigma(B_Z)$ [91, 101, 103, 104, 150, 151]. For the $|\alpha| = \beta \gg \beta_3$ regime, the resulting internal SO magnetic field $\mathbf{B}_{\text{int}}(\mathbf{k})$ (see Chapter 5.6) is uniaxial and vanishes for $\mathbf{k}$ along one direction in the 2DEG plane ($\hat{x}_-$ for $\beta = +\alpha$, or $\hat{x}_+ (\perp \hat{x}_-)$ for $\beta = -\alpha$). Therefore, WAL (maximal $\sigma(B_Z = 0)$) is suppressed and the effectively spin-less situation exhibiting weak localization (WL) (minimal $\sigma(B_Z = 0)$) is restored [30, 81, 101, 105]. We introduce the SO lengths $\lambda_\pm = \hbar^2/(2m^* |\alpha \pm \beta|)$ (with Planck constant $\hbar$ and effective mass m^*) as the *ballistic* length to be traveled along $\hat{x}_\pm$, respectively, for a spin rotation of one radian. For $\beta = +\alpha$, λ_- diverges (no precessions) while λ_+ is finite, and vice versa for $\beta = -\alpha$. We note that a closed-form theory of MC including all relevant SO terms is not currently available [91, 101, 103, 104], making extraction of the SO parameters from MC difficult.

5.3.1 Locked $\alpha = \beta$ in Asymmetrically Doped Quantum Wells

Figure 5.1b displays the MC of the 9.3 nm QW for configurations labeled $1-7$, showing a transition from WAL (1 & 2) to WL (4 & 5) back to WAL (7) upon monotonically changing α on a contour of constant density, see Fig. 5.1a. Selecting the most pronounced WL curve allows us to determine the symmetry point $\alpha \approx \beta$. This scheme is repeated for a number of densities, yielding the symmetry point as a function of n. Thus, Rashba and Dresselhaus fields can be locked with gate voltages over a wide range (see Fig. 5.2a, blue markers), varying n by a factor of 2. Numerical simulations [152] (see Chapter 5.5) can accurately calculate α and $\langle k_z^2 \rangle$. This leaves only one fit parameter: γ, the bulk Dresselhaus coefficient, which can now be extracted from fits to the density dependence of the symmetry point, see solid blue line in Fig. 5.2a, giving excellent agreement. Further, the WL dip – often used to determine phase coherence

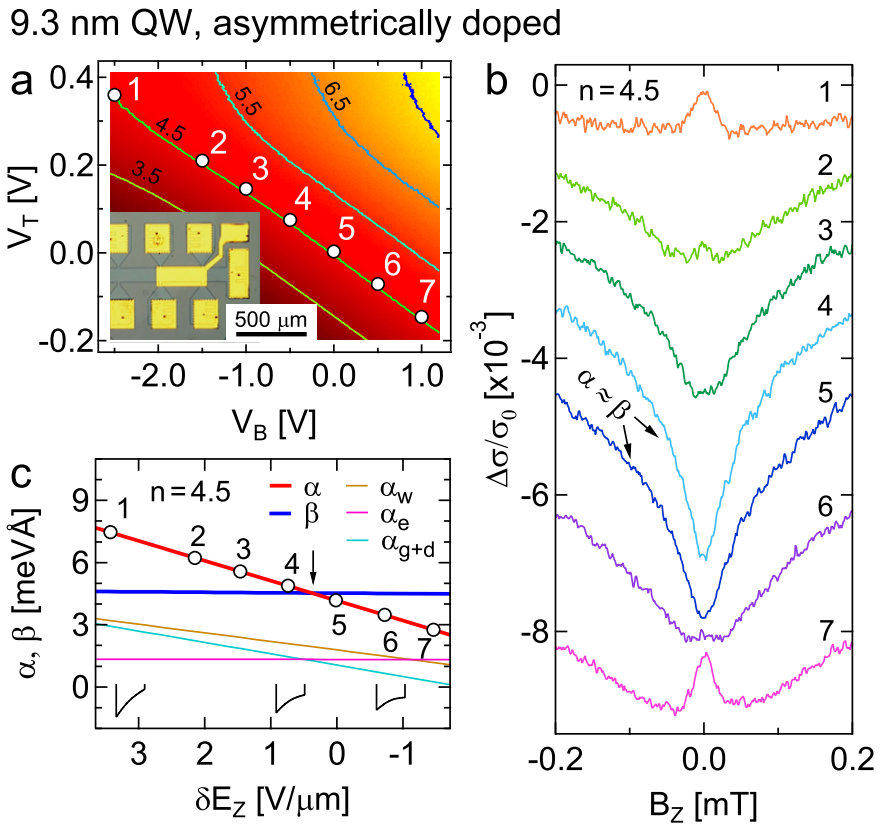

Figure 5.1: Weak localization (WL) as an $\alpha = \beta$ detector; gate-control of Rashba α at constant density. **(a)** Measured charge density n (color) versus top gate voltage V_T and back gate voltage V_B (9.3 nm QW). Contours of constant density $3.5 - 7.5 \cdot 10^{11}\,\mathrm{cm}^{-2}$ are shown. Inset: optical micrograph of typical Hall bar, with contacts (yellow), gate (center) and mesa (black lines). **(b)** Normalized longitudinal conductivity $\Delta\sigma/\sigma_0 = (\sigma(B_Z) - \sigma(0))/\sigma(0)$ versus $B_Z \perp$ 2DEG. Curves for gate configurations $1 - 7$ along constant $n = 4.5 \cdot 10^{11}\,\mathrm{cm}^{-2}$ are shown (offset vertically), also labeled in panels **a** and **c**. **(c)** Simulated Rashba α and Dresselhaus β coefficients (see text) against gate-induced field change δE_Z, shown for constant $n = 4.5 \cdot 10^{11}\,\mathrm{cm}^{-2}$. The δE_Z axis – decreasing from left to right – corresponds exactly to the V_B abscissa of panel **a** for a covarying V_T such that $n = 4.5 \cdot 10^{11}\,\mathrm{cm}^{-2}$ constant. Sketches of the QW potential at 1, 4 and 6 illustrate the change of α with δE_Z. Note that $\alpha(\delta E_Z = 0) \neq 0$ since the external E-field (see Chapter 5.6) is not zero at $\delta E_Z = 0$.

– sensitively depends on the SO coupling (e.g. curves $3-6$ in Fig. 5.1b), even before WAL appears. Negligence of SO coupling could thus lead to spurious or saturating coherence times.

5.3.2 Extraction of SO Parameters

Next, we change the Dresselhaus coefficient β_1 by varying the QW width and repeating the above procedure, summarized in Fig. 5.2a. For wider QWs, a smaller β_1 results, shifting the symmetry point towards smaller α, i.e. towards the lower right in Fig. 5.2a. As seen, locking of $\alpha = \beta$ is achieved in all present wavers. Further, reduced β_1 makes possible the Rashba regime $\alpha \gg \beta$, particularly in the upper left of Fig. 5.2a where α is large. Again performing fits over the density dependence of the symmetry point for each QW width, we obtain very good agreement, see Fig. 5.2a, and extract $\gamma = 11.6 \pm 1\,\mathrm{eV\AA}^3$ consistently for all QWs (Fig. 5.2c). We emphasize that γ is notoriously difficult to calculate and measure [91, 104]; the value reported here agrees well with recent studies [32, 79, 153].

The Rashba coefficient is composed of $\alpha = \alpha_{\mathrm{g+d}} + \alpha_{\mathrm{w}} + \alpha_{\mathrm{e}}$ in the simulation, with gate and doping term $\alpha_{\mathrm{g+d}}$, QW structure term α_{w}, and Hartree term α_{e}. Along a contour of constant density, mainly $\alpha_{\mathrm{g+d}}$ and α_{w} are modified, while α_{e} and β remain constant, see Fig. 5.1c. The density dependence for locked $\alpha = \beta$ (see Fig. 5.2b)) shows that while β_1 is nearly constant, β_3 is linearly increasing with n, thus reducing $\beta = \beta_1 - \beta_3$, and therefore forcing a corresponding reduction of α to keep $\alpha = \beta$ matched. The Hartree term α_{e}, however, increases for growing n. This is compensated by the other α-terms to nicely match $\beta(n)$, see Fig. 5.2b. Here, a change of $\sim 25\%$ in SO strength (~ 4 to $\sim 5\,\mathrm{meV\AA}$) corresponds to a gate-controlled spin rotation of $\pi/2$ over a precession length of $5\,\mu$m, which is clearly shorter than the spin diffusion length over the whole range, thus enjoying protection from spin relaxation.

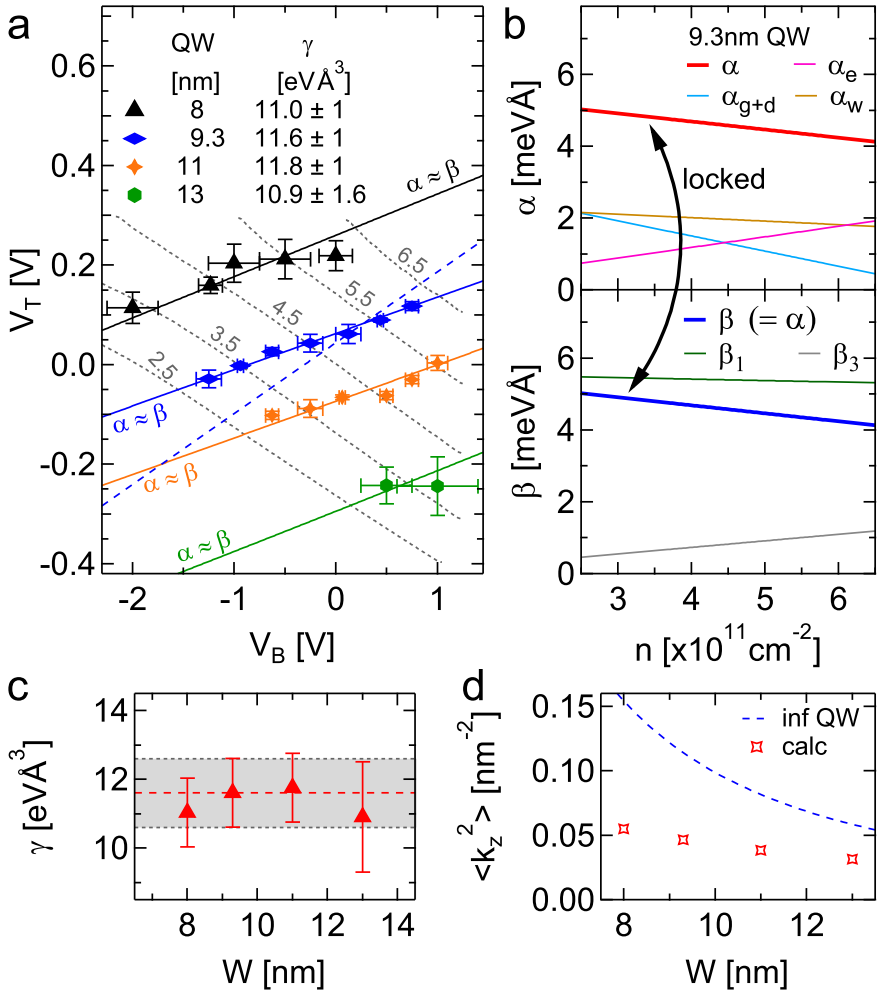

Figure 5.2: Tuning and locking $\alpha = \beta$. **(a)** The markers indicate $\alpha \approx \beta$ for four different QW widths (asymmetric doping) and various densities (gray contours of constant n, labeled in units of $10^{11}\,\mathrm{cm}^{-2}$) in the V_T and V_B plane. Error bars result from the finite number of MC traces in the (V_B, V_T)-space. Theory fits (solid lines) are shown for each QW, with γ as the only fit parameter (inset table, error bars dominated by systematic error, see below). The dashed blue line indicates the slope of constant $\alpha = \beta_1$, neglecting β_3, which is inconsistent with the data. **(b)** Simulation of locked $\alpha = \beta$ versus density n along solid blue line from **a**, showing the various SO contributions (see text). **(c)** Values of γ from fits for each well width W. Red dahed line is the average $\gamma = 11.6 \pm 1\,\mathrm{eV\AA}^3$ (excluding the 13 nm well due to its larger error), gray the $\sim 9\%$ error, stemming mostly from the systematic uncertainty in the input parameters of the simulations (see Chapter 5.5). **(d)** $\langle k_z^2 \rangle$ as a function of QW width W for realistic (markers) and infinite (blue) potential.

5.3.3 Symmetrically Doped Quantum Well

We now show that α can be tuned through β *and through zero* in a more symmetrically doped wafer, opening the Dresselhaus regime $\beta \gg \alpha$. We introduce the magnetic field B_{SO} where the MC exhibits minima at $B_{\mathrm{Z1}} \approx -B_{\mathrm{Z2}}$. Beyond the WAL-WL-WAL transition (Fig. 5.3b upper panel), B_{SO} is seen to peak and decrease again (dashed curve). The gate voltages with maximal B_{SO} are added to Fig. 5.3a for several densities (red markers). We surmise that these points mark $\alpha \approx 0$: B_{SO} signifies the crossover between WL/WAL-like MC, thus defining an empirical measure for the effects of SO coupling (larger B_{SO}, stronger effects). For $\alpha = 0$, the full effect of β on MC becomes apparent without cancellation from α, giving a maximal B_{SO}. Indeed, the simulated $\alpha = 0$ curve (dashed red line in Fig. 5.3a) cuts through the experimental points, also reflected in Fig. 5.3c by a good match with the simulated $\alpha = 0$ crossing point (red arrow).

5.3.4 Effective Spin-Orbit Length

For a comparison of experiment and simulation, we convert the empirical B_{SO} to a magnetic length $\lambda_{\mathrm{SO}} = \sqrt{\hbar/2eB_{\mathrm{SO}}}$, where $e > 0$ is the electron charge and the factor of two accounts for time-reversed pairs of closed trajectories. Fig. 5.4 shows the theoretical spin diffusion length λ_{eff} (see Chapter 5.5) and the ballistic $\lambda_{\pm}$, together with the experimental λ_{SO}, all agreeing remarkably well. First, we note that the ballistic $\lambda_{\pm}$ and the diffusive λ_{eff} (small β_3) are equivalent. The enhanced λ_{SO} around $\alpha/\beta = 1$ corresponds to an increased spin relaxation time $\tau_{\mathrm{SO}} = \lambda_{\mathrm{SO}}^2/(2D)$. Second, $\max(\lambda_{\pm})$ quantifies the deviation from the *uniaxial* $\mathbf{B}_{\mathrm{int}}(\mathbf{k})$ at $\alpha = \beta$ and thus the extent to which spin rotations are not undone in a closed trajectory due to the non-Abelian nature of spin rotations around non-collinear axes. This leads to WAL, a finite B_{SO} and $\lambda_{\mathrm{SO}} \simeq \max(\lambda_{\pm})$, as observed (see Fig. 5.4). Unlike the corresponding time scales, the SO lengths are only weakly dependent on density and mobility when plotted against α/β, allowing a comparison of various densities.

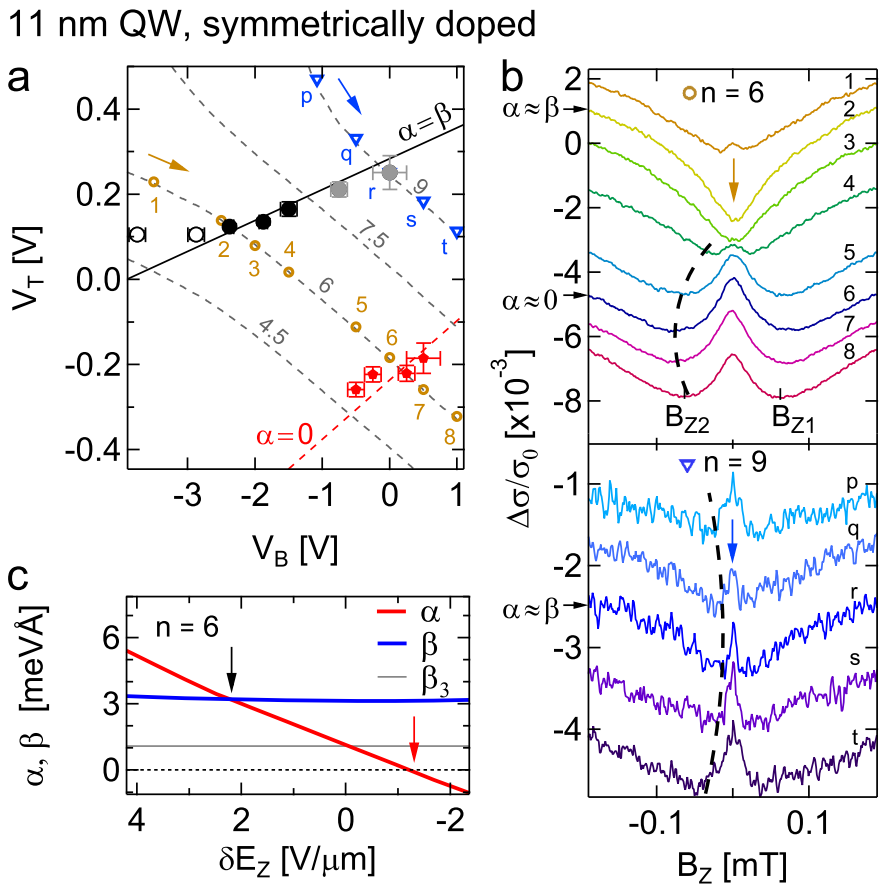

Figure 5.3: The Dresselhaus and the cubic regime. **(a)** Locked regime $\alpha \approx \beta$ (black/gray symbols) and Dresselhaus regime $\alpha \approx 0$ (red symbols) from the broadest WAL minima (maximal B_{SO}) in the V_T and V_B plane for a more symmetrically doped 11 nm QW. The solid black line displays the $\alpha = \beta$ simulation, while the dashed red line marks the simulated $\alpha = 0$ contour. Open black markers (leftmost V_B) are entering the non-linear gate regime, causing a slight deviation from theory, which assumes linear gate action. The rightmost V_B points (gray) are obtained from the minimal B_{SO} in presence of WAL. **(b)** MC sequences at $n = 6 \cdot 10^{11}\,\mathrm{cm}^{-2}$ (upper panel) and $n = 9 \cdot 10^{11}\,\mathrm{cm}^{-2}$ (lower panel), shifted vertically for clarity. Each brown/blue marker in **a** corresponds to a trace in **b**, as labeled by numerals/letters. B_{SO} is indicated as a guide for the eye by black dashed curves for negative B_Z. **upper panel** B_{SO} increases and peaks (indicating $\alpha = 0$) before decreasing again. **lower panel** broken spin symmetry regime: WAL is no longer suppressed here due to symmetry breaking from the cubic term at large n. Still, $\alpha \approx \beta$ can be identified with the narrowest WAL peak. **(c)** Simulation of α and β along $n = 6 \cdot 10^{11}\,\mathrm{cm}^{-2}$. α traverses both β (black arrow) and for smaller δE_Z also zero (red arrow).

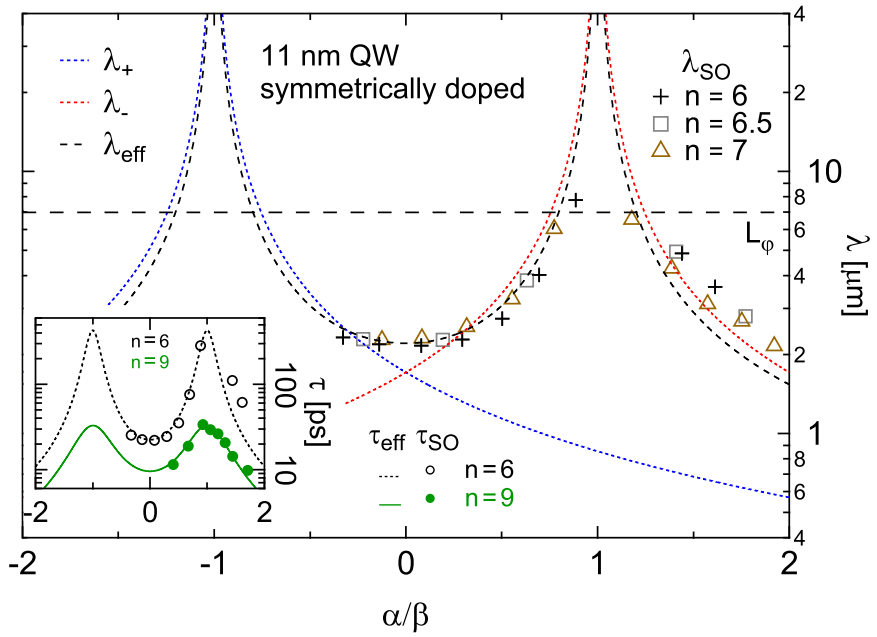

Figure 5.4: Experimental and theoretical SO-lengths and SO-times. Experimental $\lambda_{\mathrm{SO}} = \sqrt{\hbar/2eB_{\mathrm{SO}}}$ (markers, densities as labeled, in units of $10^{11}\,\mathrm{cm}^{-2}$) as a function of the dimensionless ratio α/β (from SO simulation). The ballistic $\lambda_{\pm}$ (blue/red dashes) and effective λ_{eff} (black dashed curve) are only weakly n-dependent (small β_3) when plotted against α/β. Thus, curves for only one density ($n = 6 \cdot 10^{11}\,\mathrm{cm}^{-2}$) are shown. The experimental uncertainty on λ_{SO} is captured by the spread given by the three slightly different densities. The coherence length $L_\varphi \approx 7\,\mu\mathrm{m}$ is added for illustration (obtained from WL curves), setting the visibility of SO effects in MC and thus the width of the WAL-WL-WAL transition. Inset: experimental spin relaxation time $\tau_{\mathrm{SO}} = \lambda_{\mathrm{SO}}^2/(2D)$ (circles) as a function of α/β for two densities as indicated. Theory curves τ_{eff} (dashed) now include the symmetry breaking third harmonic term, preventing divergence at $\alpha/\beta = 1$, while λ_{eff} (main panel) does not.

The cubic term causes spin relaxation even at $\alpha = \beta$ and becomes visible at large densities: WAL is present in all traces and through $\alpha = \beta$ (Fig. 5.3b, lower panel), because $\mathbf{B}_{\text{int}}(\mathbf{k})$ can no longer be made uniaxial, thus breaking spin symmetry and reviving WAL. A partial symmetry restoration is still apparent, where – in contrast to the $\alpha = 0$ case – a *minimal* B_{SO} is reached (dashed curves) consistent with $\alpha = \beta$ (gray markers Fig. 5.3a at large n). We include the cubic β_3 in the spin relaxation time τ_{eff} (see Chapter 5.5), shown in the inset of Fig. 5.4 for two densities, finding good agreement with the experimental $\tau_{\text{SO}} = \lambda_{\text{SO}}^2/(2D)$, where D is the diffusion constant. Over the whole locked regime of Fig. 5.2b, WAL is absent, and τ_{SO} is enhanced between one and two orders of magnitude compared to $\alpha = 0$. Finally, the coherence length L_φ sets an upper limit for the visibility of SO effects: WAL is suppressed for $\lambda_{\text{eff}} \gg L_\varphi$, setting the width of the WAL-WL-WAL transition (see Chapter 5.6).

5.4 Outlook

As an outlook, this work is laying the foundation for a new generation of experiments benefiting from unprecedented command over SO coupling in semiconductor nanostructures such quantum wires, quantum dots, and electron spin qubits. We note that analogous SO control is in principle also possible in other semiconductors. Finally, SO coupling is crucial beyond spintronics and quantum computation, e.g. for novel states of matter such as helical states, topological insulators, Majorana fermions and parafermions.

5.5 Materials and Methods

GaAs QW materials. The QWs are grown on an n-doped substrate (for details see Chapter 5.6) and fabricated into Hall bar structures (see inset, Fig. 5.1a) using standard photolithographic methods. The 2DEG is contacted by thermally annealed GeAu/Pt Ohmic contacts, optimized for a low 2DEG contact resistance while maintaining high back gate tunability (low leakage currents) and avoiding short circuits to the back gate. On one segment of the Hall bar, a Ti/Au top gate with dimensions of $300\,\mathrm{x}\,100\,\mu m$ was deposited. The average gate-induced E-field change in the QW is defined as $\delta E_Z = 1/2\,(V_T/d_T - V_B/d_B)$, with effective distance $d_{T/B}$ from the QW to the top/back gate, extracted using a capacitor model, consistent with the full quantum description (see Chapter 5.6). Contours of constant density follow $\delta V_T/d_T = -\delta V_B/d_B$. Deviations from linear behavior appear at most positive/negative gate voltages due to incipient gate leakage and hysteresis.

Low temperature electronic measurements. The experiments are performed in a dilution refrigerator with base temperature $T_b = 20\,\mathrm{mK}$. We have used a standard four-wire lock-in technique at 133 Hz and 100 nA current bias, chosen to avoid self-heating while maximising the signal. The density is determined with Hall measurements in the classical regime, whereas Shubnikov-de Haas oscillations were used to exclude occupation of the second subband, which is the case for all the data discussed. The WAL signature of MC is a small correction (10^{-3}) to total conductance. To achieve a satisfactory signal-to-noise ratio, longitudinal conductivity traces $\Delta\sigma/\sigma_0 = (\sigma(B)-\sigma(0))/\sigma(0)$ were measured at least 10 times and averaged.

Numerical Simulations. The simulations calculate the Rashba coefficient α and $\langle k_z^2 \rangle$ based on the bulk semiconductor band parameters, the QW structure, the measured QW electron densities and the measured gate lever arms. We solve the Schrödinger and Poisson equations self consistently ("Hartree approximation"), obtain the self-consistent eigenfunctions, and then determine α via appropriate expectation values

[152]. The Dresselhaus coefficient γ is extracted from fits of the simulation to the experiment which detects the absence of WAL at $\alpha = \beta = \gamma(\langle k_z^2 \rangle - k_F^2/4)$. Thus, given α and $\langle k_z^2 \rangle$ from the simulation and the measured $n = k_F^2/(2\pi)$, we obtain $\gamma = 11.6 \pm 1\,\mathrm{eV\AA^3}$ consistently for all asymmetrically doped QWs. Taking into account the uncertainties of the band parameters, the experimental errors and a negligible uncertainty on $\langle k_z^2 \rangle$, an overall uncertainty of about $9 - 10\%$ or about $\pm 1\,\mathrm{eV\AA^3}$ on γ results. About $1-2\%$ error originates from the experimental uncertainty of determining $\alpha = \beta$. The doping distribution (above/below QW) is not expected to influence γ, and hence we use the same γ for the more symmetrically doped wafer. Fits to the $\alpha = \beta$ experimental points then determine how much charge effectively comes from upper rather than lower doping layers, fixing the last unknown parameter also for the more symmetrically doped QW (see Chapter 5.6).

Spin-dephasing times and lengths. In WL/WAL measurements, additional spin dephasing is introduced by the external magnetic field B via the Aharonov-Bohm phase arising from the magnetic flux enclosed by the time reversed trajectories: $\Delta\varphi = 2eAB/\hbar$, where A is the loop area. Here we take $A = \lambda_{\mathrm{SO}}^2 = 2D\tau_{\mathrm{SO}}$ as a characteristic "diffusion area" probed by our WL/WAL experiment, with τ_{SO} being the spin dephasing time, and λ_{SO} the spin diffusion length. By taking $\Delta\varphi = 1$ (rad) at $B = B_{\mathrm{SO}}$, we can extract τ_{SO} from the minima of the WAL curves, which yields $\tau_{\mathrm{SO}} = \hbar(4eDB_{\mathrm{SO}})^{-1}$. The factor of 4 here stems from the two time-reversed paths and the diffusion length.

Effective SO times and lengths. Theoretically, we determine τ_{SO} via a spin random walk process (D'yakonov-Perel (DP)). The initial electron spin in a loop can point (with equal probability) along the s_{x_-}, s_{x_+}, and s_z axes (analogous to x_+, x_-, and z, respectively), which have unequal spin-dephasing times $\tau_{\mathrm{DP},\mathrm{s_{x_-}}}$, $\tau_{\mathrm{DP},\mathrm{s_{x_+}}}$, and $\tau_{\mathrm{DP},\mathrm{s_z}}$. Hence, for unpolarized, independent spins, we take the average $\tau_{\mathrm{eff}} = (\tau_{\mathrm{DP},\mathrm{s_{x_-}}} + \tau_{\mathrm{DP},\mathrm{s_{x_+}}} + \tau_{\mathrm{DP},\mathrm{s_z}})/3$ which leads to an average spin dephasing length $\lambda_{\mathrm{eff}} = \sqrt{2D\tau_{\mathrm{eff}}}$. In the Chapter 5.6, we discuss the spin random walk and provide expressions for the DP times including corrections due to the cubic β_3 term. Figure 4 shows curves for the

spin dephasing times and lengths presented here. In the main panel, the cubic β_3 is neglected in λ_{eff} since for $n \leq 7 \cdot 10^{11}\,\text{cm}^{-2}$, WL appears at $\alpha = \beta$ (small β_3). In contrast, the cubic term is included in τ_{eff} in the inset since at the higher density $n = 9 \cdot 10^{11}\,\text{cm}^{-2}$, WAL persists (sufficiently strong β_3).

Acknowledgments

We would like to thank A. C. Gossard, D. Loss, D. L. Maslov, G. Salis for valuable inputs and stimulating discussions. This work was supported by the Swiss Nanoscience Institute (SNI), NCCR QSIT, Swiss NSF, ERC starting grant, EU-FP7 SOLID and MICROKELVIN, US NSF and ONR, Brazilian grants FAPESP, CNPq, PRP/USP (Q-NANO), and natural science foundation of China (Grant No. 11004120).

5.6 Supplementary Information

5.6.1 Wafer Structure

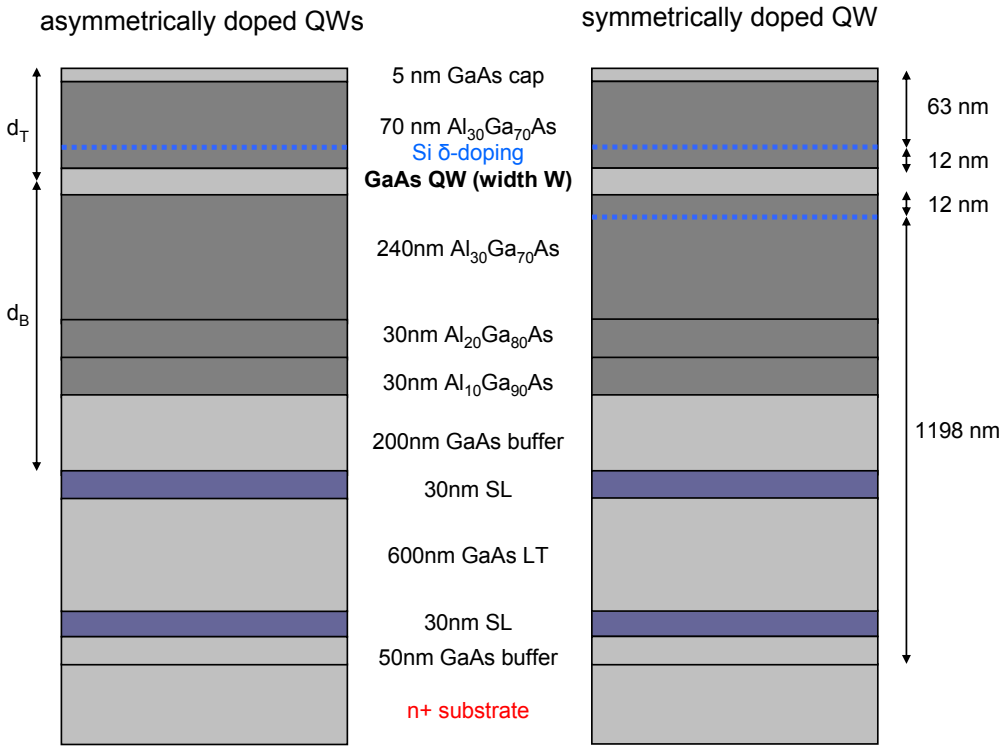

Figure 5.5: Quantum well wafer profiles. MBE growth profiles of the asymmetrically (left) and more symmetrically (right) doped QW wafers. The GaAs QW width W is $8, 9.3, 11$ and $13\,\mathrm{nm}$ for the asymmetric and $11\,\mathrm{nm}$ for the symmetric QW, respectively.

The quantum well (QW) samples are grown on (001) n-doped substrates, serving as a back gate, with total distance of $1210\,\mathrm{nm}$ between back gate and QW, including $600\,\mathrm{nm}$ of low-temperature (LT) grown GaAs, see Fig. 5.5. The LT GaAs creates a barrier by pinning the Fermi level midgap [154]. Thus, in a simple plate capacitor model, the effective distance d_B between QW and back gate is reduced by the thickness of the LT barrier, increasing the range of tunability and reducing leakage currents at the same time. Similarly, d_T is defined as the distance between QW and top gate. Good agreement is found between $d_{B/T}$ extracted from the measured back/top gate

dependence of the carrier density and the as-grown thicknesses of the layers in the QW structure. The QWs are 75 nm below the surface with a setback of 12 nm to the Si δ-doping layer above the well for the asymmetric QWs with $W = 8, 9.3, 11$ and 13 nm and an additional doping layer 12 nm below the 2DEG for the more symmetric 11 nm QW.

Using top and back gates, the density is tunable in a range of $n \approx 2$ - $8 \cdot 10^{11}\,\mathrm{cm}^{-2}$ (Fig. 5.6a) corresponding to mobilities $\mu \approx 2$ - $20\,\mathrm{m}^2/(\mathrm{Vs})$ (Fig. 5.6b). Tunability is limited by onset of gate leakage and hysteresis issues. For positive $V_T > 300\,\mathrm{mV}$ and large negative $V_B < -2\,\mathrm{V}$, a non-linear gate dependence is observed. Shubnikov-de Haas measurements indicate that all data in this study are in the single 2D subband regime, consistent with the numerical simulations. For low densities $n \lesssim 2 \cdot 10^{11}\,\mathrm{cm}^{-2}$, WAL as a signature of SO coupling becomes very weak or disappears due to the small wave number $k_F^2 = 2\pi n$. At even lower densities the electrons become strongly localized by disorder. Hence the lower left corners of Fig. 5.6a and b corresponding to low densities are not displayed.

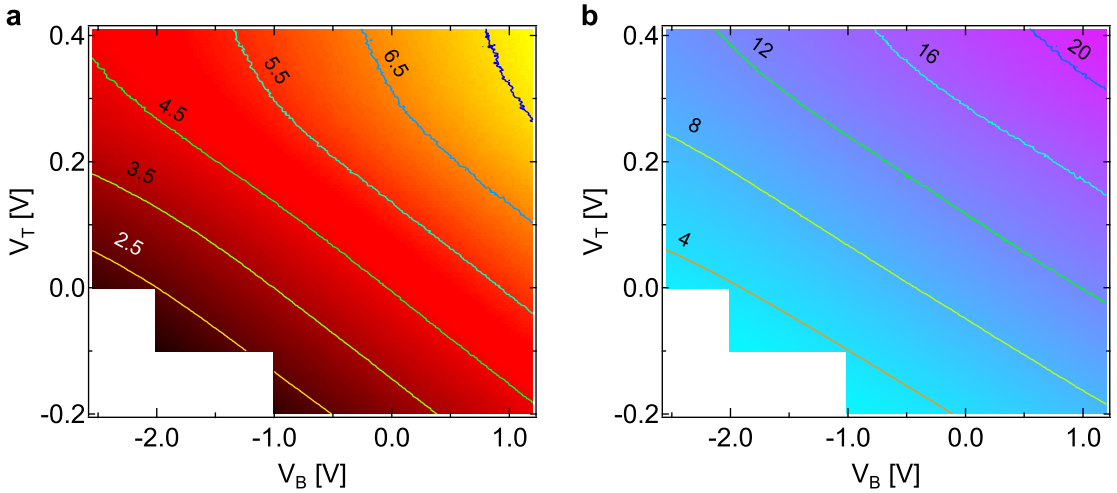

Figure 5.6: Density and mobility map of 9.3 nm QW. Charge carrier density n **(a)** and mobility μ **(b)** as a function of top gate voltage V_T and back gate voltage V_B. Contour lines are labeled in units of $10^{11}\,\mathrm{cm}^{-2}$ **(a)** and $\mathrm{m}^2/(\mathrm{Vs})$ **(b)**, respectively. The lower left corner was omitted due to a general lack of WAL at low n.

5.6.2 Temperature Dependence

Elevated temperatures suppress quantum corrections to conductivity, as shown in Figure 5.7. The magnetic field position B_{SO} of the MC minima, however, appears not affected by temperature (dashed line in Fig. 5.7), consistent with a spin-orbit (SO) length λ_{SO} independent of T. At elevated temperatures, WAL and the B_{SO} minima are shallower and eventually can disappear, due to loss of coherence. This leads to a broadening of the WAL-WL-WAL transition with increasing temperature, i.e. the size of the gate voltage range where WAL is suppressed grows with increasing temperature, see Fig. 5.8 from left to right. Thus, in absence of symmetry breaking effects of the higher harmonic β_3, the phase coherence defines the width of the WAL-WL-WAL transition in our experiment.

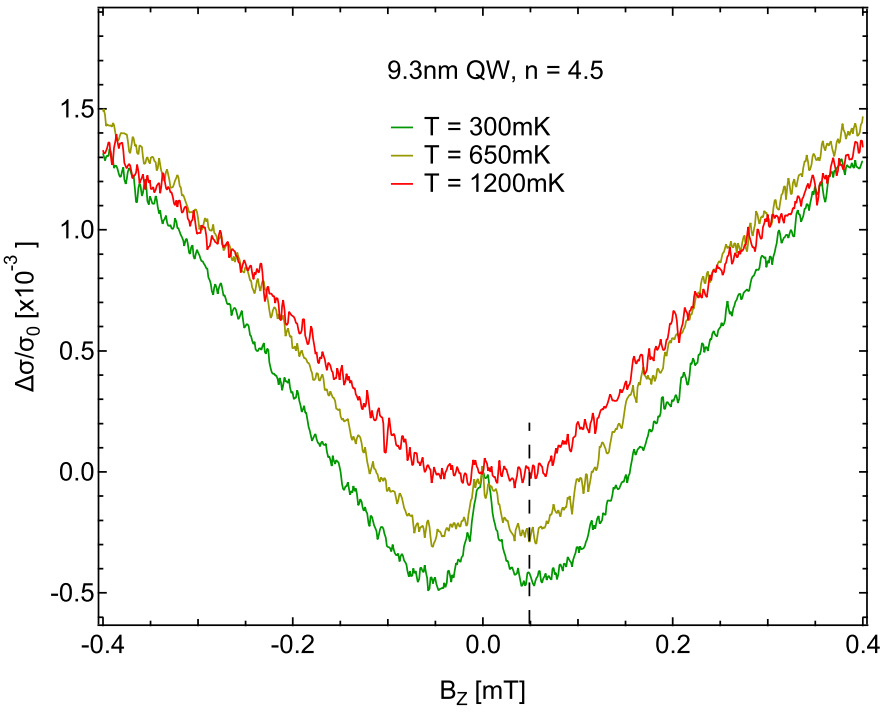

Figure 5.7: Temperature dependence of WAL. Magnetoconductance for a specific gate configuration (9.3 nm QW, $n = 4.5 \cdot 10^{11}\,\mathrm{cm}^{-2}$, $V_T = -146\,\mathrm{mV}$, $V_B = 1\,\mathrm{V}$) showing clear WAL signature at $T = 300\,\mathrm{mK}$ (green). The WAL maximum at $B_Z = 0$ weakens for $T = 650\,\mathrm{mK}$ (olive), and essentially disappears at $T = 1200\,\mathrm{mK}$ (red). The position of the MC minima (defined as B_{SO}) appears to be not affected by temperature (dashed vertical line).

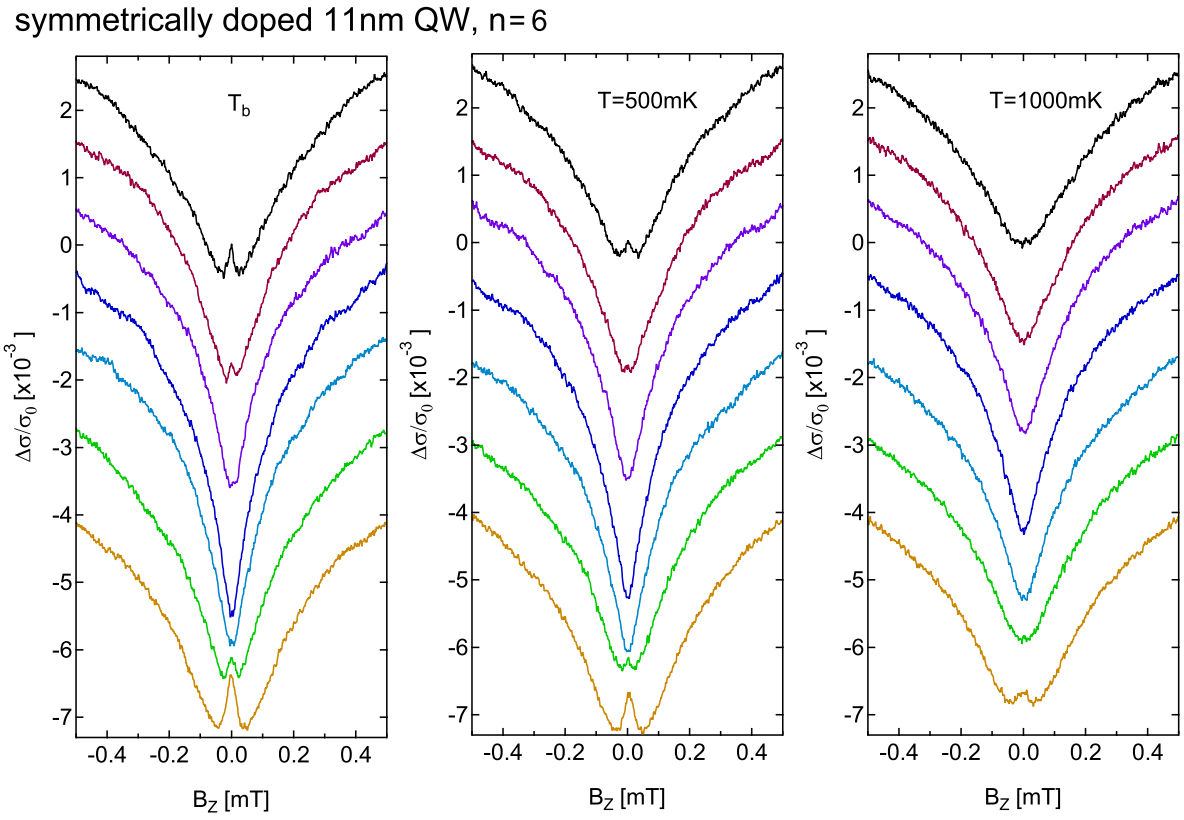

Figure 5.8: Temperature dependence of WAL-WL-WAL transition of the more symmetrically doped 11 nm QW, shown for base temperature (left panel), 500 mK (middle panel) and 1 K (right panel) for various (V_T, V_B) configurations (color coded) at constant density $n = 6 \cdot 10^{11}\,\mathrm{cm}^{-2}$. The curves are shifted vertically for clarity. Upon increasing T, WAL weakens and finally disappears on both sides of the low-T symmetry point (see e.g. green and dark brown curve), resulting in a widening of the transition.

5.6.3 Numerical Simulations

Self-consistent approach and potential The confining potential of our GaAs/$Al_{0.3}Ga_{0.7}As$ wells (see Fig. 5.9) contains [152]: (i) the structural part V_w arising from the band offset at the interfaces, (ii) the potential V_g from the top and back gates, which allows us to adjust the symmetry of the well profile and the electronic densities while keeping the chemical potential μ constant, (iii) the doping potential V_d, which remains fixed at low temperatures (we also use $V_{\mathrm{g+d}} = V_\mathrm{g} + V_\mathrm{d}$), and (iv) the electronic Hartree potential V_e which depends on carrier density. The 3D electron charge density in the well ρ_e depends on the total potential $V_\mathrm{sc} = V_\mathrm{w} + V_{\mathrm{g+d}} + V_\mathrm{e}$,

which in turn depends on ρ_{e} via the Hartree term. Hence to find the eigensolutions of the system, we solve the Schrödinger equation for electrons in the total potential $V_{\mathrm{sc}} = V_{\mathrm{w}} + V_{\mathrm{g+d}} + V_e$. Both V_{w} and $V_{\mathrm{g+d}}$ depend only on the z variable (growth direction). Within the Hartree approximation, the electron charge density is $\rho_e(z,\vec{r}) = 2\sum_{\nu,\vec{k}} |\varphi_{\nu,\vec{k}}(z,\vec{r})|^2 f_{k,\nu}$, where $\varphi_{\nu,\vec{k}}(z,\vec{r}) = \frac{1}{\sqrt{A}} \exp(i\vec{k}\cdot\vec{r})\psi_\nu(z)$ with $\psi_\nu(z)$ being the ν^{th} subband wave function of the well, $\vec{k}$ the in-plane electron wave vector, A a normalizing area, and $f_{k,\nu}$ the Fermi-Dirac distribution. Note that within the Hartree approximation, $\rho_e(z,\vec{r}) \to \rho_e(z)$ because of the plane wave dependence of the wave function in the xy-plane and hence the Hartree potential V_{e} depends only on z.

Upon summing over $\vec{k}$, $\rho_e(z)$ simplifies to $\rho_e(z) = \sum_\nu |\psi_\nu(z)|^2 n_\nu$, with the electron occupation of the ν^{th} subband $n_\nu = \frac{m^*}{\pi\hbar^2} k_B T \ln[1 + \exp(\mu - \mathcal{E}_\nu)/k_B T]$ and confinement energy $\mathcal{E}_\nu$. Here μ is the electron chemical potential, k_B the Boltzmann constant and T the absolute temperature. The areal electron density n in the well and $\rho_e(z)$ are related via $n = \int dz \rho_e(z) = \sum_\nu n_\nu$. Note that the Hartree potential V_e depends only on z. We then solve the resulting one-dimensional Schrödinger equation together with the Poisson's equation for the total charge density $\rho_{\mathrm{tot}}(z) = \rho_e(z) + \rho_{\mathrm{d}}(z)$, where $\rho_{\mathrm{d}}(z)$ denotes the ionized donor concentration profile. We obtain the subband energies $\mathcal{E}_\nu$ and wave functions $\psi_\nu(z)$ iteratively within this self consistent procedure when convergence is attained.

The potential profile and the corresponding wave function for the 9.3 nm well based on our self-consistent scheme are shown in Fig. 5.9 for top and back gates set to $V_T = 75\,\mathrm{mV}$ and $V_B = -500\,\mathrm{mV}$, respectively, corresponding to point 4 in Fig. 5.1.

Expressions for the SO coupling terms

Rashba spin-orbit coupling α. As shown in Ref. [152], the strength α of the Rashba coupling can be cast as the expectation value $\langle ... \rangle$ of the weighted derivatives of the

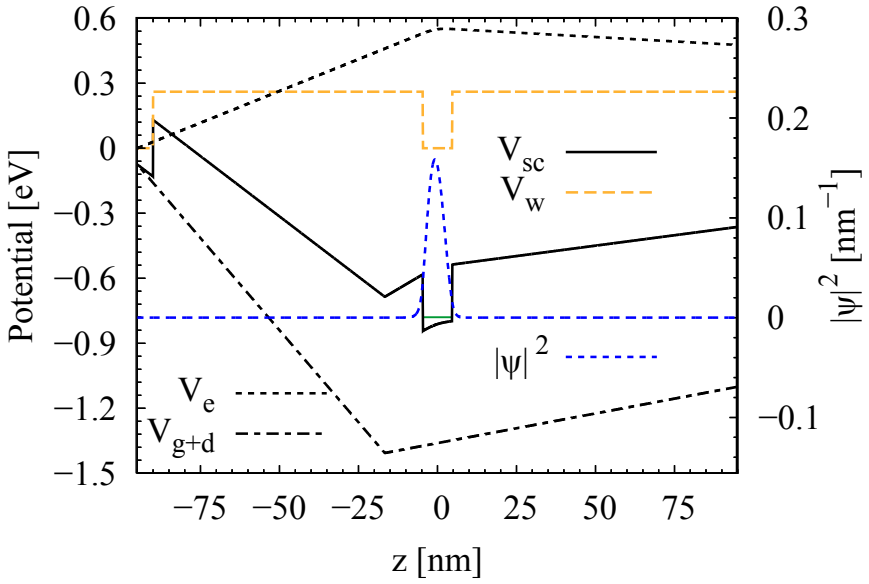

Figure 5.9: Self-consistent potential $V_{\rm sc}$ and the corresponding wave function Ψ for our GaAs/$Al_{0.3}Ga_{0.7}$As 9.3 nm quantum well with the top gate $V_T = 75$ mV and back gate $V_B = -500$ mV. The QW band offset potential $V_{\rm w}$, the electron Hartree potential $V_{\rm e}$ and the gate plus doping potential $V_{\rm g+d}$ are also shown. The first subband energy level is $\mathcal{E}_1 = -776.0$ meV (indicated by solid green line inside QW), i.e. 16.4 meV below the Fermi energy (not shown), which is pinned at -759.6 meV (i.e., the mid gap energy in bulk GaAs). The resulting carrier density is $n = 4.5 \cdot 10^{11}$cm^{-2}. Note that the origin of the abscissa is in the center of the well and the wafer surface is located slightly farther away than specified in the growth profile (see also Fig. 5.5) due to the lever arm measured in the experiment.

potential contributions (i)-(iv) above:

$$\alpha = \eta_{\rm w}\langle\partial_z V_{\rm w}\rangle + \eta_{\rm H}\langle\partial_z V_{\rm e}\rangle + \eta_{\rm H}\langle\partial_z V_{\rm g+d}\rangle, \tag{38}$$

with

$$\eta_{\rm w} = \frac{P^2}{3}\left(\frac{\delta_{\rm v}/\delta_{\rm c}}{E_g^2} - \frac{\delta_\Delta/\delta_{\rm c}}{(E_g+\Delta_{\rm w})^2}\right), \tag{39}$$

and

$$\eta_{\rm H} = -\frac{P^2}{3}\left(\frac{1}{E_g^2} - \frac{1}{(E_g+\Delta_{\rm w})^2}\right), \tag{40}$$

which involve the bulk quantities of the well layer, such as the band gap E_g and the usual Kane parameters Δ ("spin orbit") and P, in addition to the offsets $\delta_{\rm i}$, $i = {\rm c, v}, \Delta$ (see Fig. 5.10 and section E below for a discussion of these parameters). Even though $\alpha = \alpha_{\rm w} + \alpha_{\rm e} + \alpha_{\rm g+d}$ comprises seemingly independent contributions, we note that each of

these $\alpha_{\rm w}$, $\alpha_{\rm e}$, and $\alpha_{\rm g+d}$ does depend on all four potentials (i)-(iv) via the self-consistent wave function used in the expectation values. In particular, they all change as we vary the gates (top and back), which allows us to fine tune α and thus attain the $\alpha = \beta$ regime when the Dresselhaus term is considered.

We emphasize that the Rashba coefficient α can be rewritten in terms of an "external" electric field $E_{\rm ext} = E_{\rm gate} + E_{\rm d} + E_{\rm e}$, where we have defined $E_{\rm gate} = \frac{1}{e}\langle\partial_z V_{\rm g}\rangle$, $E_{\rm d} = \frac{1}{e}\langle\partial_z V_{\rm d}\rangle$, and $E_{\rm e} = \frac{1}{e}\langle\partial_z V_{\rm e}\rangle$ with $e > 0$ the elementary charge. Since the total force on a bound state is zero (Ehrenfest's theorem), *i.e.*, $\langle\partial_z V_{sc}\rangle = \langle\partial_z(V_{\rm w} + V_{\rm e} + V_{\rm g} + V_{\rm d})\rangle = 0$, one has the relation of α with $E_{\rm ext}$,

$$\alpha = (\eta_{\rm H} - \eta_{\rm w}) e E_{\rm ext}. \tag{41}$$

Now let us turn to the change of α due to a variation of $E_{\rm ext}$, i.e. a variation δV_T of the top gate voltage and/or a variation δV_B of the back gate voltage, giving $\delta\alpha = e(\eta_{\rm H} - \eta_{\rm w})(\delta E_{\rm gate} + \delta E_{\rm d} + \delta E_{\rm e})$. In our model, the variation $\delta E_{\rm d} \simeq 0$ since the doping potential does not vary with the gates. Furthermore, in the case of constant density (as shown in Figs. 1c and 3c of the paper), we also have $\delta E_{\rm e} \simeq 0$ since the rearrangement of the *quantum mechanical* distributions of electrons in the gate range we studied is negligible. Therefore, to keep the carrier density n unchanged when we tune the gates, we have $\delta\alpha \simeq e(\eta_{\rm H} - \eta_{\rm w})\delta E_{\rm gate}$. Note that in the main text of the paper (and in Figs. 1c and 3c), we use the notation of $\delta E_z = \delta E_{\rm gate}$ to describe the change of electric field along the growth direction due to the gates.

Dresselhaus spin-orbit couplings β_1 and β_3. The linear β_1 and cubic β_3 coefficients of the Dresselhaus well Hamiltonian arise from the expectation value of the bulk cubic Dresselhaus Hamiltonian [77]. Using our self-consistent electron wave functions, we obtain $\beta_1 = -\gamma\langle\partial_z^2\rangle$ and $\beta_3 = \gamma k_F^2/4$, where γ is the bulk Dresselhaus parameter and k_F the Fermi wave vector. To a very good approximation the Fermi contours are essentially circles and hence $k_F \simeq \sqrt{2\pi n}$, with n being the areal electron density, and

$\beta_3 \simeq \gamma\pi n/2$.

Input from the experiment Input for our simulations are mainly based on the experimental conditions:

1. The chemical potential is pinned at mid gap in GaAs ($= -759.60\,\mathrm{meV}$) [154].

2. The top gate voltage V_T and back gate voltage V_B enter the numerical calculation as boundary conditions when solving the Poisson's equation for $V_g(z)$, *i.e.*, $V_g(-d_T) = -eV_T$ and $V_g(d_B) = -eV_B$ with the coordinate origin being chosen as the center of the well, which amounts to a linear external gate potential $V_g(z) = -e\left[V_T + \frac{(V_B - V_T)}{d_B + d_T}(z + d_T)\right]$. The gate lever arms, *i.e.*, the d_T and d_B values, are taken from the experiment and are close to the nominal values from the wafer growth profile.

3. We model the delta-doping regions in our samples by considering monolayer-thick doped regions with an effective ionized areal doping density ρ^{eff} used in the simulation, distinct from the nominal doping ρ^{nom} specified in the MBE growth.

In the asymmetrically doped wafers, the effective doping density ρ^{eff} is chosen so that the areal electron density $n(V_T, V_B)$ in the QW matches the measured values for all gate voltages using the experimentally determined gate lever arms. We find a donor ionization efficiency $\rho^{\mathrm{eff}}/\rho^{\mathrm{nom}}$ of about 50% for all asymmetric wafers. We need to introduce the effective doping density ρ^{eff} because the simulation does not include effects such as partial absorption of donor electrons e.g. by positive background doping or DX centers, resulting in partial ($\sim 50\%$) rather than full ionization of donors.

In the more symmetrically doped wafer, in contrast to the asymmetric ones, we have two δ-doping layers: an upper layer above the QW with effective doping $\rho_{\mathrm{u}}^{\mathrm{eff}}$ and a lower layer below the QW with effective doping $\rho_{\mathrm{l}}^{\mathrm{eff}}$. The effective doping asymmetry ratio $r = \rho_{\mathrm{l}}^{\mathrm{eff}}/\rho_{\mathrm{u}}^{\mathrm{eff}}$ modifies the Rashba coefficient α by changing the electric field across the QW. In the experiment, we detect the $\alpha = \beta$ regime (absence of WAL), where

$\beta \propto \gamma$. Thus, r and with it the simulated α will directly affect the extracted γ. There is no reason to have a γ for the symmetrically doped QW that is different from the asymmetrically doped, but otherwise identical QW. Thus, we choose the doping asymmetry r by requiring the Dresselhaus parameter γ to take on the same value $\gamma = 11.6\,\mathrm{eV\AA}^3$ as for all the asymmetric wafers, while choosing $\rho_\mathrm{u}^\mathrm{eff}$ to maintain the measured charge density in the QW. Here, we obtain $\rho_\mathrm{u}^\mathrm{eff} \sim 0.61 \cdot \rho_\mathrm{u}^\mathrm{nom}$ and $r \sim 0.3$, i.e. about three times more doping from above compared to from below the QW.

We note that the QW electron density n is significantly smaller than the total effective ionized doping $\rho^\mathrm{eff} = \rho_\mathrm{u}^\mathrm{eff} + \rho_\mathrm{l}^\mathrm{eff}$, e.g. $n \sim 5 \cdot 10^{11}\,\mathrm{cm}^{-2}$ versus $\rho^\mathrm{eff} \sim 15 \cdot 10^{11}\,\mathrm{cm}^{-2}$. Due to the close proximity of the QW to the surface and to the interface with the LT GaAs barrier, a large fraction of the ionized donor electrons will populate surface and interface states, rather than the QW. This results in strong band bending at the surface and LT interface, lowering the QW energy below the chemical potential and allowing population of the QW with electrons.

Gate voltages and contours of constant density We will now describe the effect of the gate voltages in a quantum mechanical model and compare the results to a simple classical plate capacitor model.

Quantum mechanical description We treat the variation $\delta V_g^T(z)$ due to a change of top gate voltage δV_T and the variation $\delta V_g^B(z)$ due to a change of back gate voltage δV_B as a perturbation and obtain the first order correction to the lowest subband energy, $\delta\mathcal{E}_1 = \delta\mathcal{E}_1^T + \delta\mathcal{E}_1^B$ with

$$\delta\mathcal{E}_1^T = \langle\psi^0|\delta V_g^T(z)|\psi^0\rangle = -e\frac{d_B - \langle\psi^0|z|\psi^0\rangle}{d_B + d_T}\delta V_T, \tag{42}$$

and

$$\delta\mathcal{E}_1^B = \langle\psi^0|\delta V_g^B(z)|\psi^0\rangle = -e\frac{d_T + \langle\psi^0|z|\psi^0\rangle}{d_B + d_T}\delta V_B, \tag{43}$$

where ψ^0 is the envelope function in absence of $\delta V_g^T(z)$ and $\delta V_g^B(z)$, and d_T (d_B) the top (back) gate lever arms. Notice that in all our wafers the well width $W \ll d_T(d_B)$, which ensures $\langle\psi^0|z|\psi^0\rangle \ll d_T(d_B)$ since ψ^0 is mostly confined in the well (if ψ^0 is symmetric with respect to the center of the well, i.e., in a symmetric wafer, $\langle\psi^0|z|\psi^0\rangle$ is always zero). Therefore we have

$$\delta\mathcal{E}_1^T \simeq -e\frac{d_B}{d_B+d_T}\delta V_T, \qquad \delta\mathcal{E}_1^B \simeq -e\frac{d_T}{d_B+d_T}\delta V_B. \tag{44}$$

The resulting change of carrier density δn can be straightforwardly written as

$$\delta n = -\frac{m^*}{\pi\hbar^2}(\delta\mathcal{E}_1^T + \delta\mathcal{E}_1^B) = \frac{m^*}{\pi\hbar^2}e\left(\frac{d_B}{d_B+d_T}\delta V_T + \frac{d_T}{d_B+d_T}\delta V_B\right). \tag{45}$$

Note that this change of density is only considering the response to a change of gate voltages and is neglecting the resulting change of the self-consistent Hartree potential. When the self-consistent Hartree potential is also included, the resulting gate lever arm is identical to the lever arm obtained in the plate capacitor model (see below) and reproduces the experimentally measured density changes very well. On a contour of constant density, the Hartree potential is essentially constant in the voltage range considered here, and thus drops out. From equation 8, a constant density results for $\delta V_T/d_T = -\delta V_B/d_B$. Furthermore, the change of electric field for constant density is

$$\delta E_z = \frac{\delta V_T - \delta V_B}{d_T+d_B} = \frac{\delta V_T + \delta V_T\frac{d_B}{d_T}}{d_T+d_B} = \frac{\delta V_T}{d_T}\frac{d_T+d_B}{d_T+d_B} = \frac{\delta V_T}{d_T} = -\frac{\delta V_B}{d_B}. \tag{46}$$

Classical plate capacitor model Based on a simple plate capacitor model, a variation of top gate δV_T and back gate δV_B induces a change of carrier density δn^T and δn^B, respectively,

$$\delta n^T = \frac{\epsilon\epsilon_0}{e}\frac{\delta V_T}{d_T}, \qquad \delta n^B = \frac{\epsilon\epsilon_0}{e}\frac{\delta V_B}{d_B}, \tag{47}$$

which also agrees very well with the measured gate effect. To ensure a constant density when varying the top and back gates, i.e., $\delta n^T + \delta n^B = 0$, we obtain, $\delta V_T/d_T =$

$-\delta V_B/d_B$, identical to the expression from the quantum mechanical description. Furthermore, the change of average electric field on the left and right of the 2DEG plate is $\delta E_z = 1/2(\delta V_T/d_T - \delta V_B/d_B)$. On a contour of constant density, this again becomes $\delta E_z = \delta V_T/d_T = -\delta V_B/d_B$, as before in the quantum description. For simplicity, we use $\delta E_z = 1/2(V_T/d_T - V_B/d_B)$, i.e. using the actual applied gate voltages, rather than only changes of voltages, as a practical choice of the origin of E_z, e.g. for Figure 5.1c and Figure 5.3c.

Estimate of the error bars in the Rashba coupling due to the uncertainties in input parameters The Rashba coupling strength α is more sensitive to the band parameters, especially to the band offsets of the quantum well (see expression for α above), than the Dresselhaus β_1, which in our phenomenological description solely depends on the well confinement via the wave function. Therefore, to extract a reliable γ based on the condition $\alpha = \beta$ (locked $\alpha = \beta$ regime or absence of WAL), it is essential to assess how sensitive the Rashba coupling is to the band parameters.

A sketch of the conduction and valence-band offsets for our GaAs/$Al_{0.3}Ga_{0.7}$As quantum well is shown in Fig. 5.10, where the relevant bulk parameters are indicated. The commonly accepted band gap in GaAs at low temperature is 1.519 eV [61, 155–158], and the band gap in $Al_{0.3}Ga_{0.7}$As is 1.951 ± 0.006 eV [156]. The main offsets of a GaAs/$Al_{0.3}Ga_{0.7}$A quantum well, δ_c (electrons) and δ_v (heavy and light holes), are taken from literature with uncertainties of about 2% [156]. We obtain the split-off hole offset δ_Δ straightforwardly through the relation, $\delta_\Delta = \delta_v + \Delta_b - \Delta_w$ with Δ_w (Δ_b) the split-off gap in the well (barrier), see Fig. 5.10 and Table 1. The split-off gap Δ_b of the barrier is obtained from linear interpolation of the GaAs and AlAs values [157]. From the uncertainties in δ_v, Δ_b and Δ_w, one can evaluate the error bar of δ_Δ [159].

Another crucial quantity determining the Rashba α is the Kane parameter P (see eq. 1-3), usually expressed via the quantity $E_P = 2m_0P^2/\hbar^2$ (see e.g. Ref. [157]), with m_0 the bare electron mass. We take E_P for GaAs from the widely accepted values

quoted by Hermann and Weisbuch [160] (see also [157]), who extracted this parameter via a detailed fitting procedure involving both the effective mass and the g factor. In their fitting, an error of effective mass and g factor less than 1% has been assumed. As pointed out by Vurgaftman *et al.* in their classic review Ref. [157], other estimates of E_P with smaller errors seem to have internal inconsistencies. The band parameters and Kane parameter E_P used in the simulations and their corresponding errors are summarized in Table 1.

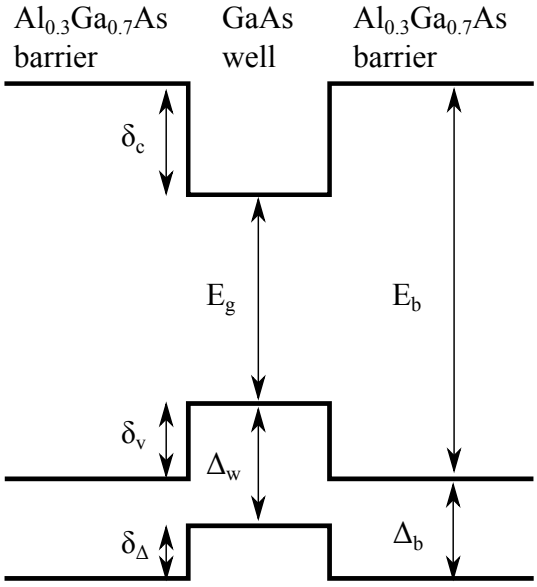

Figure 5.10: Schematic of the band offsets for GaAs/AlGaAs well. E_g (E_b) and Δ_w (Δ_b) are the fundamental band gap and the split-off gap in the well (barrier), respectively. δ_i ($i = c, v, \Delta$) denote the corresponding band offsets: δ_c for conduction band, δ_v for heavy hole (and light hole) , and δ_Δ for split-off hole.

Table 1: Main relevant parameters for the Rashba coupling. The unit is in eV

	Δ_b(AlAs)	Δ_w(GaAs)	Δ_b($Al_{0.3}Ga_{0.7}As$)
Value	0.30[a,e] (0.28[c])	0.341[a–f] (0.340[h])	0.329[c]
Error	0.02 (6.7%)	0.001 (0.3%)	0.007 (2%)

	δ_c	δ_v	δ_Δ	E_P
Value	0.261[b]	0.171[b]	0.159[f]	28.9[c,g]
Error	0.003 (1.2%)[b]	0.003 (1.8%)[b]	0.01 (6.3%)[f]	0.9 (3.1%)[c,g]

[a]Ref. [155], [b]Ref. [156], [c]Ref. [157],[d]Ref. [158], [e]Ref. [61], [f]Ref. [159], [g]Ref. [160], and [h]Ref. [161].

With all these parameters and the corresponding errors at hand, we can now evaluate the Rashba coefficient α and its uncertainty. The α coefficient for our 9.3 nm well as a function of back gate is shown in Fig. 5.11, where we vary both the top and back gates so that the curve follows a constant density, $n = 4.5 \cdot 10^{11}\,\mathrm{cm}^{-2}$. The α plotted here actually corresponds to the one shown in Fig. 5.1c (red solid curve). The error bar of α for several values of the back gate is also shown in Fig. 5.11.

The resulting error of α is found to be $\sim 8\%$, with two dominating contributions, $\sim 4\%$ from the uncertainty of the band parameters and $\sim 3\%$ from the Kane parameter P. The remaining $\sim 1\%$ error of α arises from the uncertainty of the measured carrier density, the effective lever arms, and the resulting uncertainty of the doping efficiency ($\rho^{\mathrm{eff}}/\rho^{\mathrm{nom}}$). This error analysis holds for all wafers used in this study. Note that to determine γ (Fig. 5.2c), we use the error bars arising from experimental uncertainty ($1-2\%$) only, not taking into account the 13 nm wafer data due to its significantly larger error bar (using three data points from the 8, 9.3 and 11 nm wafers in Fig. 5.2c). We then add the larger systematic error, resulting in a total error on γ of about $9-10\%$ or $\pm 1\mathrm{eV\AA}^3$. We note that finally, the γ extracted from the 13 nm wafer is also consistent with this γ-value.

5.6.4 Effective Spin-Orbit Magnetic Field

In the rotated coordinate system $\hat{x}_+||(110)$, $\hat{x}_-||(1\bar{1}0)$, and $\hat{z}$, the Rashba and linear Dresselhaus terms for a 001-grown GaAs well becomes

$$\mathcal{H}_{\mathrm{SO}}^{(1)} = (\alpha - \beta_1)k_-\sigma_+ - (\alpha + \beta_1)k_+\sigma_-, \tag{48}$$

while the cubic term

$$\mathcal{H}_{\mathrm{SO}}^{(3)} = \frac{2\beta_3}{k^2}(k_+^2 - k_-^2)(k_-\sigma_+ - k_+\sigma_-). \tag{49}$$

It is convenient (e.g., for the D'Yakonov-Perel' mechanism) to reexpress the spin-orbit

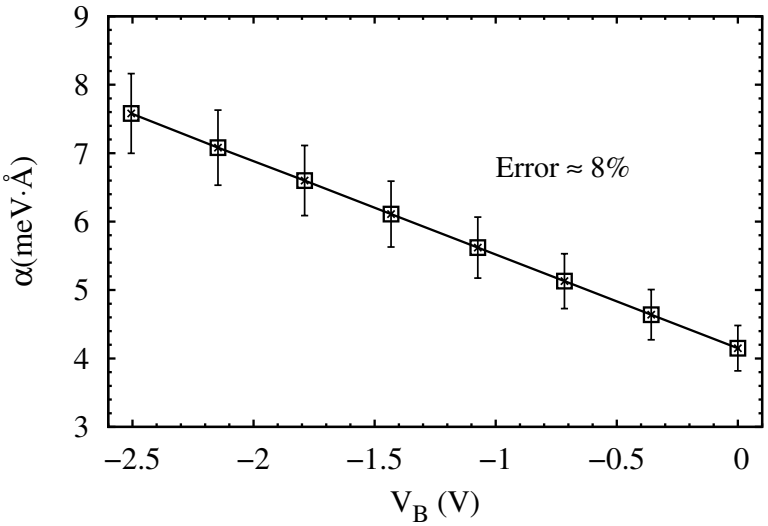

Figure 5.11: Error bar on the calculated Rashba coefficient α. Rashba coupling strength α as a function of V_B on a contour of constant density $n = 4.5 \cdot 10^{11}\,\mathrm{cm}^{-2}$ for the 9.3 nm QW and corresponds to the α curve (the red solid curve) in Fig. 5.1c. The error bar due to the uncertainty in input parameters for several values of back gate is also shown. The error is about 8%.

Hamiltonian $\mathcal{H}_{\mathrm{SO}}$ in terms of an effective magnetic field $\mathbf{B}_{\mathrm{int}}(\mathbf{k})$

$$\mathcal{H}_{\mathrm{SO}} = \frac{1}{2} g\mu_{\mathrm{B}} \mathbf{B}_{\mathrm{int}}(\mathbf{k}) \cdot \sigma, \tag{50}$$

with g the electron g-factor in the QW, μ_B the Bohr magneton and,

$$\mathbf{B}_{\mathrm{int}}(\mathbf{k}) = \mathbf{B}^{(1)}_{\mathrm{int}}(\mathbf{k}) + \mathbf{B}^{(3)}_{\mathrm{int}}(\mathbf{k}), \tag{51}$$

and

$$\mathbf{B}^{(1)}_{\mathrm{int}}(\mathbf{k}) = \frac{2}{g\mu_{\mathrm{B}}} k_F \left[(\alpha - \beta)\sin(\theta)\hat{x}_+ - (\alpha + \beta)\cos(\theta)\hat{x}_- \right], \tag{52}$$

and

$$\mathbf{B}^{(3)}_{\mathrm{int}}(\mathbf{k}) = \frac{2}{g\mu_{\mathrm{B}}} k_F \left[\beta_3 \sin(3\theta)\hat{x}_+ - \beta_3 \cos(3\theta)\hat{x}_- \right], \tag{53}$$

where $\mathbf{B}^{(1)}_{\mathrm{int}}(\mathbf{k})$ and $\mathbf{B}^{(3)}_{\mathrm{int}}(\mathbf{k})$ are the first ($\cos(\theta) = k_+/k$) and third ($\cos(3\theta) = 4k_+^3/k^3 - 3k_+/k$) harmonics, respectively [103, 162], and θ denotes the angle between $\mathbf{k}$ and x_+ axis. Note that here $\beta = \beta_1 - \beta_3$ implying that part of the cubic Dresselhaus term

($\mathcal{H}^{(3)}_{\mathrm{SO}}$) renormalizes the linear parameter β_1 thus altering the condition for attaining the regime of matched SO strength (or absence of WAL) from $\alpha = \beta_1$ to $\alpha = \beta$. The remaining part of the cubic term (third harmonic) breaks the spin symmetry and is detrimental to the protection from relaxation.

5.6.5 Diffusive Spin-Orbit Time and Length

We determine the theoretical spin relaxation time τ_{eff} via the D'Yakonov-Perel' (DP) spin dephasing mechanism: as an electron performs a two-dimensional random walk in real space due to momentum scattering, it precesses about the momentum-dependent spin-orbit field $\mathbf{B}_{\mathrm{int}}(\mathbf{k})$, whose direction is randomly changing as well, thus accruing random precessional phases and spin dephasing after many scattering events in a time τ_{DP}.

Let $r_{x_i} = \sum_{j=1}^{N} \delta^j_{x_i}$ be the x_i component of the electron position vector on the (x_-, x_+) plane after a total of N scattering events whose jth displacement along the corresponding direction we denote by $\delta^j_{x_i}$. As usual in random walks [163], $\langle r_{x_i}\rangle_t = 0 = \langle \delta^j_{x_i}\rangle_t$ and its variance $\sigma^2_{x_i} = \langle r^2_{x_i}\rangle_t = N\langle(\delta^j_{x_i})^2\rangle_t$. Here $\langle ...\rangle_t$ denotes a time average over the survival probability $P(t) = \exp(-t/\tau_p)$, with τ_p being the momentum scattering time. Here, $P(t)$ is the probability of surviving a time t without suffering a collision (momentum scattering). The individual mean square displacement $\langle(\delta^j_{x_i})^2\rangle_t = \langle(v_{x_i}t)^2\rangle_t$ is independent of j and equals to $\langle(\delta^j_{x_i})^2\rangle_t = v_F^2\tau_p^2$, where we have used $\langle v^2_{x_i}\rangle_t = v_F^2/2$ and $\langle t^2\rangle_t = 2\tau_p^2$. Since $N = \tau_{\mathrm{DP}}/\tau_p$, we find $\sigma^2_{x_i} = (\tau_{\mathrm{DP}}/\tau_p)v_F^2\tau_p^2 = \tau_{\mathrm{DP}}l^2/\tau_p = 2D\tau_{\mathrm{DP}}$, where $l = v_F\tau_p$ is the electron mean free path and $D = l^2/2\tau_p$. We now define the spin diffusion lengths along x_- and x_+ via $\lambda^2_{\mathrm{DP},-} = \sigma^2_{x_-} = 2D\tau_{\mathrm{DP}}$ and $\lambda^2_{\mathrm{DP},+} = \sigma^2_{x_+} = 2D\tau_{\mathrm{DP}}$, respectively. Since $\lambda_{\mathrm{DP},+} = \lambda_{\mathrm{DP},-} = \lambda_{\mathrm{DP}}$, the direction of the diffusion is isotropic and the product $\lambda_{\mathrm{DP},-}\lambda_{\mathrm{DP},+} = \lambda^2_{\mathrm{DP}} = 2D\tau_{\mathrm{DP}}$ gives the characteristic loop area A of a closed trajectory. Thus we obtain $\lambda_{\mathrm{DP}} = \sqrt{2D\tau_{\mathrm{DP}}}$ for the conversion between spin relaxation time and spin diffusion length. As already shown in the main text and methods, using an Aharonov-Bohm phase of $\Delta\varphi = 1$ from the flux through A, we can convert the

experimental B_{SO} to a SO length $\lambda_{\mathrm{SO}} = \sqrt{\hbar/2eB_{\mathrm{SO}}}$, which we can further convert to a SO time $\tau_{\mathrm{SO}} = \lambda_{\mathrm{SO}}^2/(2D)$.

For a degenerate 2DEG, the individual spin relaxation rates $\tau_{\mathrm{DP,i}}$, with $i = +, -, z$ for spins polarized along $\hat{x}_+$, $\hat{x}_-$, and $\hat{z}$, can be described by [164]

$$\frac{1}{\tau_{\mathrm{DP},\pm}} = \frac{2\tau_1 k_F^2}{\hbar^2}\left[(\alpha \pm \beta)^2 + \frac{\tau_3}{\tau_1}\beta_3^2\right], \tag{54}$$

$$\frac{1}{\tau_{\mathrm{DP,z}}} = \frac{4\tau_1 k_F^2}{\hbar^2}\left[\alpha^2 + \beta^2 + \frac{\tau_3}{\tau_1}\beta_3^2\right]. \tag{55}$$

Here, τ_1 is the transport scattering time τ_p and we assume $\tau_1 \geq \tau_3$, where τ_3 is the third moment of the momentum relaxation time [164]. For dominant small angle scattering, one obtains $\tau_1 = 9\tau_3$.

We remark that the ballistic spin precession length $\lambda_\pm$ and the spin diffusion length defined by $\sqrt{2D\tau_{\mathrm{DP},\pm}}$ via the DP process are equivalent. The formulation of the ballistic $\lambda_\pm$ did not include third harmonic effects. Thus, when setting to zero the third harmonic term and converting $\tau_{\mathrm{DP},\pm}$ to a length using $\sqrt{2D\tau_{\mathrm{DP},\pm}}$, one obtains the ballistic $\lambda_\pm$ (up to a factor of order one). The diffusion constant D cancels here in the conversion from time to length. Hence, the diffusive spin relaxation length and the ballistic spin precession lengths are equivalent.

Note that equations 54 and 55 describe the relaxation of polarized spins, e.g. optically excited spins. In contrast, there is a negligible spin polarization in our transport experiment, therefore we define an effective τ_{eff} for a random spin, by taking the average of the spin lifetimes

$$\tau_{\mathrm{eff}} = \frac{1}{3}\left(\tau_{\mathrm{DP},+} + \tau_{\mathrm{DP},-} + \tau_{\mathrm{DP,z}}\right). \tag{56}$$

Note that we average the spin relaxation times here, not the spin relaxation rates. This is because we have three independent, equally populated spin components that are each relaxing through their own, separate channel, in contrast to a single spin species that can relax through three different channels. Note that this also correctly results in a

diverging τ_{eff} for $\alpha = \pm\beta$ in case of negligible β_3. With this at hand, an effective diffusive SO length $\lambda_{\text{eff}} = \sqrt{2D\tau_{\text{eff}}}$ can be defined, reading

$$\lambda_{\text{eff}} = \frac{\hbar^2}{\sqrt{6}m^\star}\sqrt{\left[(\alpha-\beta)^2+\frac{\tau_3}{\tau_1}\beta_3^2\right]^{-1}+\left[(\alpha+\beta)^2+\frac{\tau_3}{\tau_1}\beta_3^2\right]^{-1}+\frac{1}{2}\left[\alpha^2+\beta^2+\frac{\tau_3}{\tau_1}\beta_3^2\right]^{-1}} \tag{57}$$

Equivalently, this average spin diffusion length can be defined from the variance $\bar{\sigma}^2_{x_i} = (\sigma^2_{x_i,s_{x_-}} + \sigma^2_{x_i,s_{x_+}} + \sigma^2_{x_i,s_z})/3$, $i = +,-$, obtained by averaging over the initial spin directions. At $\alpha = \pm\beta$ and small β_3 (and/or $\tau_3 \ll \tau_1$) the SO length λ_{eff} diverges, as explained in the main text. We fit our data points using equation 57 and the ratio τ_3/τ_1 as a free parameter, as shown in Figure 5.12. The resulting ratio $\tau_3/\tau_1 \lesssim 0.2$ (0.4) for $n = 6 \cdot 10^{11}\,\text{cm}^{-2}$ ($9 \cdot 10^{11}\,\text{cm}^{-2}$) can be explained by small angle scattering, originating from the long range potential of the remote donors.

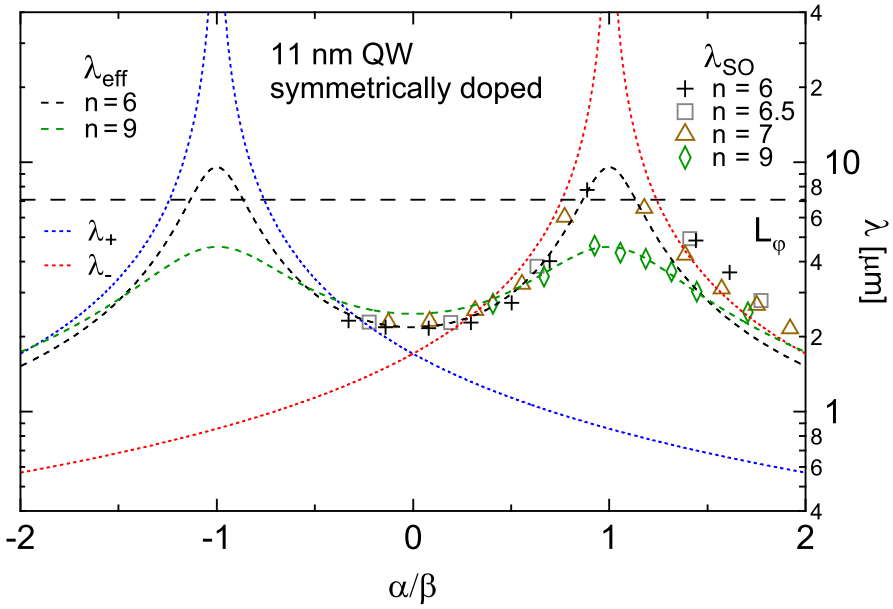

Figure 5.12: Theoretical and experimental SO lengths including symmetry breaking. In contrast to the ballistic $\lambda_\pm$ (dotted red and blue), the diffusive λ_{eff} (dashed black and green, fits to λ_{SO} data points) includes the symmetry breaking higher harmonic term and does not diverge at $\alpha = \pm\beta$. The highest density $n = 9 \cdot 10^{11}\,\text{cm}^{-2}$ (green markers) shows the strongest symmetry breaking effect, where WAL remains visible through $\alpha = \pm\beta$, thus allowing extraction of $\lambda_{\text{SO}} < L_\varphi$ at $\alpha = \beta$.

6 Conclusion and Outlook

6.1 Hybrid 2DEGs

Motivated by the idea of combining and coupling InAs SAQDs to gate defined lateral quantum dots on a single device, we investigated the influence of SAQDs on the transport properties of a proximal 2DEG. A key role for the vast majority of quantum transport experiments in 2DEGs is played by its quality. Scattering induced by the Coulomb potential of the InAs SAQDs or even an extension of the 2DEG wave function into the QD layer has previously led to low electron mobility in comparable hybrid heterostructures [109]. The systematically optimized and very controlled MBE-growth of the inverted hybrid heterostructures studied in this work, results in 2DEGs exhibiting a substantial gain in quality, with mobilities up to $800'000\,\mathrm{cm}^2/(\mathrm{Vs})$.

Due to a gradient in SAQD density across the wafers and variations in the barrier width between SAQDs and 2DEG, the scattering could be studied in different regimes. Measurements clearly show, that a considerable reduction of the mobility is induced by a proximal InAs wetting layer alone (in absence of SAQDs), but the potential of the SAQDs adds additional scattering. The most critical parameter with regards to the mobility (and therefore also the mean free path) is the tunnel barrier width. To reach decent values for ballistic experiments ($\sim 500'000\,\mathrm{cm}^2/(\mathrm{Vs})$) and at the same time maintain electron tunneling between the systems, a tunnel barrier between 40 and 50 nm seems a good choice, also with the perspective of the quantum optical interface [25].

In spite of the mean free path being much larger than the QPC constriction, no conductance quantization was observed on the 45 nm tunnel barrier hybrid 2DEG, independent of SAQD formation/density. Fluctuations in the potential either from InAs wetting layer or Si-donors in the remote doping layer induce disorder and thus scattering in the 1D channel. Further, electrostatic gating is suffering from hysteresis. Solving these

problems on the material level is important in order to enable experiments with more complex gate defined structures, such as lateral quantum dots. Ideas for improvement include an increase of the 2DEG density by increasing the 2DEG depth or by adding more Si to the δ-doping layer. Both approaches have drawbacks and limitations such as the requirement of larger negative gate voltages for 2DEG depletion, reduced AFM surface detection sensitivity and a possible increase of Si migration. Extending the set back (distance between 2DEG and Si) on the other hand, reduces the remote donor scattering and the Si migration but at the same time also the density.

On an experimental level, the excitation of a persistent photocurrent by LED illumination offers a more simple way to increase the number of electrons in the 2DEG. In presence of surface gates however, this method may lead to increased gate leakage and a non-uniform density distribution. Concerning the lack of quantization in the QPC data of our experiments (Chapter 4), we cannot completely exclude a non-ideal QPC geometry, e.g. a confinement potential with very low subband spacing. Here, additional measurements including magnetic fields, different QPC geometries or alternative fabrication approaches like etch-defined constrictions could shed more light on the topic.

From the point of view of fabrication, the precise positioning of nanostructures near a SAQD has proven to be challenging but feasible. Choosing the right areal density of SAQDs from a gradient induced by a wafer rotation stop during InAs growth even allows to specifically select a single InAs QD. The localization precision of the optical method of μ-PL with sub-μm resolution is excelled by the surface mapping method using an AFM. This detection method however needs an ultra-clean surface, which we achieved to maintain despite the well known resist residue problems of standard nano-lithography methods.

Altogether, the improved quality of inverted hybrid 2DEG structures and the precise alignment of lateral gate nanostructures indeed goes into the right direction. For the implementation of a quantum optical interface, there are however additional fundamen-

tal barriers to break down. One of them is certainly a sensitive probe, demonstrating the tunnel coupling of single SAQDs to the 2DEG, which in a next step should happen in a very controlled way. Also, for using such a coupled device as a photon source and not only as a detector, one has to think about how to controllably feed holes into a single SAQD to enable recombination processes.

6.2 Control of SOI

In our experiment, we achieve a remarkably high level of control of all the relevant SO fields. The in-situ control using a top *and* a back gate allows broad tunability of α, independent of the electron density in the QW. While the linear Dresselhaus contribution can only be accessed via the quantum well width, we can tune the strength of the cubic term by changing the density and hence also by an external electric field. Using these degrees of freedom, we demonstrate a dynamically locking of the SO fields at equal strength ($\alpha = \beta = \beta_1 - \beta_3$) over a wide range of gate voltages for the first time.

In this regime, the spin is expected to be immune against D'Yakonov-Perel' spin relaxation, usually present in diffusive transport. Indeed, we observe a strongly enhanced spin lifetime, which we extract from the width of the WAL. The experimental SO times are in very good agreement with an effective spin relaxation time τ_{eff}, derived by simply averaging the highly anisotropic D'Yakonov-Perel' spin relaxation times. Around $\alpha \approx \beta$ this effective SO time (and hence the effective SO length) coincides with the longer ballistic SO time (and length) and diverges in absence of symmetry breaking by the cubic Dresselhaus term. In spite of the quasi-ballistic behavior of spin relaxation in otherwise diffusive transport, the conformity of two physically different quantities comes rather surprising and is lacking a proper interpretation.

Although the quantum corrections to magnetoconductance prove to be a sensitive probe of SOI, there are two aspects that need further attention in future experiments and theory. First, the measurement sensitivity near $\alpha = \beta$ is limited by coherence. The

rather broad transition from WAL to pure WL and back to WAL as a function of α can possibly be sharpened by an increase in coherence. Experimentally, this is possible by lowering the electron temperature and hence decreasing the electron-electron dephasing rate $1/\tau_{ee} \propto T^2 \ln(1/T)$ and quasi-elastic Nyquist scattering rate $1/\tau_{e-e} \propto T$ [151]. A reduction of other, T-independent intrinsic dephasing sources [165] needs further study, possibly leading to improvements on the material side. Secondly, a closed-form expression for the extraction of the SO parameters from magnetoconductance data is lacking. It would allow a direct and independent access to the Rashba and Dresselhaus coefficients and thus also answer open questions, like e.g. the role of the confinement on γ, for which we find a single value ($\gamma = 11.6 \pm 1\, eV\text{Å}^3$) for all QWs, in contradiction to the dependence on QW width reported elsewhere [80].

With the demonstrated universal control of SO interaction we have access to the length of the spin rotation as required for the implementation of the active area of a non-ballistic spin FET (purple area in Fig. 1.2) while maintaining $\alpha = \beta$ and thus protection from spin relaxation. For progress towards a technologically interesting spintronic device, the focus now has also to be laid on spin injection and detection, which in GaAs 2DEGs is difficult to achieve. Additional to the possible technological applications, SO coupling and its control are of great importance with respect to effects in quantum wires or quantum dots. Preliminary results show, that lateral gating to a 1D confinement in principle is possible on the QWs discussed in this work, paving the way for new such experiments. The direct access to the relevant SO terms in open QDs for example could enable a thorough study of the influence of the confinement potential or complement previous work, such as experiments with in-plane magnetic field [166, 167]. Further, the well defined anisotropy of the SO-induced spin splitting at $\alpha = \pm\beta$, with maximal splitting along one crystal axis and absence of the SO field along the perpendicular direction is an interesting situation. Electric-dipole induced spin resonance for example is predicted to exhibit an enhanced spin susceptibility at $\alpha = \beta$ [67] and will depend strongly on the direction of the ac E-field. In [100] GaAs 2DEGs, these axes are easy

to identify because they coincide with the crystallographic cleaving axes.

More experiments are also triggered on the material side. A reduction of the (slow) random telegraph noise and disorder in the potential affecting QPC measurements in our current material [168] is preferable for measurements on laterally confined structures. Further, applying our control and understanding of SOI to other 2DEGs (e.g. [011] or [111] grown QWs, different materials,...) or even double QW structures, where the subband fields combine to a crossed persistent spin helix pattern [169], new aspects of spin relaxation and coherent spin control can be explored. On a more fundamental level, SO coupling - and therefore also its control - plays a key role in topics such as Majorana fermions, topological insulators and other effects, currently generating a lot of interest among theorists and experimentalists.

Appendices

Appendix A Material Overview

A.1 Hybrid Wafers

wafer	sample name	tunnel barrier width [nm]	InAs growth temp. [°C]	mesa etch depth [nm]	SAQD density
D090626A	Pinto 38 OT	45	518	305	no
D090626A	Pinto 38 HD	45	518	460	high
D090626B	Pinto 39 LD	30	518	465	no
D090626B	Pinto 39 HD	30	518	470	high
D090626C	Pinto 40 LD	15	517	470	no
D090626C	Pinto 40 HD	15	517	455	high
D090719A	Pinto 42 OT	45	534	295	no
D090719A	Pinto 42 HD	45	534	305	high
D090719A	Pinto 42 QPC 10-13	45	534	295	low
D090719A	Pinto 42 QPC 20-23	45	534	305	low
D090719A	Pinto 42 QPC 30-33	45	534	295	no
D090719A	Pinto 42 QPC 40-43	45	534	305	no
D090719B	Pinto 43 LD	15	533	300	no
D090719B	Pinto 43 HD	15	533	300	high
D090918B	Pinto 60 LD	60	533	290	no
D090918B	Pinto 60 HD	60	533	295	high

This material was grown at the University of Regensburg in collaboration with Antonio Badolato and the group of Werner Wegscheider.

A.2 Quantum Well Wafers

wafer	sample name	quantum well width [nm]	doping density [$\times 10^{11} cm^{-2}$]	
			top	bottom
120601C	α=β01C_11_bg_LTB	11	28	-
120619A	α=β19A_8	8	28	-
120619B	α=β18B_9.3	9.3	28	-
120621A	α=β21A_13	13	28	-
120630A	α=β30A_11sym2	11	20	4

These wafers were designed and grown in collaboration with Shawn Mack and David D. Awschalom at the University of California, Santa Barbara.

Appendix B Optical Data

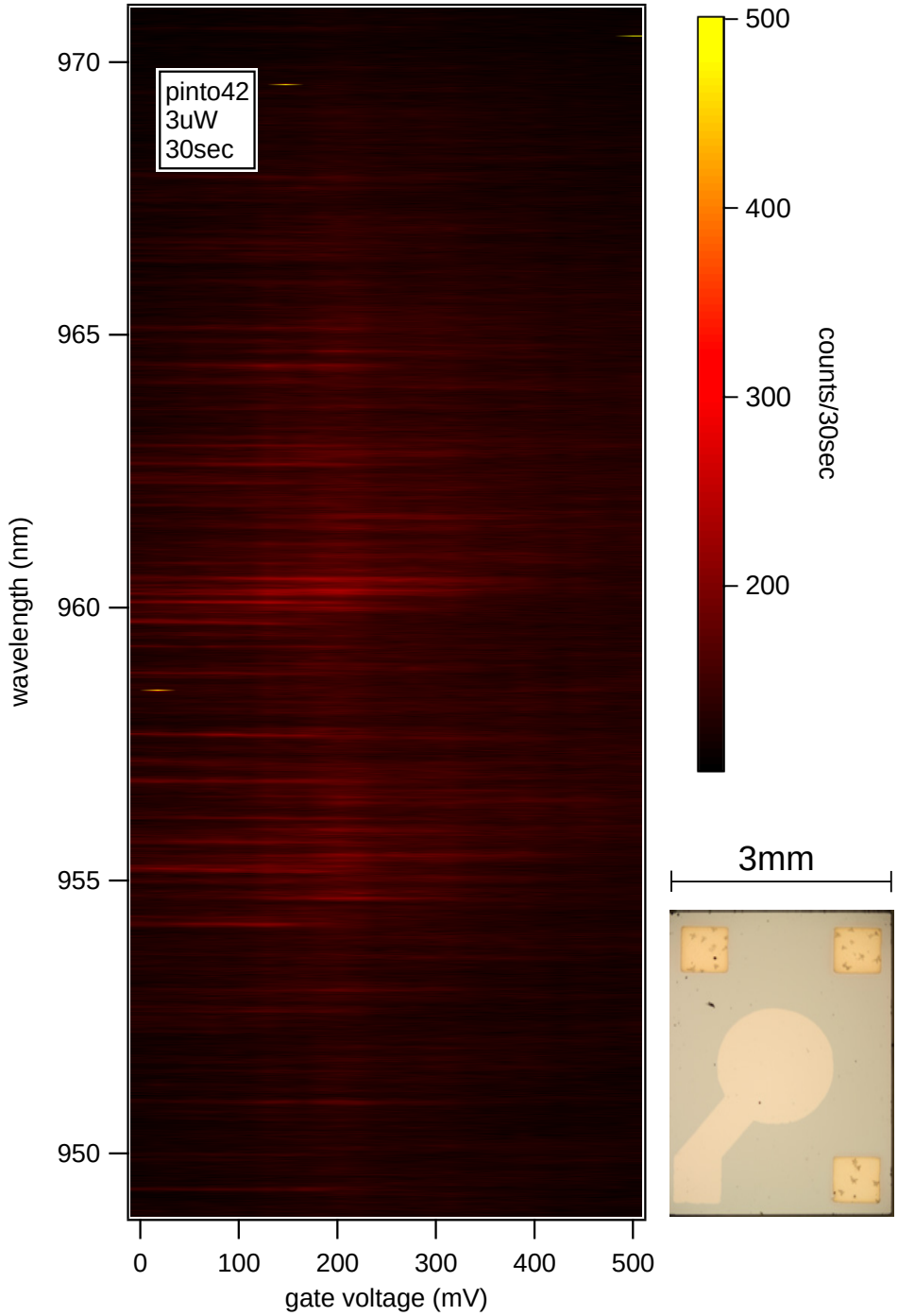

Figure B.1: PL data of a low SAQD density sample of the D090719A (45 nm tunnel barrier) wafer, as used for the single QD experiments in Chapter 4. The gate voltage (abscissa) is applied to the large, transparent Ti/Au top gate, see photo of sample on the right. Red lines correspond to electron-hole recombinations of single SAQDs, emitting around 960 nm.

Appendix C Fabrication Details

C.1 Hybrid Wafers

Hall Bar Fabrication

- **Clean Ga on the back of the wafer:**
  - rinse in IPA[1] and blow off
  - pre-bake at 120 °C for 5 min, let the sample cool to room temperature (RT)
  - spin photoresist *ma-N 415*[2] at 4000 rpm for 40 s, 4 s rise time
  - bake at 93 °C for 90 s
  - dip into HCl for 30 s, followed by DI[3] H_2O for 30 s, repeat until all the Ga has gone (no bubbling, $\sim 5\times$ or more)
  - remove unexposed photoresist with developer *ma-D 377XP*[2] for 5 min in ultrasound
  - wash in DI for 5 min and rinse in IPA, blow off
- **Mesa etch:**
  - 3-solvent-clean: sonication in TCE[4], acetone and methanol for 5 min (each), blow off
  - pre-bake at 120 °C for 5 min, let the sample cool to RT
  - spin photoresist *ma-N 415* at 6000 rpm for 40 s, 6 s rise time ($\sim 1.3\,\mu$m)
  - bake at 93 °C for 90 s, let the sample cool to RT
  - expose mesa pattern for 6 s (*MJB4*, channel II, hard contact 2 s)
  - develop in *ma-D 332S*[2] for ~ 100 s, rinse in DI H_2O for 10 s
  - check under microscope and add development time if necessary
  - measure resist height with α-stepper
  - prepare an etch solution with ratio 1:8:240 H_2SO_4:H_2O_2:H_2O
  - measure etch rate by etching a test sample, etch rate $\sim 2-3$ nm/s
  - etch 460 nm, rinse in DI H_2O, check with α-stepper and etch more, if needed
  - wash photoresist with remover *mr-Rem 660*[2] or NMP[5] (3 min ultrasound) and rinse in IPA, blow off
  - re-check with α-stepper
- **Ohmic contacts:**

[1] isopropyl alcohol
[2] from microresist technology GmbH, Germany
[3] de-ionized
[4] trichloroethylene
[5] N-methyl-2-pyrrolidone

- 3-solvent-clean
- pre-bake at 120 °C for 5 min, let the sample cool to RT
- spin photoresist *ma-N 415* at 6000 rpm for 40 s, 6 s rise time ($\sim 1.3\,\mu$m)
- bake at 93 °C for 90 s, let the sample cool to RT
- align and expose Ohmic pattern for 6 s (*MJB4*, channel II, hard contact 2 s)
- develop in *ma-D 377XP* for $\sim 3-5$ min, rinse in DI H_2O for 10 s
- check under microscope for good undercut and add development time if necessary
- oxygen plasma etch: 16 %, 250 mTorr, 30 W for 40 s
- prepare evaporator
- dip into HCl for 3 s, rinse in DI H_2O, glue onto evaporation plate with PMMA glue and pump down evaporator, do this within a short period of time (< 5 min)
- evaporate Au/Ge/Au/Ge/Pt 120 nm/60 nm/120 nm/60 nm/85 nm
- lift-off in warm (45 °C) remover *mr-Rem 660* or NMP for $30-60$ min, rinse in IPA, blow off
- thermal annealing (old annealing oven *AZ500*):

step #	T [°C]	time [s]	type
1	100	60	1
2	100	60	3
3	100	60	1
4	370	120	2
5	500	60	2
6	100	60	3

- **Top gate and bonding pads:**
  - 3-solvent-clean
  - pre-bake at 120 °C for 5 min, let the sample cool to RT
  - spin photoresist *ma-N 415* at 6000 rpm for 40 s, 6 s rise time ($\sim 1.3\,\mu$m)
  - bake at 93 °C for 90 s, let the sample cool to RT
  - align and expose gate pattern for 6 s (*MJB4*, channel II, hard contact 2 s)
  - develop in *ma-D 377XP*[6] for $\sim 3-5$ min, rinse in DI H_2O for 10 s
  - check under microscope for good undercut and add development time if necessary
  - oxygen plasma etch: 16 %, 250 mTorr, 30 W for 40 s
  - evaporate Ti/Au 15 nm/300 nm
  - lift-off in warm (45 °C) remover *mr-Rem 660* or NMP for $30-60$ min, rinse in IPA, blow off

[6] also from microresist technology GmbH, Germany

QPC Sample Fabrication

- **Clean Ga on the back of the wafer:** same procedure as for the Hall bar fabrication
- **Alignment grid:**
  - 3-solvent-clean
  - pre-bake at 120 °C for 1 min, let the sample cool to RT
  - spin 3:1 *ZEP 520A*[7]:anisole, at 4000 rpm for 40 s, 4 s rise time
  - bake at 180 °C for 3 min, let the sample cool to RT, add gold particles for e-beam focusing
  - write alignment grid with 20keV, 10 μm aperture, working distance (WD) 11 mm, 83 μC/cm^2 clearing dose (step size 8 nm, dwell time 1.6 μs)
  - develop in 1:1 MIBK[8]:IPA for 60 s and then in 9:1 MIBK:IPA for 15 s
  - flood expose sample for 15 min on the mask aligner
  - evaporate Ti/Au 5 nm/20 nm
  - lift-off in warm (45 °C) NMP for 10 min, warm acetone for 30 min, rinse in RT acetone and IPA, blow off
- **AFM SAQD mapping:**
  - record $2-3$ images of each grid quadrant 25×25 μm, with a marker cross in every corner
  - in each quadrant, choose one SAQD surface hill and assign coordinates with respect to the grid
- **Mesa etch:** same procedure as for the Hall bar fabrication
- **Ohmic contacts:** same procedure as for the Hall bar fabrication
- **QPC:**
  - 3-solvent-clean
  - pre-bake at 120 °C for 1 min, let the sample cool to RT
  - spin *PMMA*[9] at 4000 rpm for 40 s, 4 s rise time ($\sim$ 120 nm)
  - bake at 180 °C for 7 min, let the sample cool to RT, add gold particles for e-beam focusing
  - write QPC with 20keV, 10 μm aperture, working distance (WD) 11 mm, 100 μC/cm^2 clearing dose (step size 8 nm, dwell time 1.9 μs)
    - dose factor for small (inner) gates: 2.0
    - dose factor for larger (outer) gates: 1.6

[7] Zeon Corporation, Japan
[8] methyl isobutyl ketone
[9] 4% 950K in chlorobenzene

  - develop in 3:1 IPA:MIBK +1.3%MEK[10] for 75 s and then IPA for 15 s
  - evaporate Ti/Au 5 nm/20 nm
  - lift-off in warm (50 °C) acetone for 1 h, rinse in IPA, blow off

- **Top gate and bonding pads:** same procedure as for the Hall bar fabrication, but
  - no ultrasound
  - layer thickness Ti/Au 10 nm/200 nm

[10] methyl ethyl ketone

C.2 Quantum Well Wafers

Hall Bar Fabrication

- **Mesa etch:**
  - 3-solvent-clean
  - pre-bake at 120 °C for 5 min, let the sample cool to RT
  - spin photoresist *ma-N 415* at 6000 rpm for 40 s, 6 s rise time ($\sim 1.3\,\mu$m)
  - bake at 93 °C for 90 s, let the sample cool to RT
  - expose mesa pattern for 4.5 s (*MJB4*, channel II, soft contact)
  - develop in *ma-D 332S* for ~ 100 s, rinse in DI H_2O for 10 s
  - check under microscope and add development time if necessary
  - measure resist height with α-stepper
  - prepare an etch solution with ratio 1:8:240 H_2SO_4:H_2O_2:H_2O
  - measure etch rate by etching a test sample, etch rate $\sim 2-3$ nm/s
  - etch 100 nm, rinse in DI H_2O, check with α-stepper and etch more, if needed
  - wash photoresist with remover *mr-Rem 660* (3 min ultrasound) and rinse in IPA
  - re-check with α-stepper
- **Ohmic contacts:**
  - 3-solvent-clean
  - pre-bake at 120 °C for 5 min, let the sample cool to RT
  - spin photoresist *ma-N 415* at 6000 rpm for 40 s, 6 s rise time ($\sim 1.3\,\mu$m)
  - bake at 93 °C for 90 s, let the sample cool to RT
  - align and expose Ohmic pattern for 4.5 s (*MJB4*, channel II, soft contact)
  - develop in *ma-D 377XP* for $\sim 3-5$ min, rinse in DI H_2O for 10 s
  - check under microscope for good undercut and add development time if necessary
  - oxygen plasma etch: 16 %, 250 mTorr, 30 W for 40 s
  - prepare evaporator
  - dip into HCl for 3 s, rinse in DI H_2O, glue onto evaporation plate with PMMA glue and pump down evaporator, do this within a short period of time (< 5 min)
  - evaporate AuGe/Pt 100 nm/30 nm (thermal/e-beam, AuGe (eutectic): $\sim$ 1.3 g/100 nm)
  - lift-off in warm (45 °C) remover *mr-Rem 660* for $30-60$ min, rinse in IPA, blow off

– thermal annealing (old annealing oven *AZ500*):

step #	T [°C]	time [s]	type
1	100	60	1
2	100	60	3
3	100	60	1
4	370	120	2
5	460	60	2
6	100	60	3

- **Top gate and bonding pads:**
  - 3-solvent-clean
  - pre-bake at 120 °C for 5 min, let the sample cool to RT
  - spin photoresist *ma-N 415* at 6000 rpm for 40 s, 6 s rise time ($\sim 1.3\,\mu$m)
  - bake at 93 °C for 90 s, let the sample cool to RT
  - align and expose gate pattern for 4.5 s (*MJB4*, channel II, soft contact)
  - develop in *ma-D 377XP* for $\sim 3-5$ min, rinse in DI H_2O for 10 s
  - check under microscope for good undercut and add development time if necessary
  - oxygen plasma etch: 16 %, 250 mTorr, 30 W for 40 s
  - evaporate Ti/Au 5 nm/100 nm
  - lift-off in warm (45 °C) remover *mr-Rem 660* for $30-60$ min, rinse in IPA, blow off
  - use silver paint to glue to chip carrier

References

[1] *The Nobel Prize in Physics 1956*. http://www.nobelprize.org/nobel_prizes/physics/laureates/1956/.

[2] R. P. Feynman. *Simulating physics with computers*. International Journal of Theoretical Physics **21**, 467 (1982).

[3] D. Deutsch. *Quantum theory, the Church-Turing principle and the universal quantum computer*. Proceedings of the Royal Society A: Mathematical, Physical and Engineering Sciences **400**, 97 (1985).

[4] M. Nielsen and I. Chuang. *Quantum computation and quantum information*. Cambridge Series on Information and the Natural Sciences (Cambridge University Press, 2000).

[5] T. D. Ladd, F. Jelezko, R. Laflamme, Y. Nakamura, C. Monroe, and J. L. O'Brien. *Quantum computers*. Nature **464**, 45 (2010).

[6] S. Wiesner. *Conjugate coding*. SIGACT News **15**, 78 (1983).

[7] N. Gisin, G. Ribordy, W. Tittel, and H. Zbinden. *Quantum cryptography*. Reviews of Modern Physics **74**, 145 (2002).

[8] B. Schumacher. *Quantum coding*. Physical Review A **51**, 2738 (1995).

[9] P. W. Shor. *Polynomial-time algorithms for prime factorization and discrete logarithms on a quantum computer*. SIAM Review **41**, 303 (1999).

[10] D. P. DiVincenzo. *The physical implementation of quantum computation*. Fortschritte der Physik **48**, 771 (2000).

[11] D. D. Awschalom, L. C. Bassett, A. S. Dzurak, E. L. Hu, and J. R. Petta. *Quantum spintronics: engineering and manipulating atom-like spins in semiconductors*. Science **339**, 1174 (2013).

[12] C. Kloeffel and D. Loss. *Prospects for spin-based quantum computing in quantum dots.* Annual Review of Condensed Matter Physics **4**, 51 (2013).

[13] D. Loss and D. P. DiVincenzo. *Quantum computation with quantum dots.* Physical Review A **57**, 120 (1998).

[14] J. R. Petta, A. C. Johnson, J. M. Taylor, E. A. Laird, A. Yacoby, M. D. Lukin, C. M. Marcus, M. P. Hanson, and A. C. Gossard. *Coherent manipulation of coupled electron spins in semiconductor quantum dots.* Science **309**, 2180 (2005).

[15] R. Hanson, J. R. Petta, S. Tarucha, and L. M. K. Vandersypen. *Spins in few-electron quantum dots.* Reviews of Modern Physics **79**, 1217 (2007).

[16] R. Brunner, Y.-S. Shin, T. Obata, M. Pioro-Ladrière, T. Kubo, K. Yoshida, T. Taniyama, Y. Tokura, and S. Tarucha. *Two-qubit gate of combined single-spin rotation and interdot spin exchange in a double quantum dot.* Physical Review Letters **107**, 146801 (2011).

[17] R. J. Warburton, C. Schäflein, D. Haft, F. Bickel, A. Lorke, A., K. Karrai, J. M. Garcia, W. Schoenfeld, and P. M. Petroff. *Optical emission from a charge-tunable quantum ring.* Nature **405**, 926 (2000).

[18] M. Kroutvar, Y. Ducommun, D. Heiss, M. Bichler, D. Schuh, G. Abstreiter, and J. J. Finley. *Optically programmable electron spin memory using semiconductor quantum dots.* Nature **432**, 81 (2004).

[19] M. Atatüre, J. Dreiser, A. Badolato, A. Högele, K. Karrai, and A. Imamoglu. *Quantum-dot spin-state preparation with near-unity fidelity.* Science **312**, 551 (2006).

[20] P. Michler, A. Kiraz, C. Becher, W. V. Schoenfeld, P. M. Petroff, L. Zhang, E. Hu, and A. Imamoglu. *A quantum dot single-photon turnstile device.* Science **290**, 2282 (2000).

[21] Z. Yuan, B. E. Kardynal, R. M. Stevenson, A. J. Shields, C. J. Lobo, K. Cooper, N. S. Beattie, D. A. Ritchie, and M. Pepper. *Electrically driven single-photon source.* Science **295**, 102 (2001).

[22] S. T. Yilmaz, P. Fallahi, and A. Imamoglu. *Quantum-dot-spin single-photon interface.* Physical Review Letters **105**, 033601 (2010).

[23] W. B. Gao, P. Fallahi, E. Togan, J. Miguel-Sanchez, and A. Imamoglu. *Observation of entanglement between a quantum dot spin and a single photon.* Nature **491**, 426 (2012).

[24] D. Kim, S. G. Carter, A. Greilich, A. S. Bracker, and D. Gammon. *Ultrafast optical control of entanglement between two quantum-dot spins.* Nature Physics **7**, 223 (2010).

[25] H.-A. Engel, J. M. Taylor, M. D. Lukin, and A. Imamoglu. *Quantum optical interface for gate-controlled spintronic devices.* arXiv preprint cond-mat/0612700 (2006).

[26] S. A. Wolf, D. D. Awschalom, R. A. Buhrman, J. M. Daughton, S. von Molnar, M. L. Roukes, A. Y. Chtchelkanova, and D. M. Treger. *Spintronics: A spin-based electronics vision for the future.* Science **294**, 1488 (2001).

[27] I. Zutic, J. Fabian, and S. Sarma. *Spintronics: Fundamentals and applications.* Reviews of Modern Physics **76**, 323 (2004).

[28] S. Datta and B. Das. *Electronic analog of the electro-optic modulator.* Applied Physics Letters **56**, 665 (1990).

[29] H. C. Koo, J. H. Kwon, J. Eom, J. Chang, S. H. Han, and M. Johnson. *Control of spin precession in a spin-injected field effect transistor.* Science **325**, 1515 (2009).

[30] J. Schliemann, J. C. Egues, and D. Loss. *Nonballistic spin-field-effect transistor.* Physical Review Letters **90**, 146801 (2003).

[31] J. D. Koralek, C. P. Weber, J. Orenstein, B. A. Bernevig, S.-C. Zhang, S. Mack, and D. D. Awschalom. *Emergence of the persistent spin helix in semiconductor quantum wells.* Nature **458**, 610 (2009).

[32] M. P. Walser, C. Reichl, W. Wegscheider, and G. Salis. *Direct mapping of the formation of a persistent spin helix.* Nature Physics **8**, 757 (2012).

[33] K. von Klitzing, G. Dorda, and M. Pepper. *New method for high-accuracy determination of the fine-structure constant based on quantized Hall resistance.* Physical Review Letters **45**, 494 (1980).

[34] J. H. Davies. *The Physics of Low-dimensional Semiconductors: An Introduction* (Cambridge University Press, 1998).

[35] D. Leonard, M. Krishnamurthy, C. M. Reaves, S. P. Denbaars, and P. M. Petroff. *Direct formation of quantum-sized dots from uniform coherent islands of InGaAs on GaAs surfaces.* Applied Physics Letters **63**, 3203 (1993).

[36] D. Leonard, K. Pond, and P. M. Petroff. *Critical layer thickness for self-assembled InAs islands on GaAs.* Physical Review B **50**, 11687 (1994).

[37] Y. Tu and J. Tersoff. *Origin of apparent critical thickness for island formation in heteroepitaxy.* Physical Review Letters **93**, 216101 (2004).

[38] Z. M. Wang. *Self-assembled quantum dots* (Springer, New York, 2008).

[39] J. M. Moison, F. Houzay, F. Barthe, L. Leprince, E. André, and O. Vatel. *Self-organized growth of regular nanometer-scale InAs dots on GaAs.* Applied Physics Letters **64**, 196 (1994).

[40] C. Sikorski and U. Merkt. *Spectroscopy of electronic states in InSb quantum dots.* Physical Review Letters **62**, 2164 (1989).

[41] R. J. Warburton, B. T. Miller, C. S. Dürr, C. Bödefeld, K. Karrai, J. P. Kotthaus, G. Medeiros-Ribeiro, P. M. Petroff, and S. Huant. *Coulomb interactions in small charge-tunable quantum dots: A simple model.* Physical Review B **58**, 16 (1998).

[42] J.-Y. Marzin, J.-M. Gérard, A. Izrael, D. Barrier, and G. Bastard. *Photoluminescence of single InAs quantum dots obtained by self-organized growth on GaAs.* Physical Review Letters **73**, 716 (1994).

[43] M. Grundmann, J. Christen, N. N. Ledentsov, J. Böhrer, D. Bimberg, S. S. Ruvimov, P. Werner, U. Richter, U. Gösele, and J. Heydenreich. *Ultranarrow luminescence lines from single quantum dots.* Physical Review Letters **74**, 4043 (1995).

[44] S. Farfad, R. Leon, D. Leonard, J. L. Merz, and P. M. Petroff. *Phonons and radiative recombination in self-assembled quantum dots.* Physical Review B **52**, 5752 (1995).

[45] K. H. Schmidt, G. Medeiros-Ribeiro, M. Oestreich, P. M. Petroff, and G. H. Döhler. *Carrier relaxation and electronic structure in InAs self-assembled quantum dots.* Physical Review B **54**, 11346 (1996).

[46] E. Dekel, D. Gershoni, E. Ehrenfreund, D. Spektor, J. M. Garcia, and P. M. Petroff. *Multiexciton spectroscopy of a single self-assembled quantum dot.* Physical Review Letters **80**, 4991 (1998).

[47] R. C. Ashoori, H. L. Stormer, J. S. Weiner, L. N. Pfeiffer, S. J. Pearton, K. W. Baldwin, and K. W. West. *Single-electron capacitance spectroscopy of discrete quantum levels.* Physical Review Letters **68**, 3088 (1992).

[48] H. Drexler, D. Leonard, W. Hansen, J. P. Kotthaus, and P. M. Petroff. *Spectroscopy of quantum levels in charge-tunable InGaAs quantum dots.* Physical Review Letters **73**, 2252 (1994).

[49] M. Russ, A. Lorke, D. Reuter, and P. Schafmeister. *Self-assembled quantum dots as probes for Landau-level spectroscopy.* Physica E: Low-dimensional Systems and Nanostructures **22**, 506 (2004).

[50] B. J. Van Wees, H. Van Houten, C. W. J. Beenakker, J. G. Williamson, L. P. Kouwenhoven, D. Van der Marel, and C. T. Foxon. *Quantized conductance of point contacts in a two-dimensional electron gas.* Physical Review Letters **60**, 848 (1988).

[51] D. A. Wharam, T. J. Thornton, R. Newbury, M. Pepper, H. Ahmed, J. E. F. Frost, D. G. Hasko, D. C. Peacock, D. A. Ritchie, and G. A. C. Jones. *One-dimensional transport and the quantisation of the ballistic resistance.* Journal of Physics C: Solid State Physics **21**, L209 (1988).

[52] K. J. Thomas, J. T. Nicholls, M. Y. Simmons, M. Pepper, D. R. Mace, and D. A. Ritchie. *Possible spin polarization in a one-dimensional electron gas.* Physical Review Letters **77**, 135 (1996).

[53] S. Cronenwett, H. Lynch, D. Goldhaber-Gordon, L. Kouwenhoven, C. Marcus, K. Hirose, N. Wingreen, and V. Umansky. *Low-temperature fate of the 0.7 structure in a point contact: a Kondo-like correlated state in an open system.* Physical Review Letters **88**, 226805 (2002).

[54] F. Bauer, J. Heyder, E. Schubert, D. Borowsky, D. Taubert, B. Bruognolo, D. Schuh, W. Wegscheider, J. von Delft, and S. Ludwig. *Microscopic origin of the 0.7-anomaly in quantum point contacts.* Nature **501**, 73 (2013).

[55] M. J. Iqbal, R. Levy, E. J. Koop, J. B. Dekker, J. P. de Jong, J. H. M. van der Velde, D. Reuter, A. D. Wieck, R. Aguado, Y. Meir, and C. H. van der Wal. *Odd and even Kondo effects from emergent localization in quantum point contacts.* Nature **501**, 79 (2013).

[56] M. Field, C. G. Smith, M. Pepper, D. A. Ritchie, J. E. F. Frost, G. A. C. Jones, and D. G. Hasko. *Measurements of Coulomb blockade with a noninvasive voltage probe.* Physical Review Letters **70**, 1311 (1993).

[57] M. Poggio, M. P. Jura, C. L. Degen, M. A. Topinka, H. J. Mamin, D. Goldhaber-Gordon, and D. Rugar. *An off-board quantum point contact as a sensitive detector of cantilever motion.* Nature Physics **4**, 635 (2008).

[58] B. J. Van Wees, L. P. Kouwenhoven, H. Van Houten, C. W. J. Beenakker, J. E. Mooij, C. T. Foxon, and J. J. Harris. *Quantized conductance of magnetoelectric subbands in ballistic point contacts.* Physical Review B **38**, 3625 (1988).

[59] P. Debray, S. M. S. Rahman, J. Wan, R. S. Newrock, M. Cahay, A. T. Ngo, S. E. Ulloa, S. T. Herbert, M. Muhammad, and M. Johnson. *All-electric quantum point contact spin-polarizer.* Nature Nanotechnology **4**, 759 (2009).

[60] P. A. M. Dirac. *The quantum theory of the electron.* Proceedings of the Royal Society A: Mathematical, Physical and Engineering Sciences **117**, 610 (1928).

[61] R. Winkler. *Spin-orbit coupling effects in two-dimensional electron and hole systems* (Springer, Berlin; New York, 2003).

[62] V. N. Golovach, M. Borhani, and D. Loss. *Electric-dipole-induced spin resonance in quantum dots.* Physical Review B **74**, 165319 (2006).

[63] K. C. Nowack, F. H. L. Koppens, Y. V. Nazarov, and L. M. K. Vandersypen. *Coherent control of a single electron spin with electric fields.* Science **318**, 1430 (2007).

[64] M. Borhani and X. Hu. *Spin manipulation and relaxation in spin-orbit qubits.* Physical Review B **85**, 125132 (2012).

[65] E. I. Rashba and A. L. Efros. *Efficient electron spin manipulation in a quantum well by an in-plane electric field.* Applied Physics Letters **83**, 5295 (2003).

[66] M. Duckheim and D. Loss. *Electric-dipole-induced spin resonance in disordered semiconductors.* Nature Physics **2**, 195 (2006).

[67] M. Duckheim and D. Loss. *Resonant spin polarization and spin current in a two-dimensional electron gas.* Physical Review B **75**, 201305 R (2007).

[68] J. Schliemann, D. Loss, and R. Westervelt. *Zitterbewegung of electrons and holes in III–V semiconductor quantum wells.* Physical Review B **73**, 085323 (2006).

[69] Y. Oreg, G. Refael, and F. von Oppen. *Helical liquids and Majorana bound states in quantum wires.* Physical Review Letters **105**, 177002 (2010).

[70] R. M. Lutchyn, J. D. Sau, and S. Das Sarma. *Majorana fermions and a topological phase transition in semiconductor-superconductor heterostructures.* Physical Review Letters **105**, 077001 (2010).

[71] Y. A. Bychkov and E. I. Rashba. *Properties of a 2D electron gas with lifted spectral degeneracy.* JETP Letters **39**, 78 (1984). (Pis'ma Zh. Eksp. Teor. Fiz. 39 (1984)).

[72] J. Nitta, T. Akazaki, H. Takayanagi, and T. Enoki. *Gate control of spin-orbit interaction in an inverted $In_{0.53}Ga_{0.47}As/In_{0.52}Al_{0.48}As$ heterostructure.* Physical Review Letters **78**, 1335 (1997).

[73] S. J. Papadakis, E. P. De Poortere, H. C. Manoharan, M. Shayegan, and R. Winkler. *The effect of spin splitting on the metallic behavior of a two-dimensional system.* Science **283**, 2056 (1999).

[74] D. Grundler. *Large Rashba splitting in InAs quantum wells due to electron wave function penetration into the barrier layers.* Physical Review Letters **84**, 6074 (2000).

[75] Y. Kato, R. C. Myers, A. C. Gossard, and D. D. Awschalom. *Coherent spin manipulation without magnetic fields in strained semiconductors.* Nature **427**, 50 (2004).

[76] S. Crooker and D. Smith. *Imaging spin flows in semiconductors subject to electric, magnetic, and strain fields.* Physical Review Letters **94**, 236601 (2005).

[77] G. Dresselhaus. *Spin-orbit coupling effects in zinc blende structures.* Physical Review **100**, 580 (1955).

[78] R. Eppenga and M. F. H. Schuurmanns. *Effect of bulk inversion asymmetry on [001],[110],and [111]GaAs/AlAs quantum wells.* Physical Review B **37**, 10923 (1988).

[79] J. Krich and B. Halperin. *Cubic Dresselhaus spin-orbit coupling in 2D electron quantum dots.* Physical Review Letters **98**, 226802 (2007).

[80] W. Leyland, R. Harley, M. Henini, A. Shields, I. Farrer, and D. Ritchie. *Oscillatory Dyakonov-Perel spin dynamics in two-dimensional electron gases.* Physical Review B **76**, 195305 (2007).

[81] B. Bernevig, J. Orenstein, and S.-C. Zhang. *Exact SU(2) Symmetry and Persistent Spin Helix in a Spin-Orbit Coupled System.* Physical Review Letters **97**, 236601 (2006).

[82] E. A. de Andrada e Silva. *Conduction-subband anisotropic spin splitting in III-V semiconductor heterojunctions.* Physical Review B **46**, 1921 (1992).

[83] U. Rössler and J. Kainz. *Microscopic interface asymmetry and spin-splitting of electron subbands in semiconductor quantum structures.* Solid state communications **121**, 313 (2002).

[84] R. J. Elliott. *Theory of the effect of spin-orbit coupling on magnetic resonance in some semiconductors.* Physical Review **96**, 266 (1954).

[85] G. L. Bir, A. G. Aronov, and G. E. Pikus. *Spin relaxation of electrons due to scattering by holes.* Journal of Experimental and Theoretical Physics **42**, 705 (1976). (Zh. Eksp. Teor. Fiz. 69, 1382 (1975)).

[86] A. W. Overhauser. *Paramagnetic relaxation in metals.* Physical Review **89**, 689 (1953).

[87] J. Jiang and M. Wu. *Electron-spin relaxation in bulk III-V semiconductors from a fully microscopic kinetic spin Bloch equation approach.* Physical Review B **79**, 125206 (2009).

[88] M. Brand, A. Malinowski, O. Karimov, P. Marsden, R. Harley, A. Shields, D. Sanvitto, D. Ritchie, and M. Simmons. *Precession and motional slowing of spin evolution in a high mobility two-dimensional electron gas.* Physical Review Letters **89**, 236601 (2002).

[89] S. D. Ganichev, V. V. Bel'kov, L. E. Golub, E. L. Ivchenko, P. Schneider, S. Giglberger, J. Eroms, J. De Boeck, G. Borghs, and W. Wegscheider. *Experimental separation of Rashba and Dresselhaus spin splittings in semiconductor quantum wells.* Physical Review Letters **92**, 256601 (2004).

[90] B. Das, D. C. Miller, S. Datta, R. Reifenberger, W. P. Hong, P. K. Bhattacharya, J. Singh, and M. Jaffe. *Evidence for spin splitting in* $In_xGa_{1-x}As/In_{0.52}Al_{0.48}As$ *heterostructures as* $B \to 0$. Physical Review B **39**, 1411 (1989).

[91] J. B. Miller, D. M. Zumbühl, C. M. Marcus, Y. B. Lyanda-Geller, D. Goldhaber-Gordon, K. Campman, and A. C. Gossard. *Gate-controlled spin-orbit quantum interference effects in lateral transport.* Physical Review Letters **90**, 076807 (2003).

[92] J. E. Hirsch. *Spin Hall effect.* Physical Review Letters **83**, 1834 (1999).

[93] J. Sinova, D. Culcer, Q. Niu, N. Sinitsyn, T. Jungwirth, and A. MacDonald. *Universal intrinsic spin Hall effect.* Physical Review Letters **92**, 174301 (2004).

[94] T. Ihn. *Electronic quantum transport in mesoscopic semiconductors structures*, volume 192 of *Springer Tracts in Modern Physics* (Springer, 2004).

[95] G. Minkov, O. Rut, A. Germanenko, A. Sherstobitov, V. Shashkin, O. Khrykin, and V. Daniltsev. *Quantum corrections to the conductivity in two-dimensional systems: Agreement between theory and experiment.* Physical Review B **64**, 235327 (2001).

[96] B. L. Al'tshuler, A. G. Aronov, and D. E. Khmelnitsky. *Effects of electron-electron collisions with small energy transfers on quantum localisation.* Journal of Physics C: Solid State Physics **15**, 7367 (1982).

[97] A. M. Finkel'shtein. *Influence of Coulomb interaction on the properties of disordered metals.* Journal of Experimental and Theoretical Physics **81**, 788 (1983). (Zh. Eksp. Teor. Fiz. 84, 168 (1983)).

[98] G. Bergmann. *Weak anti-localization - An experimental proof for the destructive interference of rotated spin 1/2.* Solid State Communications **42**, 815 (1982).

[99] S. Hikami, A. I. Larkin, and Y. Nagaoka. *Spin-orbit interaction and magnetoresistance in the two dimensional random system.* Progress of Theoretical Physics **63**, 707 (1980).

[100] H.-P. Wittmann and A. Schmid. *Anomalous magnetoconductance beyond the diffusion limit.* Journal of Low Temperature Physics **69**, 131 (1987).

[101] F. G. Pikus and G. E. Pikus. *Conduction-band spin splitting and negative magnetoresistance in A_3B_5 heterostructures.* Physical Review B **51**, 16928 (1995).

[102] B. L. Al'tshuler, A. G. Aranov, A. I. Larkin, and D. E. Khmel'nitskil. *Anomalous magnetoresistance in semiconductors.* Journal of Experimental and Theoretical Physics **54**, 411 (1981). (Zh. Eksp. Teor. Fiz. 81, 768 (1981)).

[103] S. V. Iordanskii, Y. B. Lyanda-Geller, and G. E. Pikus. *Weak localization in quantum wells with spin-orbit interaction.* JETP Letters **60**, 206 (1994). (Pis'ma Zh. Eksp. Teor. Fiz. 60, 199 (1994)).

[104] W. Knap, C. Skierbiszewski, A. Zduniak, E. Litwin-Staszewska, D. Bertho, F. Kobbi, J. L. Robert, G. E. Pikus, F. G. Pikus, S. V. Iordanskii, *et al. Weak antilocalization and spin precession in quantum wells.* Physical Review B **53**, 3912 (1996).

[105] M. Kohda, V. Lechner, Y. Kunihashi, T. Dollinger, P. Olbrich, C. Schönhuber, I. Caspers, V. V. Bel'kov, L. E. Golub, and D. Weiss. *Gate-controlled persistent spin helix state in (In,Ga)As quantum wells.* Physical Review B **86**, 081306(R) (2012).

[106] D. Loss and D. P. DiVincenzo. *Quantum computation with quantum dots.* Physical Review A **57**, 120 (1998).

[107] J. Berezovsky, M. H. Mikkelsen, N. G. Stoltz, L. A. Coldren, and D. D. Awschalom. *Picosecond coherent optical manipulation of a single electron spin in a quantum dot.* Science **320**, 349 (2008).

[108] D. Press, T. D. Ladd, B. Zhang, and Y. Yamamoto. *Complete quantum control of a single quantum dot spin using ultrafast optical pulses.* Nature **456**, 218 (2008).

[109] H. Sakaki, G. Yusa, T. Someya, Y. Ohno, T. Noda, H. Akiyama, Y. Kadoya, and H. Noge. *Transport properties of two-dimensional electron gas in AlGaAs/GaAs selectively doped heterojunctions with embedded InAs quantum dots.* Applied Physics Letters **67**, 3444 (1995).

[110] G. H. Kim, D. A. Ritchie, M. Pepper, G. D. Lian, J. Yuan, and L. M. Brown. *Transport properties of two-dimensional electron gases containing InAs self-assembled dots.* Applied Physics Letters **73**, 2468 (1998).

[111] E. Ribeiro, R. Jäggi, T. Heinzel, K. Ensslin, T. G. Medeiros-Ribeiro, and P. M. Petroff. *Transport properties of two-dimensional electron gases in Ga[Al]As heterostructures containing InAs self-assembled quantum dots.* Microelectronic Engineering **47**, 73 (1999).

[112] E. S. Kannan, G.-H. Kim, S. Kumar, I. Farrer, D. A. Ritchie, J. H. Son, J. M. Baik, J.-L. Lee, D. H. Youn, and K.-Y. Kang. *Short range scattering effect of InAs quantum dots in the transport properties of two dimensional electron gas.* Applied Physics Letters **90**, 152110 (2007).

[113] M. Russ, C. Meier, A. Lorke, D. Reuter, and A. Wieck. *Role of quantum capacitance in coupled low-dimensional electron systems.* Physical Review B **73**, 115334 (2006).

[114] W. Lei, M. Offer, A. Lorke, C. Notthoff, C. Meier, O. Wibbelhoff, and A. D. Wieck. *Probing the band structure of InAs/GaAs quantum dots by capacitance-voltage and photoluminescence spectroscopy.* Applied Physics Letters **92**, 193111 (2008).

[115] T. Kawazu, T. Noda, and H. Sakaki. *Inelastic scattering processes in GaAs/n-AlGaAs selectively doped heterojunctions with InGaAs quantum dots.* Physica E: Low-dimensional Systems and Nanostructures **21**, 536 (2004).

[116] J. J. Finley, M. Skalitz, M. Arzberger, A. Zrenner, G. Bohm, and G. Abstreiter. *Electrical detection of optically induced charge storage in self-assembled InAs quantum dots.* Applied Physics Letters **73**, 2618 (1998).

[117] N. Horiguchi, T. Futatsugi, Y. Nakata, and N. Yokoyama. *Electron transport properties through InAs self-assembled quantum dots in modulation doped structures.* Applied Physics Letters **70**, 2294 (1997).

[118] E. E. Vdovin, Y. N. Khanin, P. L. Shabelńikova, A. Levin, L. Eaves, S. V. Dubonos, and M. Henini. *One-electron spin-dependent transport in split-gate structures containing self-organized InAs quantum dots.* Journal of Experimental and Theoretical Physics **105**, 145 (2007). (Zh. Eksp. Teor. Fiz.132, 166 (2007)).

[119] B. Marquardt, M. Russ, A. Lorke, C. Meier, D. Reuter, and A. D. Wieck. *Quan-*

tum dots as tunable scatterers for 2D- and 1D-electron systems. Physica E: Low-dimensional Systems and Nanostructures **40**, 2075 (2008).

[120] M. Jung, T. Machida, K. Hirakawa, S. Komiyama, T. Nakaoka, S. Ishida, and Y. Arakawa. *Shell structures in self-assembled InAs quantum dots probed by lateral electron tunneling structures.* Applied Physics Letters **87**, 203109 (2005).

[121] K. Shibata, C. Buizert, A. Oiwa, K. Hirakawa, and S. Tarucha. *Lateral electron tunneling through single self-assembled InAs quantum dots coupled to superconducting nanogap electrodes.* Applied Physics Letters **91**, 112102 (2007).

[122] C. Buizert, A. Oiwa, K. Shibata, K. Hirakawa, and S. Tarucha. *Kondo universal scaling for a quantum dot coupled to superconducting leads.* Physical Review Letters **99**, 136806 (2007).

[123] Y. Kanai, R. S. Deacon, S. Takahashi, A. Oiwa, K. Yoshida, K. Shibata, K. Hirakawa, Y. Tokura, and S. Tarucha. *Electrically tuned spin-orbit interaction in an InAs self-assembled quantum dot.* Nature Nanotechnology **6**, 511 (2011).

[124] M. Rother. *AQUILA: 2D Schroedinger Poisson solver toolbox for Matlab.* `http://www.mathworks.ch/matlabcentral/fileexchange/3344-2d-schroedinger-poisson-solver-aquila` (1999).

[125] L. Pfeiffer, E. F. Schubert, K. W. West, and C. W. Magee. *Si dopant migration and the AlGaAs/GaAs inverted interface.* Applied Physics Letters **58**, 2258 (1991).

[126] N. N. Ledentsov, M. Grundmann, N. Kirstaedter, O. Schmidt, R. Heitz, J. Böhrer, D. Bimberg, V. M. Ustinov, V. A. Shchukin, and A. Y. Egorov. *Ordered arrays of quantum dots: Formation, electronic spectra, relaxation phenomena, lasing.* Solid-State Electronics **40**, 785 (1996).

[127] H. Saito, K. Nishi, and S. Sugou. *Shape transition of InAs quantum dots by growth at high temperature.* Applied Physics Letters **74**, 1224 (1999).

[128] A. Badolato. Private communication.

[129] D. Scholz. *Wechselwirkung zwischen zweidimensionalen Elektronengasen und selbstorganisierten Quantenpunkten.* Ph.D. thesis, University of Regensburg, Regensburg (2012).

[130] S. J. Papadakis, E. P. De Poortere, H. C. Manoharan, J. Yau, M. Shayegan, and S. Lyon. *Low-field magnetoresistance in GaAs two-dimensional holes.* Physical Review B **65**, 245312 (2002).

[131] D. Weiss, K. V. Klitzing, K. Ploog, and G. Weimann. *Magnetoresistance oscillations in a two-dimensional electron gas induced by a submicrometer periodic potential.* EPL (Europhysics Letters) **8**, 179 (1989).

[132] P. H. Beton, E. S. Alves, P. C. Main, L. Eaves, M. W. Dellow, M. Henini, O. H. Hughes, S. P. Beaumont, and C. D. W. Wilkinson. *Magnetoresistance of a two-dimensional electron gas in a strong periodic potential.* Physical Review B **42**, 9229 (1990).

[133] M. Akabori, J. Motohisa, and T. Fukui. *Large positive magnetoresistance in periodically modulated two-dimensional electron gas formed on self-organized GaAs multiatomic steps.* Physica E: Low-dimensional Systems and Nanostructures **7**, 766 (2000).

[134] F. Takano, S. Kuroda, K. Takita, T. Takamasu, Y. Imanaka, and G. Kido. *Magneto-transport of two-dimensional electron system in magnetic semiconductors heterostructure Cd(Mn)Te/(Cd,Mg)Te.* Physica B: Condensed Matter **298**, 407 (2001).

[135] S. Jeppesen, M. S. Miller, D. Hessman, B. Kowalski, I. Maximov, and L. Samuelson. *Assembling strained InAs islands on patterned GaAs substrates with chemical beam epitaxy.* Applied Physics Letters **68**, 2228 (1996).

[136] M. Helfrich, D. Hu, J. Hendrickson, M. Gehl, D. Rülke, R. Gröger, D. Litvinov, S. Linden, M. Wegener, D. Gerthsen, T. Schimmel, M. Hetterich, H. Kalt, G. Khitrova, H. Gibbs, and D. Schaadt. *Growth and annealing of InAs quantum dots on pre-structured GaAs substrates.* Journal of Crystal Growth **323**, 187 (2011).

[137] E. Steimetz, T. Wehnert, K. Haberland, J.-T. Zettler, and W. Richter. *GaAs cap layer growth and In-segregation effects on self-assembled InAs-quantum dots monitored by optical techniques.* Journal of Crystal Growth **195**, 530 (1998).

[138] J. A. Nixon, J. H. Davies, and H. U. Baranger. *Breakdown of quantized conductance in point contacts calculated using realistic potentials.* Physical Review B **43**, 12638 (1991).

[139] L. I. Glazman and M. Jonson. *Breakdown of conductance quantization and mesoscopic fluctuations in the quasiballistic regime.* Physical Review B **44**, 3810 (1991).

[140] J. G. Williamson, C. E. Timmering, C. Harmans, J. J. Harris, and C. T. Foxon. *Quantum point contact as a local probe of the electrostatic potential contours.* Physical Review B **42**, 7675 (1990).

[141] L. I. Glazman and I. A. Larkin. *Lateral position control of an electron channel in a split-gate device.* Semiconductor Science and Technology **6**, 32 (1991).

[142] B.-Y. Gu, C.-R. Huo, Z.-Z. Gan, G.-Z. Yang, and J.-Q. Wang. *Effects of various obstacles and tunneling disorder on the quantized conductance of an electron waveguide: Model of two coupled chains.* Physical Review B **46**, 13274 (1992).

[143] J. C. Chen, Y. Lin, K. T. Lin, T. Ueda, and S. Komiyama. *Effects of impurity scattering on the quantized conductance of a quasi-one-dimensional quantum wire.* Applied Physics Letters **94**, 012105 (2009).

[144] M. Fricke, A. Lorke, J. P. Kotthaus, G. Medeiros-Ribeiro, and P. M. Petroff. *Shell structure and electron-electron interaction in self-assembled InAs quantum dots.* EPL (Europhysics Letters) **36**, 197 (1996).

[145] V. N. Golovach, A. Khaetskii, and D. Loss. *Phonon-induced decay of the electron spin in quantum dots.* Physical Review Letters **93**, 016601 (2004).

[146] S. Amasha, K. MacLean, I. Radu, D. Zumbühl, M. Kastner, M. Hanson, and A. Gossard. *Electrical control of spin relaxation in a quantum dot.* Physical Review Letters **100**, 046803 (2008).

[147] M. Duckheim, D. L. Maslov, and D. Loss. *Dynamic spin-Hall effect and driven spin helix for linear spin-orbit interactions.* Physical Review B **80**, 235327 (2009).

[148] G. Engels, J. Lange, T. Schäpers, and H. Lüth. *Experimental and theoretical approach to spin splitting in modulation-doped $In_xGa_{(1-x)}As/InP$ quantum wells for $B \to 0$.* Physical Review B **55**, R1958 (1997).

[149] J. Luo, H. Munekata, F. F. Fang, and P. J. Stiles. *Effects of inversion asymmetries on electron energy band structures in GaSb/InAs/GaSb quantum wells.* Physical Review B **41**, 7685 (1990).

[150] G. Bergmann. *Weak localization in thin films: a time-of-flight experiment with conduction electrons.* Physics Reports **107**, 1 (1984).

[151] B. L. Altschuler and A. G. Aronov. *Electron-electron interactions in disordered systems, edited by A. L. Efros and M. Pollak.* Modern Problems in Condensed Matter Sciences (Elsevier, Burlington, MA, 1985).

[152] R. S. Calsaverini, E. Bernardes, J. C. Egues, and D. Loss. *Intersubband-induced spin-orbit interaction in quantum wells.* Physical Review B **78**, 155313 (2008).

[153] M. P. Walser, U. Siegenthaler, V. Lechner, D. Schuh, S. D. Ganichev, W. Wegscheider, and G. Salis. *Dependence of the Dresselhaus spin-orbit interaction on the quantum well width.* Physical Review B **86**, 195309 (2012).

[154] K. D. Maranowski, J. P. Ibbetson, K. L. Campman, and A. C. Gossard. *Interface between low-temperature grown GaAs and undoped GaAs as a conduction barrier for back gates.* Applied Physics Letters **66**, 3459 (1995).

[155] J.-M. Jancu, R. Scholz, E. de Andrada e Silva, and G. La Rocca. *Atomistic spin-orbit coupling and k·p parameters in III-V semiconductors.* Physical Review B **72**, 193201 (2005).

[156] W. Yi, V. Narayanamurti, H. Lu, M. A. Scarpulla, A. C. Gossard, Y. Huang, J. H. Ryou, and R. D. Dupuis. *Bandgap and band offsets determination of semiconductor heterostructures using three-terminal ballistic carrier spectroscopy.* Applied Physics Letters **95**, 112102 (2009).

[157] I. Vurgaftman, J. R. Meyer, and L. R. Ram-Mohan. *Band parameters for III–V compound semiconductors and their alloys.* Journal of Applied Physics **89**, 5815 (2001).

[158] H. Mayer and U. Rössler. *Spin splitting and anisotropy of cyclotron resonance in the conduction band of GaAs.* Physical Review B **44**, 9048 (1991).

[159] The split-off hole offset is written as, $\delta_\Delta = \Delta_b + \delta_v - \Delta_w$. Based on the parameters listed in Table 1, we have, δ_Δ=(0.3287±0.006) eV + (0.171 ± 0.003) eV - (0.341 ± 0.001) eV = (0.1587 ± 0.01) eV.

[160] C. Hermann and C. Weisbuch. *k·p perturbation theory in III-V compounds and alloys: a reexamination.* Physical Review B **15**, 823 (1977).

[161] M. Cardona, N. E. Christensen, and G. Fasol. *Relativistic band structure and spin-orbit splitting of zinc-blende-type semiconductors.* Physical Review B **38**, 1806 (1988).

[162] M. M. Glazov and L. E. Golub. *Spin-orbit interaction and weak localization in heterostructures.* Semiconductor Science and Technology **24**, 064007 (2009).

[163] F. Reif. *Fundamentals of statistical and thermal physics* (McGraw Hill, Tokyo, 1965).

[164] N. S. Averkiev, L. E. Golub, and M. Willander. *Spin relaxation anisotropy in two-dimensional semiconductor systems.* Journal of Physics: Condensed Matter **14**, R271 (2002).

[165] J. J. Lin and J. P. Bird. *Recent experimental studies of electron dephasing in metal and semiconductor mesoscopic structures.* Journal of Physics: Condensed Matter **14**, R501 (2002).

[166] D. Zumbühl, J. Miller, C. Marcus, K. Campman, and A. Gossard. *Spin-orbit coupling, antilocalization, and parallel magnetic fields in quantum dots.* Physical Review Letters **89**, 276803 (2002).

[167] J.-H. Cremers, P. Brouwer, and V. Fal'ko. *Weak localization and conductance fluctuations in a quantum dot with parallel magnetic field and spin-orbit scattering.* Physical Review B **68**, 125329 (2003).

[168] S. Waechter. *Electric transport properties of quantum point contacts in a GaAs quantum well.* Master Thesis (2014).

[169] J. Fu, P. H. Penteado, M. O. Hachiya, D. Loss, and J. C. Egues. *Persistent skyrmion lattice of non-interacting electrons in spin-orbit coupled double wells.* arXiv:1507.00811 (2015).

List of Figures